INTERIM REPORT

Title of the project: Development of Advanced Nano-structured Materials for Electrocatalysis using an Eco-friendly Deep Eutectic Solvents: A Sustainable Approach to Decarbonisation

Short title of the project/Acronym: *DEMADES -09I04-03-V02-00006*

Technology Readiness Level (TRL) of the project activities: TRL 3

Identification of the entities involved in the implementation of the project:

	Official name of the entity	**Abbreviated name of the entity**	**Role in the project**
1	CENTRE FOR ADVANCED MATERIALS APPLICATION SLOVAK ACADEMY OF SCIENCES	CEMEA SAS	Applicant
2	INSTITUTE OF MATERIALS RESEARCH SLOVAK ACADEMY OF SCIENCES	IMR SAS	Partner
3	INSTITUTE OF ELECTRICAL ENGINEERING SLOVAK ACADEMY OF SCIENCES	IEE SAS	Partner

Interim report covers WP1-3:

WP1 – Catalysts preparation

WP2 – Catalysts characterization

WP3 – Electrochemical performance evaluation

Contents

1. General information 3

2. Demonstrating compliance with measurable criteria 5

3. Experimental results 10

3.1 Ni electrodeposition from DES-based electrolyte 10

3.2 SEM, EDX characteristics of Ni deposits obtained in Ethaline-based electrolyte 18

3.3 Preparation of a colloidal Ethaline-based electrolyte for the electrodeposition of MoS_2-containing Ni composites 56

3.3.1 Synthesis of MoS_2 in Ethaline-based electrolytes 57

3.3.2 Synthesis, isolation, and re-dispersion of MoS_2 nanoparticles in Ethaline-based electrolyte for Ni/MoS_2 composite electrodeposition 59

3.3.3 Preparation of Ni–MoS_2 containing electrolyte using commercial MoS_2 powder 61

3.4 Comparison of commercial and synthesized MoS_2 powders 63

3.5 Electrodeposition and characterization of Ni/MoS_2 composite coatings from the Ethaline-based electrolyte 67

3.6 Thermal engineering of MoFeNiP carbon electrocatalysts for efficient hydrogen evolution in acidic and alkaline media 82

3.6.1 Catalyst synthesis 82

3.6.2 Characterization techniques 83

3.6.3 Structural and morphological properties – thermal decomposition 84

3.6.4 XRD analysis and Raman spectroscopy 86

3.6.5. SEM/EDX analysis 87

3.6.6. Electrochemical characterization 88

4. Identification of issues and risks 96

5. Description of planned activities in the next monitoring period (Months 11–20) 97

6. Summary of the interim report (WP1–3) 99

1. General information

The project titled **"Development of Advanced Nano-structured Materials for Electrocatalysis using an Eco-friendly Deep Eutectic Solvents: A Sustainable Approach to Decarbonisation"** ("DEMADES") is underway following the originally planned schedule and objectives.

The project began in Month 1 and is currently in Month 10; all tasks and deliverables scheduled for the first ten months have been implemented in full accordance with the work plan.

Project basics

- Project acronym: DEMADES.
- Duration: months 1-20 (20 months total).
- Participating entities: CEMEA SAS (responsible for WP 1 and WP 3, project coordinator), IMR SAS, and IEE SAS.
- Research theme: Development of nano-structured electrocatalysts for the Hydrogen Evolution Reaction (HER) in alkaline media, using eco-friendly deep eutectic solvents (DESs) as a sustainable route to materials synthesis.
- Five interconnected Work Packages (WP 1 through WP 5) addressing catalyst preparation, characterization, electrochemical evaluation, sustainability assessment and theory/scaling-up.
- Status (at month 10): All tasks scheduled up to month 10 have been completed as planned, including the establishment of laboratories and teams, initiation of synthesis protocols, characterization training, and public outreach events.

It is important to note that the project team and laboratory capabilities will be substantially strengthened over the next few months. Some temporary slowdowns in

the procurement, purchase, and delivery of research equipment were caused by delays in the financial flow of the project, which are now being addressed.

Status highlights (months 1–10):

- WP 1 (Catalysts preparation) started in M1 and is ongoing; foundational tasks (team formation, lab setup, data management plan, theory update, web/social pages) have been executed.
- WP 2 (Catalysts characterization) began in M3; initial training activities and coordination between partners are complete.
- WP 3 (Electrochemical performance evaluation) began in M3; initial electrochemical work/experiments and outreach events have been held.
- WP 4 (Sustainability assessment) began in M8 and the initial work started.
- Beyond strictly research tasks, the consortium has carried out multiple dissemination, outreach and networking activities (e.g., workshops, conferences, public events) which strengthen the project's impact and stakeholder engagement.
- The project website and social media pages have been launched (deliverable D1.1 reached by M4) and are actively updated with news and events (e.g., participation in public workshops, science days, etc.).
- Public engagement and industry networking have progressed, establishing the project's visibility and laying groundwork for future collaboration and industrial translation.

The project is on schedule, the consortium is fully operational, and both research and non-research activities for the first 10 months have been executed in line with the project plan. The next phase will build on this foundation by intensifying catalyst

synthesis, characterization, electrochemical testing and integrating sustainability aspects.

2. Demonstrating compliance with measurable criteria

Below is a table summarizing the planned measurable criteria (deliverables, milestones, activities) for months 1–10 and the status of implementation.

Item	Planned by Month	Description	Status & Comments
M1.1 Fully prepared & staffed labs and teams (WP 1)	Month 2	Establishment of lab facilities, teams, roles/responsibilities	Achieved: lab setup completed for initial work tasks, teams defined, and roles assigned in Month 2
M1.2 Literature review completed (WP 1)	Month 3	Comprehensive review of state-of-the-art for catalyst deposition, DESs, and electrocatalysis	Achieved: literature review completed by the end of Month 3
D1.1 Web page & social networks (WP 1)	Month 4	Project website launched, social media presence established	Achieved: web page live, social page(s) active by Month 4
M2.1 Internal project meeting (WP 2)	Month 5	Consortium internal meeting to discuss early data, collaboration	Achieved: internal meeting held in Month 5 as planned (13 May 2025)
D3.1 Conference paper/research article (WP 3)	Month 6	Submission of the first conference paper and research article	Achieved: conference contribution and research article submitted by Month 6 (see report attachments)
D2.1 Public event(s) for regular public (WP 2)	Month 7	Outreach to the general public via events	Achieved: outreach event(s) conducted by Month 7 (web evidence: public science picnic SCI-CONNECT 2025, June, Summer School of Young Scientists), and other see project web page DEMADES
M3.1 Webinar(s), advanced training course(s) for project team (WP 3)	Month 8	Internal training webinars for the consortium team	Achieved: Advanced Electrochemical Training Course on August 29 (Month 8) DEMADES

D1.2 Conference paper (WP 1)	Month 8	Submission of the second conference paper	Achieved: evidence of conference participation posted online on project web page (additionally see in report attachments)
D3.2 Public event(s) (WP 3)	Month 10	Public event(s) to disseminate project findings	Achieved: Participation in "We Are SAS" event on June 13-14 (Month 6) and other public engagements; thus, target met/exceeded DEMADES

Table illustrating coverage of planned activities during DEMADES project implementation in M1-10.

Publications/activities	**Planned number**	**Published/performed number**
Conference paper	2	4
Articles	1	2
Project meetings	1	1
Advanced training	1	1
Public events/workshops	2	12
Awards	0	2

Detailed information on the mentioned activities is presented below.

Summary of DEMADES Project Activities and Events (Months 1–10)

Date	**Event / Activity**	**Description**
13 May 2025	Strategic Meeting of DEMADES Project Consortium, Bratislava	Hybrid meeting at CEMEA SAS, gathering CEMEA SAS, IEE SAS and IMR SAS to coordinate scientific and organizational activities. (DEMADES)
18-20 June 2025	8th Conference of the Serbian Society for Ceramic Materials (8CSCS-2025), Belgrade	DEMADES team member presented at the international conference on TiO_2 nanotubes and DES methods for catalyst development. (DEMADES)

25 June 2025	SCI-CONNECT 2025: Scientific Picnic by CEMEA SAS and DEMADES project, Bratislava	An outdoor informal scientific event organized by CEMEA SAS and DEMADES team to strengthen collaboration and public engagement. (DEMADES)
14-18 July 2025	Summer School of Young Scientists 2025, Bratislava	Week-long event where DEMADES team participated to engage young students (ages 12-18) in hands-on science. (DEMADES)
29 August 2025	Advanced Electrochemical Training Course for DEMADES Project Team, Bratislava	One-day intensive training at CEMEA SAS laboratory covering electrocatalysis, catalyst synthesis, advanced characterization and durability tests. (DEMADES)
5 September 2025	Challenger Science Award, Bratislava	DEMADES team has been awarded a grant under the Challenger Science program to develop their entrepreneurial potential.
4 September 2025	DEMADES Project at IAM-I Working Groups Meeting, Bratislava	Project represented at the Innovative Advanced Materials Initiative (IAM-I) workshop focusing on advanced materials. (DEMADES)
4-5 September 2025	XVIII International Scientific Conference in Vienna, Austria	DEMADES project team from Bratislava had a presentation devoted to the synthesis of a nanotubular catalyst for photoelectrocatalysis of water-based solutions for efficient hydrogen production.
23 September 2025	Challenger Science Workshop: Exploring Design Thinking, Bratislava	Workshop organised by Civitta & ESET where the DEMADES team participated. (DEMADES)
24 September 2025	3rd Hydrogen Workshop in Bratislava	The workshop on hydrogen strategy (legislative, production, etc.) with the project team's participation. (DEMADES)
26 September 2025	Innovation and Digital Transformation Conference, Bratislava	Participation of DEMADES in a conference on innovation, digital transformation, AI, startups. (DEMADES)
26 September 2025	European Researchers' Night 2025, Bratislava	Interactive presentation of DEMADES team members on the newest material technologies suitable even for the aerospace industry.
30 September 2025	Workshop on Customer Discovery with KU Leuven Technology Transfer Expert, Bratislava	DEMADES team attended a workshop led by business development expert Zuzana Kasanova from KU Leuven. (DEMADES)
6-9 October 2025	8th International Conference "Fracture Mechanics and Fractography of Advanced Ceramics – FAC 2025", Smolenice, Slovakia	DEMADES team from Kosice presented "Degradation mechanisms of the catalyst ceramic layer containing electrospun fibers".

7 October 2025	Challenger Science Workshop: From Research Idea to Business, Bratislava	Participation in ESET & Civitta workshop on 8ommercialization and pitch strategies. (DEMADES)
8 October 2025	IAM-I "Energy" Kick-Off Meeting, (International/web)	Project leader A. Kityk attended the IAM-I "Energy" team kick-off meeting/workshop. (DEMADES)
12-15 October 2025	9th International Conference on Novel Materials, High Tatras, Slovakia	DEMADES team from Kosice presented "Preparation of NiFe LDH catalyst for the oxygen evolution reaction by electrodeposition on nickel foam".
15 October 2025	L'Oréal UNESCO Talent Program Award, Bratislava	DEMADES project leader was awarded first place in the national competition recognizing the most talented women scientists in Slovakia, in the category of Physical and Formal Sciences.
21 October 2025	H2SK Forum, Bratislava	DEMADES team participated in the hydrogen forum focusing on production, legislation, hydrogen economy. (DEMADES)
22 October 2025	Online Event: "Public Research Organisations and Innovation in Europe", (International/web)	Participation in the event by European Patent Office (EPO) Observatory on innovation in public research organisations. (DEMADES)
28 October 2025	Challenger Science Workshop by ESET & Civitta, Bratislava	Another session by the same organisations exploring investment, pitching, startups, where DEMADES team participated. (DEMADES)

Awards

1. DEMADES project leader, Assoc. Prof. Mgr. Anna Kityk, PhD was awarded first place in the national competition recognizing the most talented women scientists in Slovakia, in the category of Physical and Formal Sciences.

2. DEMADES team from Bratislava has been awarded a grant under the Challenger Science program (founded by ESET and Civitta) to develop their entrepreneurial potential.

Published conference papers:

1. A. Kityk, M. Hnatko, V. Pavlik. Electrochemical synthesis of nanotubular TiO_2 on Ti-6Al-4V in deep eutectic solvent: fluoride-free and fluoride-assisted approaches. 8th Conference of the Serbian Society for Ceramic Materials. June 18-20, 2025. Belgrade, Serbia. Book of Abstracts. – pp. 103-104.

2. A. Kityk, J. Soltys, P. Kotrusz, V. Pavlik, M. Hnatko. Enhanced hydrogen evolution via TiO_2 nanotubes on Ti-6Al-4V fabricated by deep eutectic solvent electroprocessing. XVIII International Scientific Conference. September 4-5, 2025. Vienna, Austria. Book of Abstracts. – pp. 18-20.

3. M. Plevová, J. Hnat, M. Bouzek. Preparation of NiFe LDH catalyst for the oxygen evolution reaction by electrodeposition on nickel foam. 9th International Conference on Novel Materials – Fundamentals and Applications. October 12-15, 2025. High Tatras, Slovakia. Book of Abstracts. – p. 83.

4. E. Múdra, I. Shepa, M. Strečková, P. Hviščová. Degradation mechanisms of the catalyst ceramic layer containing electrospun fibers. 8th International Conference "Fracture Mechanics and Fractography of Advanced Ceramics – FAC 2025", October 6-9, 2025. Smolenice, Slovakia. Book of Abstracts. – p. 37.

Published articles:

1. A. Kityk, B. Sadeghi, V. Pavlik, M. Hnatko, M. Balog. Unveiling Structure–Performance Relationships in HER Catalysts for Sustainable and Scalable Hydrogen Production. MATRE-D-25-00080. Materials reports: Energy. In print.

2. T. Mudrinić, A. Guboová, I. Shepa, E. Múdra, O. Milkovic, M. Strečková. Thermal engineering of MoFeNiP carbon electrocatalysts for efficient hydrogen evolution in acidic and alkaline media. Processes (2025) 3954099. In print.

Submitted articles:

1. Kityk, V. Pavlik, M. Hnatko. Integrating Artificial Intelligence with Electrochemical Science for Advanced Energy Conversion and Storage. EST-D-25-10261. Journal of Energy Storage.

Commentary:

- All major deliverables and milestones scheduled for months 1–10 have been successfully completed or are on track.
- Some items (e.g., public outreach) have even exceeded expectations in terms of visibility and engagement.
- No deviations or delays have been identified at this stage; the project remains fully compliant with the measurable criteria for the first 10 months.

3. Experimental results

3.1 Ni electrodeposition from DES-based electrolyte

Nickel (Ni) electrodeposition has gained significant interest due to its wide range of applications in corrosion protection, microelectronics, and catalysis, including hydrogen evolution reaction (HER) catalysis in both alkaline and acidic media. Traditionally, aqueous and organic solvent-based electrolytes have been used for Ni deposition. However, these systems often face challenges like hydrogen evolution, toxicity, and limited environmental sustainability. In recent years, deep eutectic solvents (DESs) have emerged as promising alternatives owing to their low

volatility, biodegradability, and adjustable physicochemical properties. Among various DESs, Ethaline, a mixture of choline chloride and ethylene glycol, has proven particularly effective for metal electrodeposition due to its relatively high ionic conductivity, broad electrochemical stability window, and ability to dissolve metal salts efficiently.

The electrodeposition of nickel from Ethaline-based electrolytes offers an environmentally friendly and adaptable method for producing high-quality Ni coatings with controlled morphology and composition. Understanding the electrochemical behavior, nucleation mechanisms, and impact of deposition parameters in this medium is essential for optimizing film properties for industrial use. This section examines the fundamental aspects of Ni electrodeposition in Ethaline, including electrolyte analysis, deposition kinetics, and the surface morphology of the resulting nickel layers.

The composition of the electrolyte used for Ni electrodeposition in this work is summarized in Table 1. The electrolyte is based on the Ethaline deep eutectic solvent, composed of choline chloride and ethylene glycol in a 1:2 molar ratio. Nickel chloride hexahydrate ($NiCl_2 \cdot 6H_2O$) serves as the source of Ni^{2+} ions, while boric acid is added as a buffering agent to help stabilize the pH during deposition. A controlled amount of water is added to reduce the solution's viscosity and enhance its electrical conductivity.

Table 1. Electrolyte composition utilized for Ni electrodeposition

Component	**Content**
*$NiCl_2$*6H_2O*	1.0 M
Boric Acid	0.13 M
Additional water	30 wt. %
Ethaline	balance

Electrodeposition experiments were performed in a thermostated three-electrode glass cell (Fig. 1). Copper substrates (S=4 cm^2) served as working electrodes in all experiments, while a Ni mesh was used as the counter electrode. The reference electrode was an Ag wire in the DES (Ethaline)-based Ni electrolyte. All reported potentials are referenced accordingly.

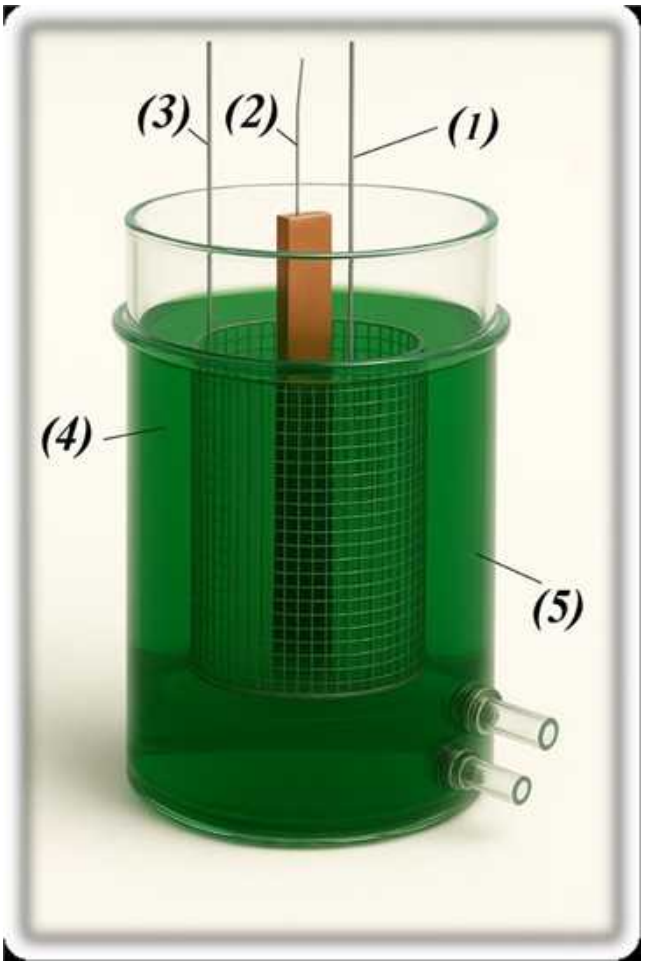


Fig. 1. Schematic illustration of the electrochemical cell used for Ni electrodeposition from Ethaline-based electrolyte: 1 – Ag-wire (pseudo reference electrode); 2 – Cu substrate (working electrode); 3 – Ni-mesh (counter electrode); 4 – electrolyte for Ni electrodeposition; 5 – thermostatically controlled jacketed glass cell.

The experimental conditions used for Ni electrodeposition are summarized in Table 2. As shown, the deposition time was fixed at 20 minutes, while the temperature varied between 30°C and 60°C. Electrodeposition was performed under galvanostatic conditions, with current densities ranging from 2 to 50 mA/cm². To assess the effect of temperature on the Ni electrodeposition process, a narrower current density range of 5–20 mA/cm² was chosen for detailed study. Current densities below 5 mA/cm² produced coatings that were too thin, while those above 20 mA/cm² resulted in cracked deposits.

Table 2. Experimental conditions for Ni electrodeposition from an Ethaline-based electrolyte.

Sample	**i, mA/cm^2**	**t, ºC**	**τ, min**
1	2	40	20
2	5		
3	10		
4	15		
5	20		
6	30		
7	50		
8	5	50	
9	10		
10	15		
11	20		
12	5	60	
13	10		
14	15		

15	20		
16	5	30	
17	10		
18	15		
19	20		

Determining the optimal current density and evaluating the influence of temperature are crucial for achieving high-quality nickel electrodeposits with desirable structural and functional properties. The current density directly affects the nucleation and growth rate of nickel crystals, which in turn governs the morphology, grain size, adhesion, and uniformity of the coating. Excessively low current densities can lead to slow deposition rates and thin, porous layers, while excessively high current densities can result in rough, cracked, or stressed deposits due to rapid metal-ion reduction. Similarly, the temperature of the electrolyte influences ion mobility, viscosity, and diffusion kinetics, thereby affecting the overall deposition rate and coating characteristics. By systematically studying these parameters, it becomes possible to optimize the electrochemical process for producing dense, adherent, and defect-free nickel coatings with controlled microstructure and improved performance for various industrial applications.

The stationary i–E curves of Ni electrodeposition at different temperatures (Fig. 2) were constructed using steady-state potentials derived from chronopotentiometric measurements. These potentials were recorded after approximately 10–15 minutes of deposition, once the potential had stabilized, as a function of the applied current density. The initial transient region corresponds to the nucleation and growth stages of nickel on the substrate, followed by the establishment of a quasi-steady-state deposition regime. The potential values

extracted from the stabilized region (up to 20 minutes) are considered representative of the equilibrium conditions of nickel ion reduction in the Ethaline-based electrolyte.

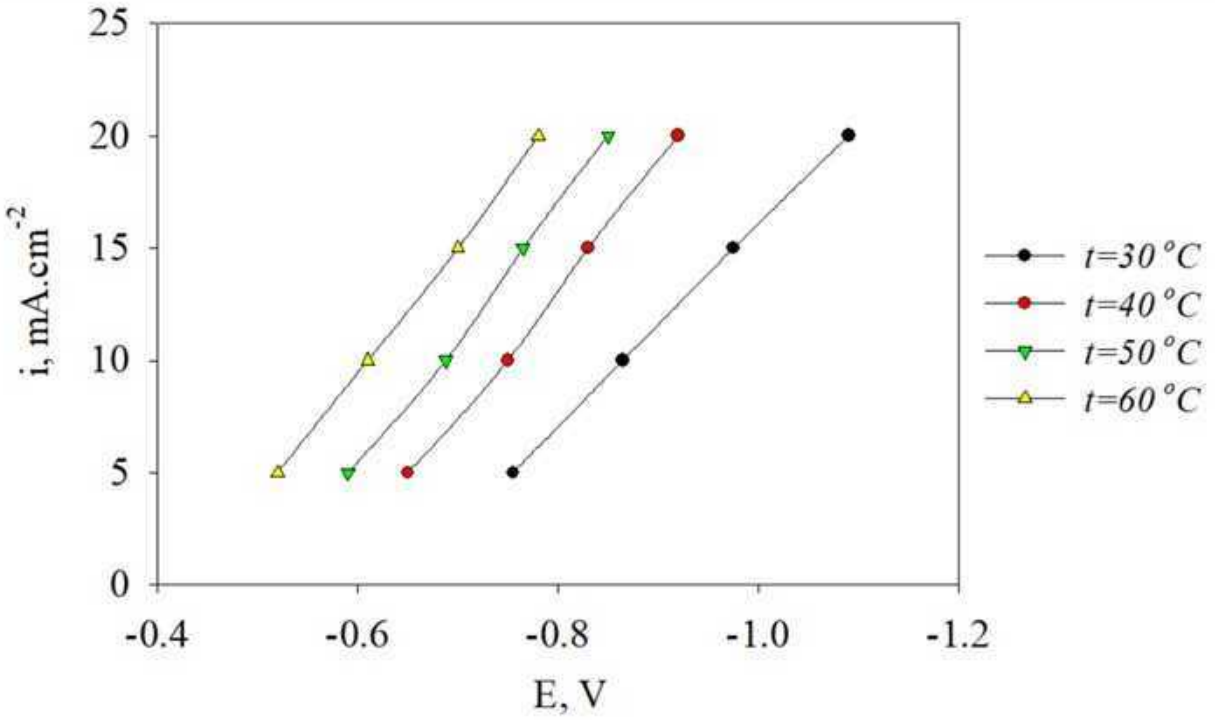


Fig. 2. Stationary i-E curves of Ni electrodeposition from an Ethaline-based electrolyte constructed from steady-state potentials obtained during chronopotentiometric measurements.

The current efficiency (CE) of nickel electrodeposition was evaluated gravimetrically by comparing the measured mass gain of the cathode before and after deposition with the theoretical mass predicted by Faraday's law. The current efficiency was calculated using the following equation:

$$CE=(m_{exp}/m_{theor})\times 100\%, \quad (1)$$

where m_{exp} is the experimentally measured mass increase of the deposit, and $m_{theor}=(M\,I\,\tau)/(n\,F)$, with M being the molar mass of nickel (58.69 $g\cdot mol^{-1}$), I the

applied current, τ the deposition time, n the number of electrons exchanged (2 for $Ni^{2+} \rightarrow Ni$), and F the Faraday constant (96,485 $C \cdot mol^{-1}$). Under all investigated conditions of current density and temperature, the current efficiency values were close to 100%, ranging from 97.6% to 100% (Fig. 3). The lowest efficiency was observed at 30°C, which can be attributed to slower ion transport and/or increased competition from side reactions. The high efficiencies obtained across all conditions confirm the effective utilization of charge for nickel ion reduction in the Ethaline-based electrolyte and indicate that "parasitic" reactions were minimal.

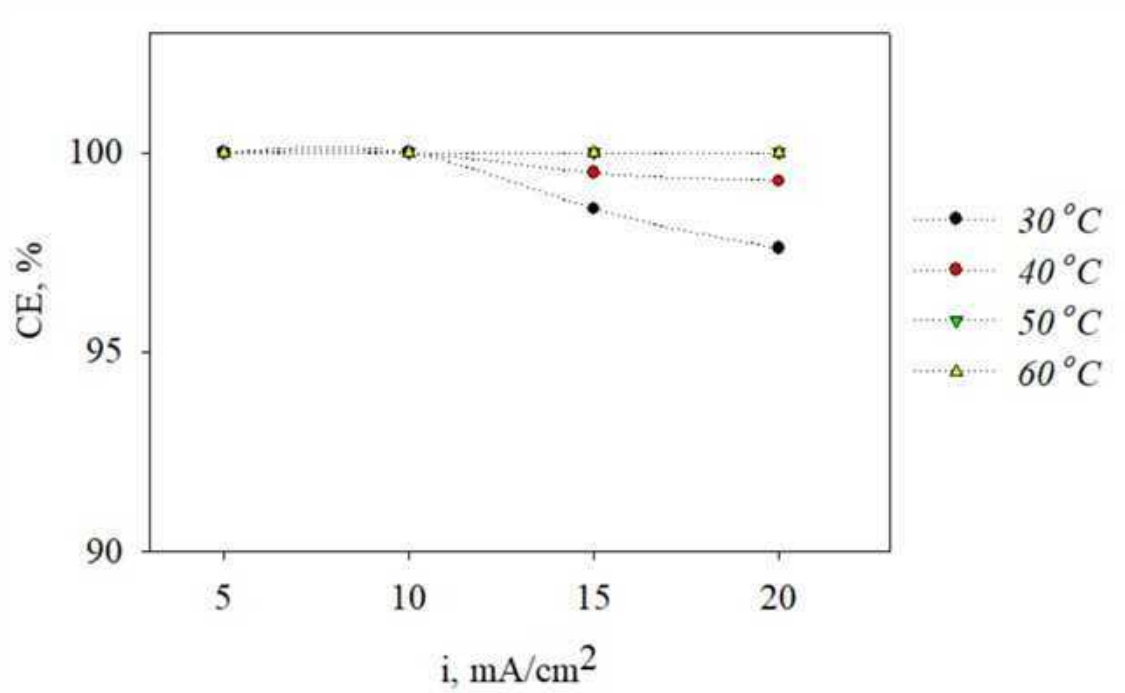


Fig. 3. Effect of temperature and current density on current efficiency of Ni electrodeposition in the Ethaline-based electrolyte.

The deposition rate (DR) of nickel coatings was determined gravimetrically from the mass of the deposits obtained under various electrodeposition conditions. The rate was calculated using the following equation:

$$DR = m_{exp}/(\rho\, A\, \tau) \quad (2)$$

where m_{exp} is the experimentally measured mass of the deposited nickel, ρ is the density of nickel (8.90 $g \cdot cm^{-3}$), A is the surface area of the working electrode, and τ is the deposition time. The resulting deposition rate values ranged from 0.105 $\mu m \cdot min^{-1}$ to 0.42 $\mu m \cdot min^{-1}$, depending on the applied current density and temperature. It should be noted that the estimated DR of Ni from Ethaline-based electrolyte is comparable to that obtained from Watts-type baths (Nickel plating handbook from Nickel institute reports DR from Watts electroplating solution equal to 25 $\mu m \cdot h^{-1}$, which is the same as 0.42 $\mu m \cdot min^{-1}$).

As shown in Fig. 4, the 3D plot clearly shows an increase in deposition rate as current density and temperature rise. This pattern corresponds with faster charge transfer and improved ionic mobility in the electrolyte at higher temperatures, along with the increased nickel ion reduction rate associated with higher current density.

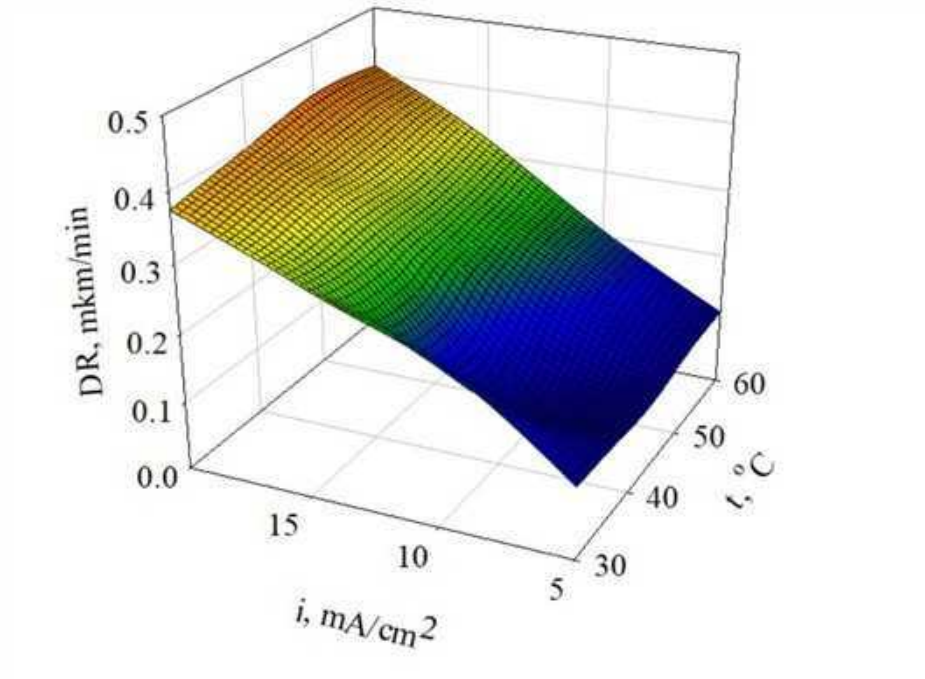


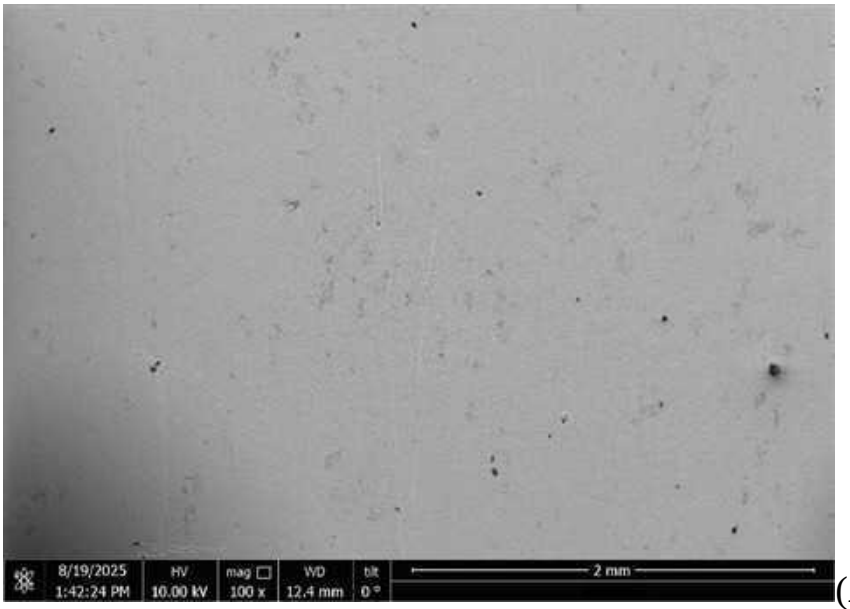
Fig. 4. 3D plot illustrating the influence of deposition current density and electrolyte temperature on deposition rate of Ni in Ethaline-based electrolyte.

To determine the optimal conditions for high-quality Ni electrodeposition from the Ethaline-based electrolyte, detailed SEM and EDX analyses were performed.

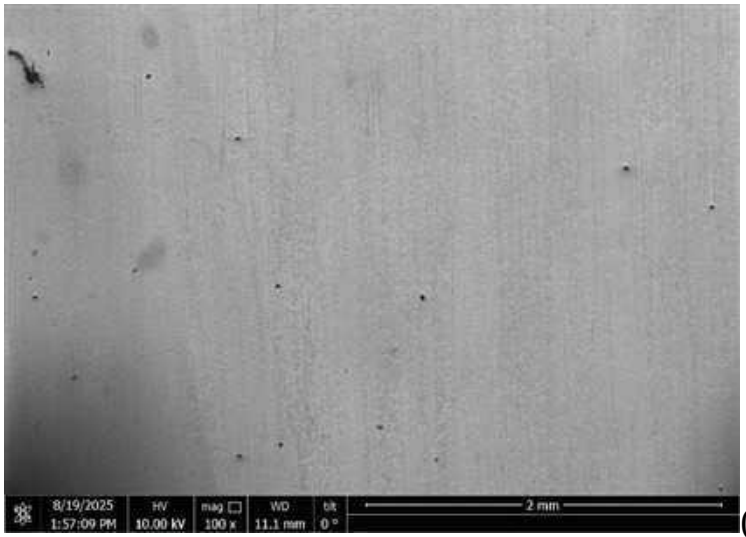
3.2 SEM, EDX characteristics of Ni deposits obtained in Ethaline-based electrolyte

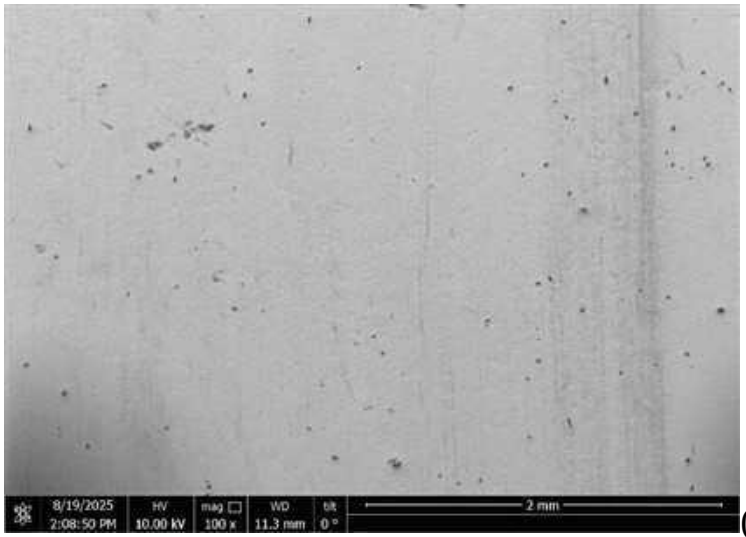
In the development of catalysts for efficient green hydrogen production, it is essential to create catalytically active surfaces with high surface area that remain stable over prolonged operation. Therefore, surface morphology, topography, and chemical composition are key factors for evaluation.

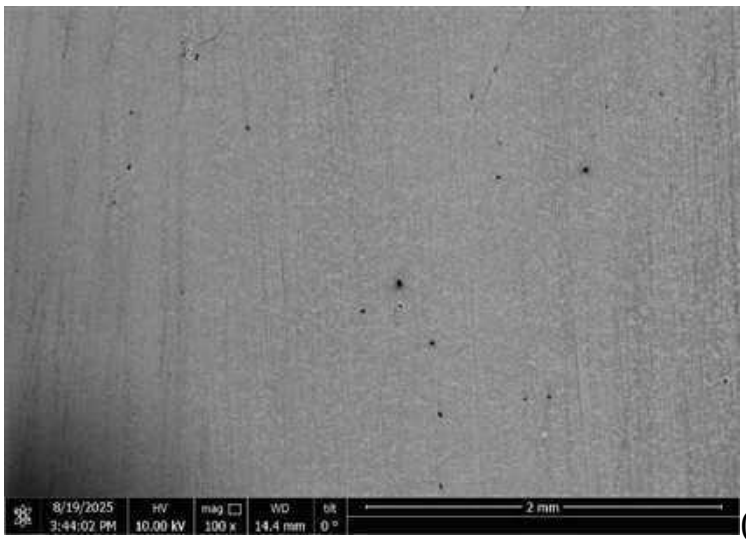
The surfaces of Ni deposits obtained from the Ethaline-based electrolyte were characterized using SEM and EDX techniques. For general observations of Ni coatings, a low magnification (100×, Fig. 5) was used, while higher magnifications were utilized to examine micro- and nano-scale surface textures in more detail (Fig. 6, 7).

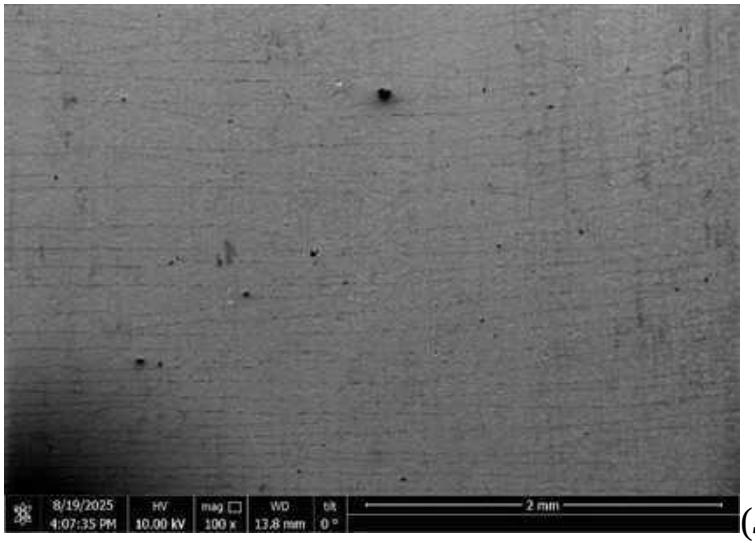


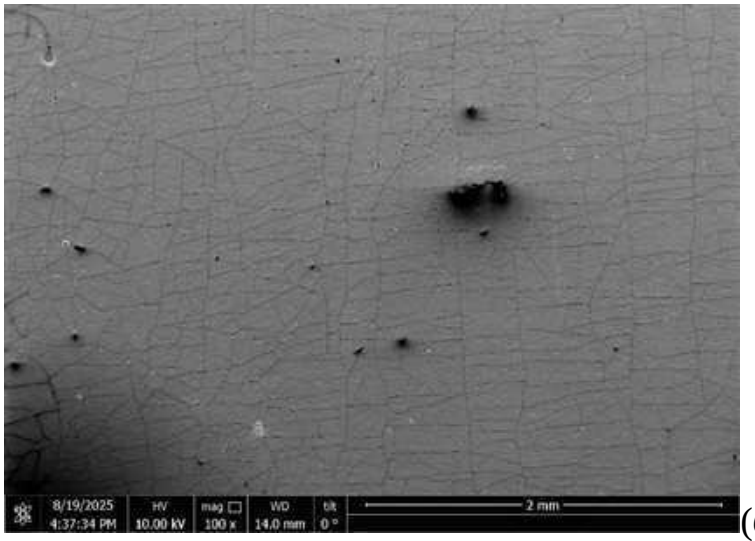
(***1***)

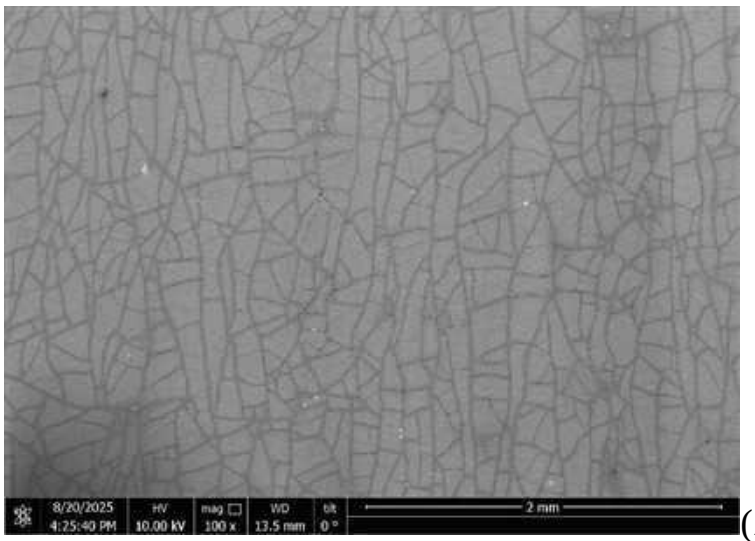

8/19/2025
1:57:09 PM
HV
10.00 kV
mag
100 x
WD
11.1 mm
tilt
0 °
2 mm
(***2***)

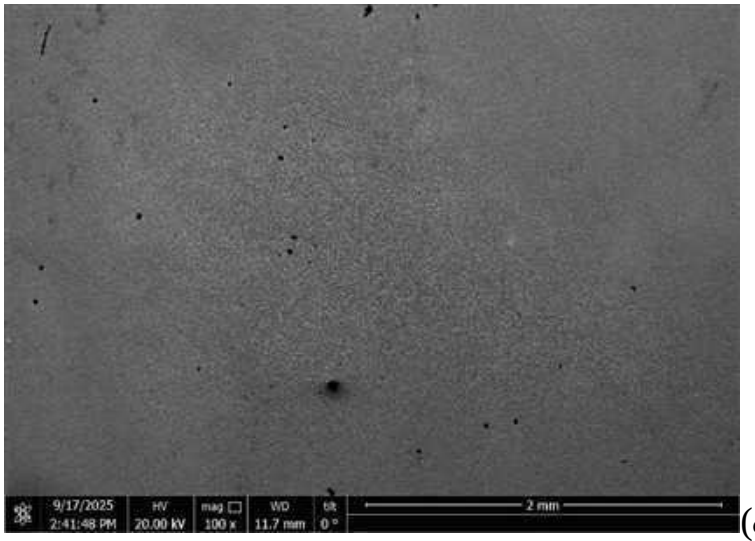

8/19/2025
2:08:50 PM
HV
10.00 kV
mag
100 x
WD
11.3 mm
tilt
0 °
2 mm
(***3***)

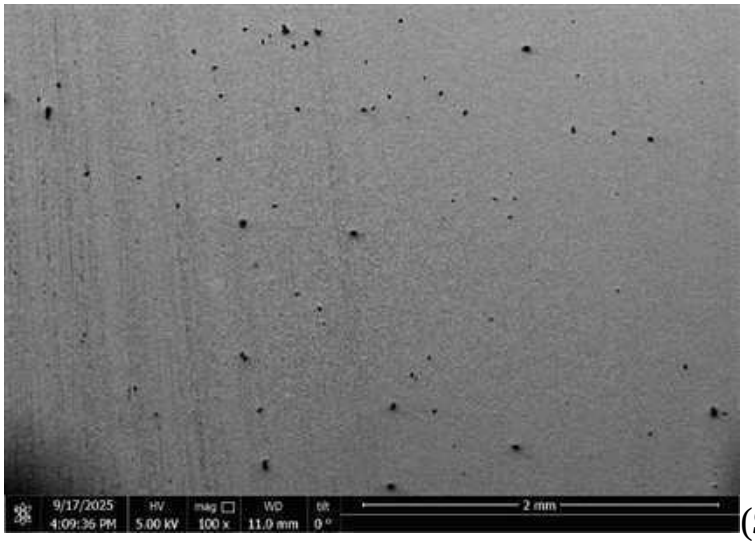

8/19/2025
3:44:02 PM
HV
10.00 kV
mag
100 x
WD
14.4 mm
tilt
0 °
2 mm
(***4***)

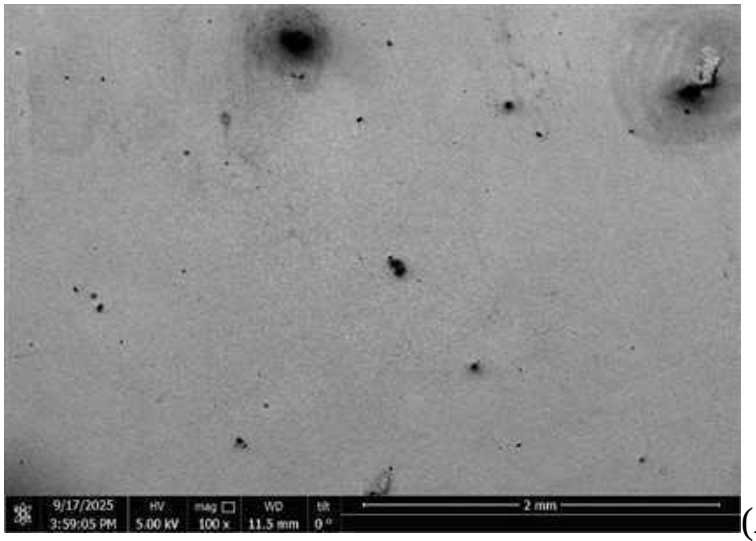

8/19/2025
4:07:35 PM
HV
10.00 kV
mag
100 x
WD
13.8 mm
tilt
0 °
2 mm
(*5*)

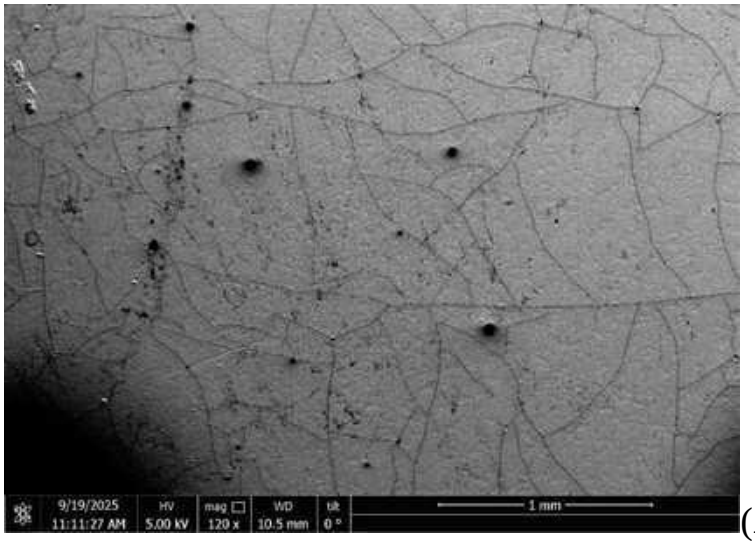

8/19/2025
4:37:34 PM
HV
10.00 kV
mag
100 x
WD
14.0 mm
tilt
0 °
2 mm
(*6*)


8/20/2025
4:25:40 PM
HV
10.00 kV
mag
100 x
WD
13.5 mm
tilt
0 °
2 mm
(*7*)

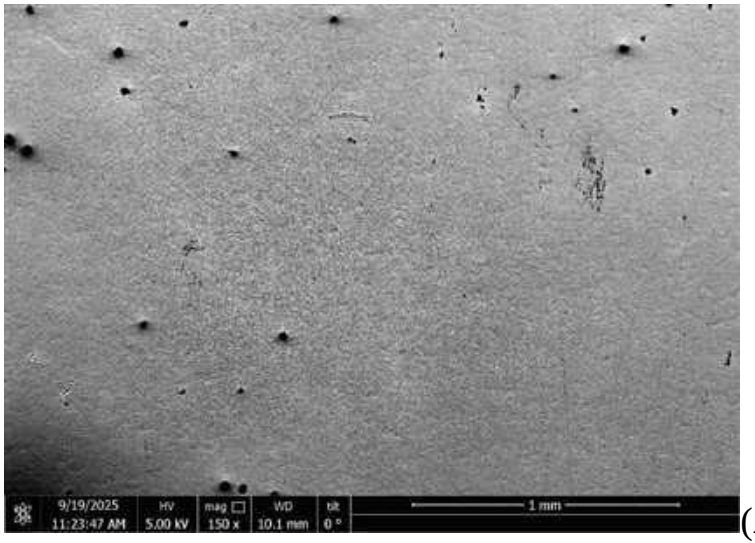

9/17/2025
2:41:48 PM
HV
20.00 kV
mag
100 x
WD
11.7 mm
tilt
0 °
2 mm
(***8***)


9/17/2025
4:09:36 PM
HV
5.00 kV
mag
100 x
WD
11.0 mm
tilt
0 °
2 mm
(***9***)

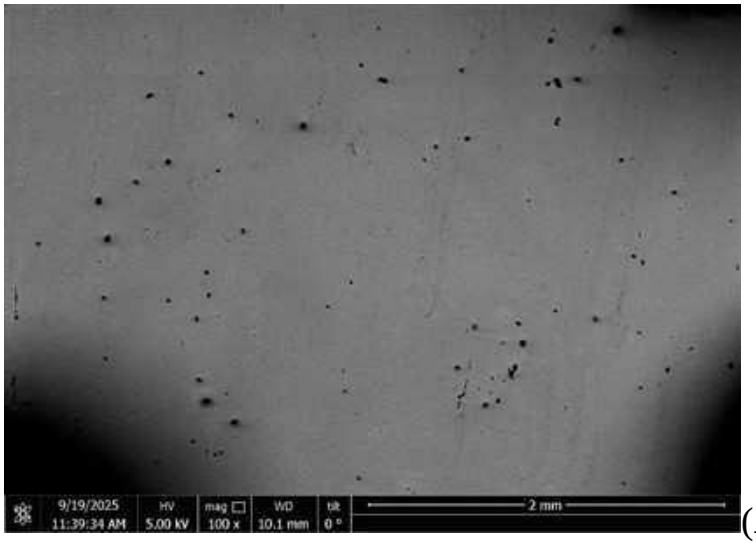

9/17/2025
3:59:05 PM
HV
5.00 kV
mag
100 x
WD
11.5 mm
tilt
0 °
2 mm
(***10***)


9/19/2025
11:11:27 AM
HV
5.00 kV
mag
120 x
WD
10.5 mm
tilt
0 °
1 mm

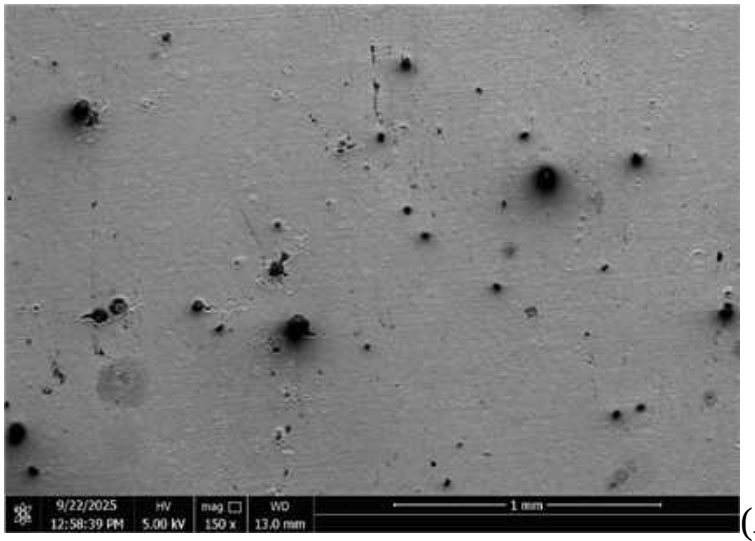
(***11***)*

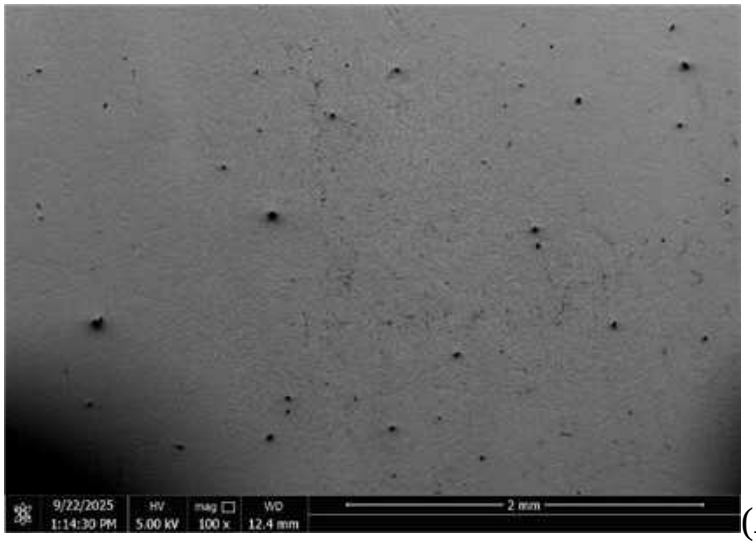

9/19/2025
11:23:47 AM
HV
5.00 kV
mag
150 x
WD
10.1 mm
tilt
0 °
1 mm

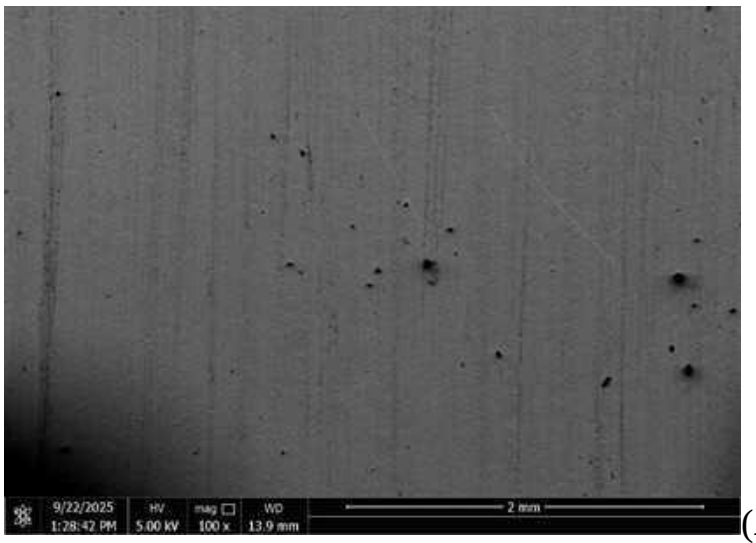
(***12***)**

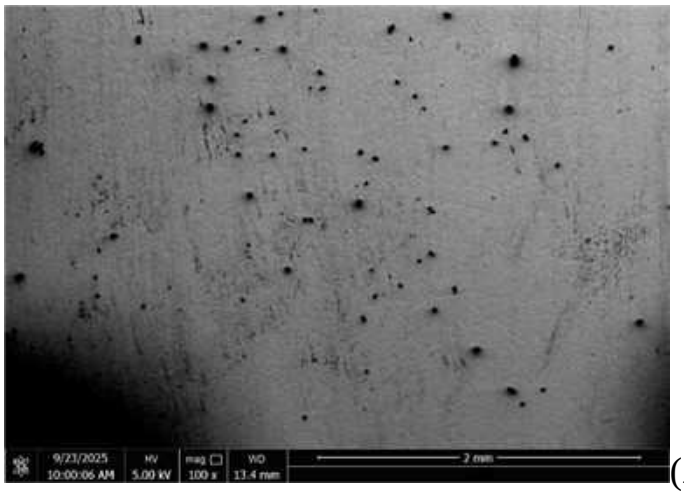

9/19/2025
11:39:34 AM
HV
5.00 kV
mag
100 x
WD
10.1 mm
tilt
0 °
2 mm

(***13***)

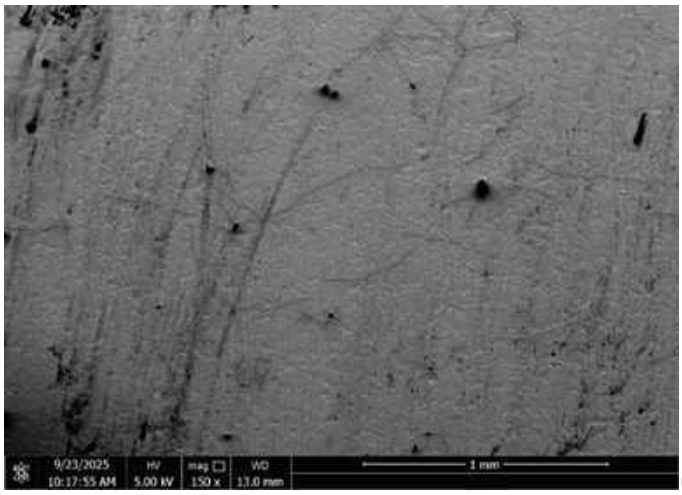

9/22/2025
12:58:39 PM
HV
5.00 kV
mag
150 x
WD
13.0 mm
1 mm
(***14***)**


9/22/2025
1:14:30 PM
HV
5.00 kV
mag
100 x
WD
12.4 mm
2 mm
(***15***)

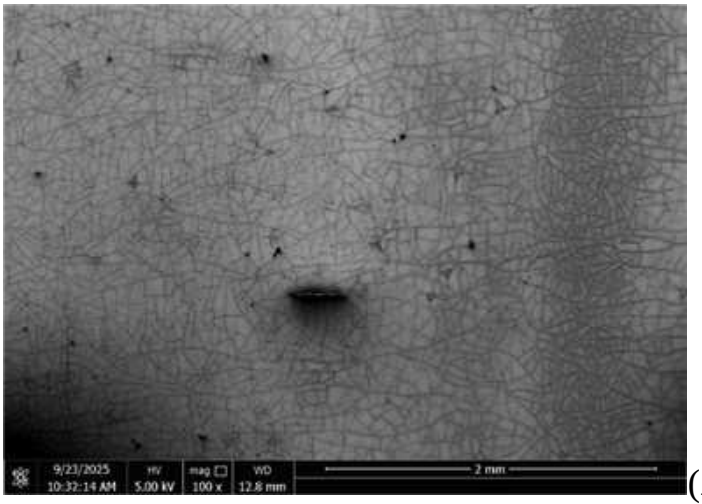

9/22/2025
1:28:42 PM
HV
5.00 kV
mag
100 x
WD
13.9 mm
2 mm
(***16***)



(***17***)



(***18***)**



(***19***)

Fig. 5. SEM images of Ni coatings electrodeposited from the Ethaline-based electrolyte under various conditions. Magnification: 100×; scale bar: 2 mm.

*Magnification: 120×; scale bar: 1 mm. **Magnification: 150×; scale bar: 1 mm. Sample numbers correspond to the electrodeposition parameters listed in Table 2.

The obtained results revealed that increasing the deposition current density and coating thickness led to the formation of surface cracks, which can be attributed to the well-known internal stresses that develop in electrodeposited Ni layers. These stresses arise from factors such as hydrogen incorporation, lattice mismatch, and rapid grain growth during deposition.

It is noteworthy that at the lowest investigated temperature (30 °C), cracks appeared at relatively low current densities, i.e., at or above 15 mA cm^{-2}. As the temperature increased, the onset of cracking shifted to higher current densities. For example, at 40 °C and 50 °C, surface cracking was first observed at 20 mA cm^{-2}. Interestingly, at 60 °C, no cracks were detected across the entire range of applied current densities, indicating that elevated temperature reduces internal stress formation and improves coating ductility.

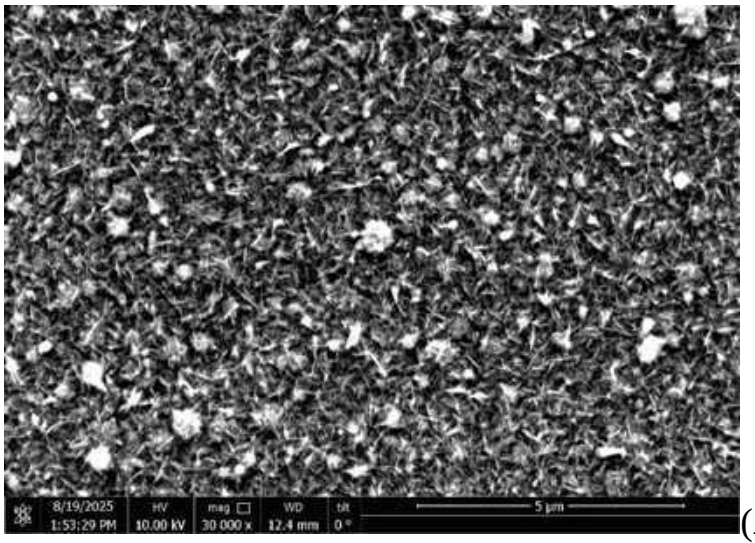
Admit that the most homogeneous and compact Ni surfaces were obtained under moderate deposition conditions, specifically, at temperatures of 40–50 °C and current densities of 10–15 mA cm^{-2}, where the balance between nucleation rate, grain growth, and stress relaxation appears optimal.

Figs. 6 and 7 clearly reveal the presence of micro- and nano-scale structures on the surfaces of Ni coatings deposited from Ethaline-based electrolytes. It is evident that both the electrolyte temperature and deposition current density significantly influence surface morphology and topography.

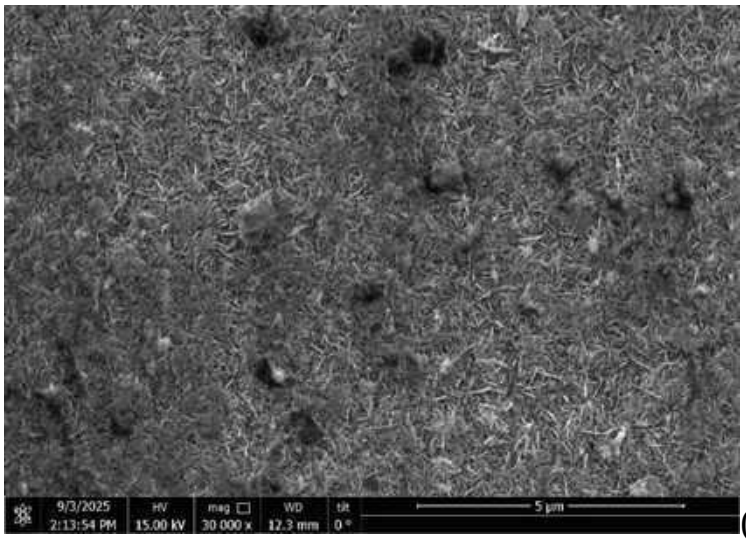
At low to moderate temperatures (30 and 40 °C), the coating surfaces exhibit a homogeneous lamellar texture composed of nano-sized lamellae. As the temperature increases (50 and 60 °C), the surface morphology changes to feature micro-sized hemispherical hills. These effects are particularly pronounced at low current

densities (5–10 mA cm^{-2}), suggesting that lower nucleation rates combined with higher atomic mobility at elevated temperatures favor the growth of larger microstructures.

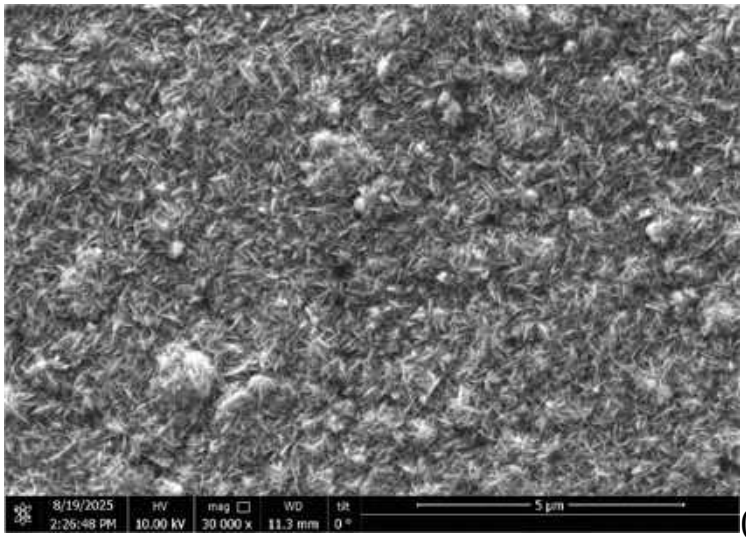
By varying the deposition current density and electrolyte temperature, it is possible to tailor the surface structure, producing either purely nano-textured coatings or combined micro–nano-textured surfaces. Such controlled texturing is of great interest for catalytic applications, as both surface area and hierarchical structures can significantly enhance catalytic activity and mass transport during reactions.

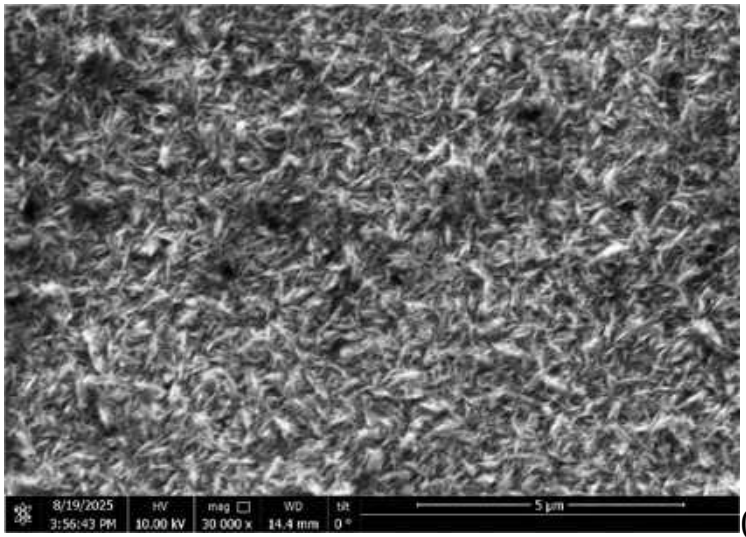


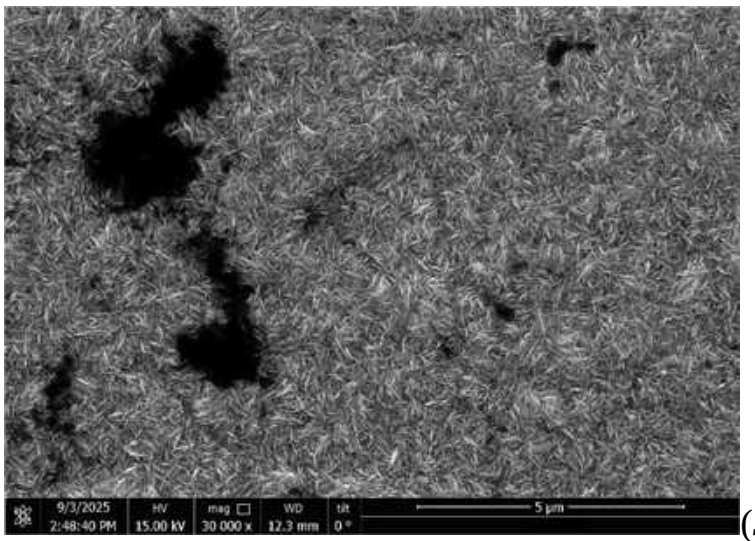
(***1***)

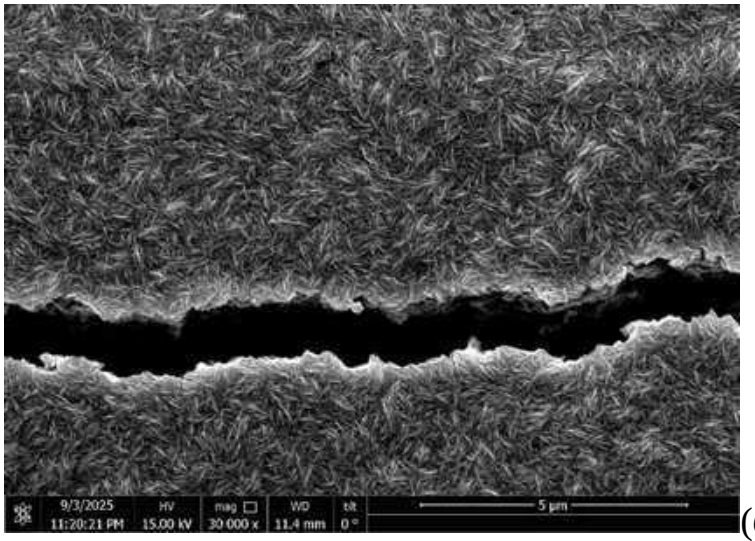


(***2***)

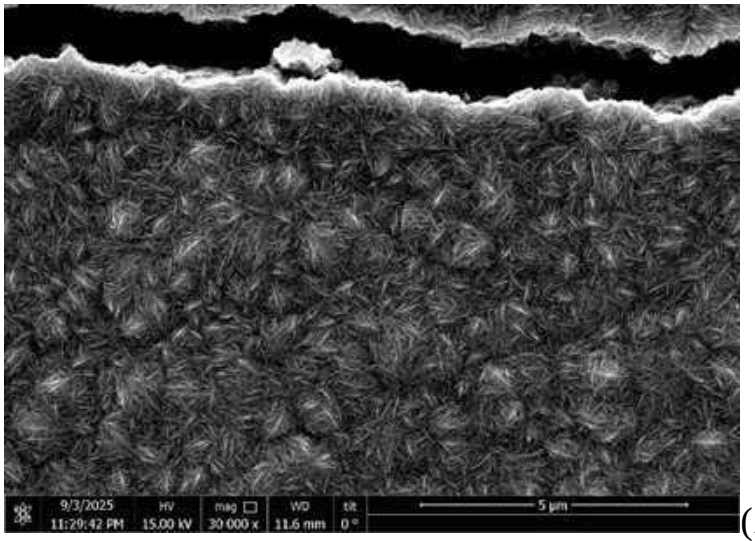

8/19/2025
2:26:48 PM
HV
10.00 kV
mag
30 000 x
WD
11.3 mm
tilt
0 °
5 µm
(***3***)


8/19/2025
3:56:43 PM
HV
10.00 kV
mag
30 000 x
WD
14.4 mm
tilt
0 °
5 µm
(***4***)

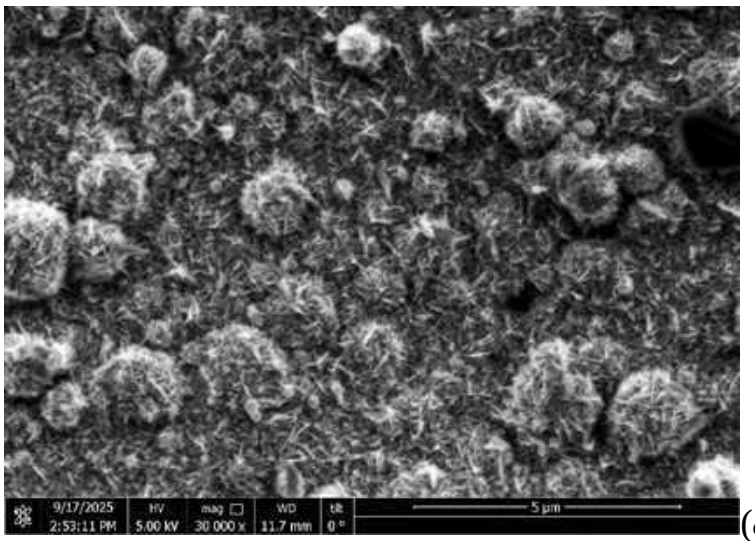

9/3/2025
2:48:40 PM
HV
15.00 kV
mag
30 000 x
WD
12.3 mm
tilt
0 °
5 µm
(***5***)


9/3/2025
11:20:21 PM
HV
15.00 kV
mag
30 000 x
WD
11.4 mm
tilt
0 °
5 µm

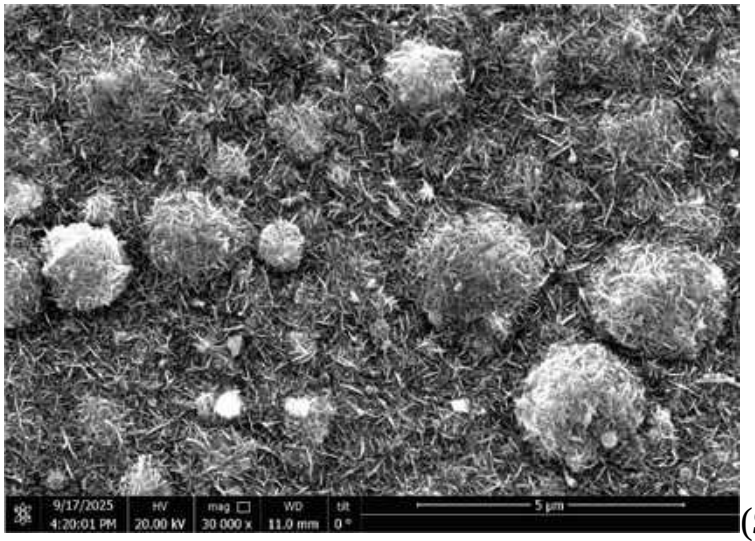
(***6***)

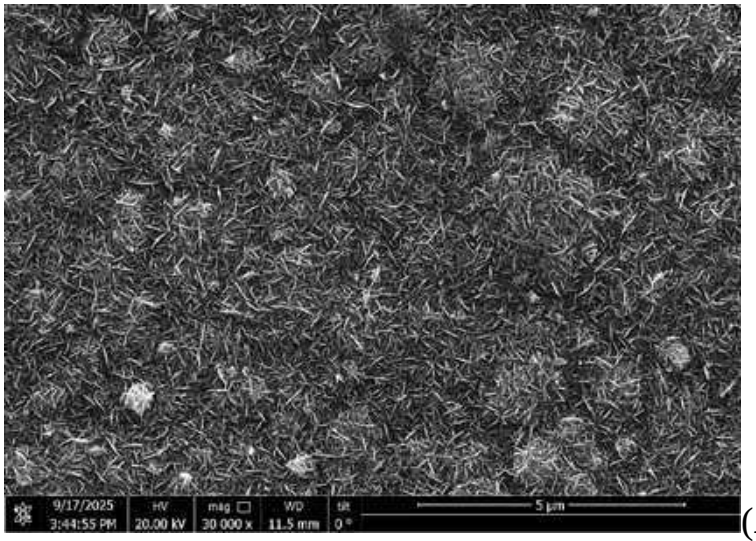

9/3/2025
11:29:42 PM
HV
15.00 kV
mag
30 000 x
WD
11.6 mm
tilt
0 °
5 µm

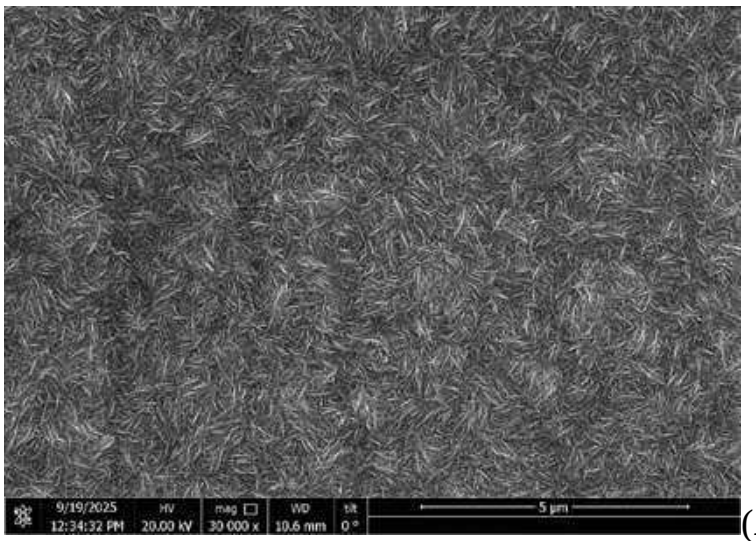
(***7***)

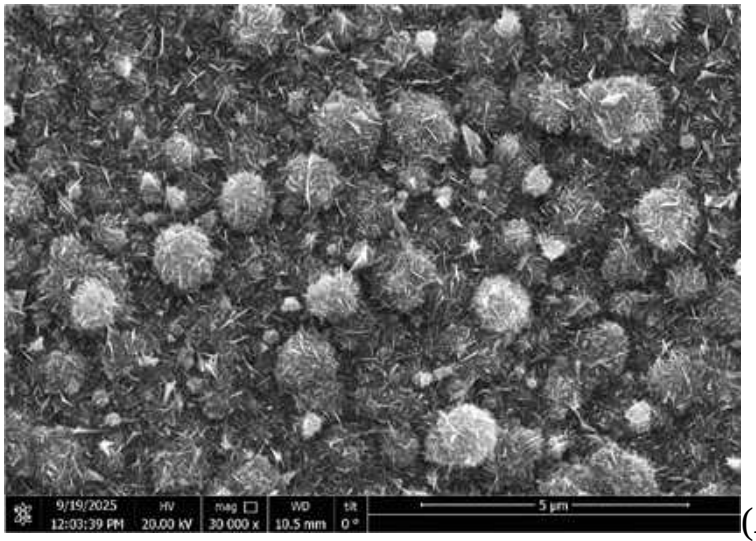

9/17/2025
2:53:11 PM
HV
5.00 kV
mag
30 000 x
WD
11.7 mm
tilt
0 °
5 µm

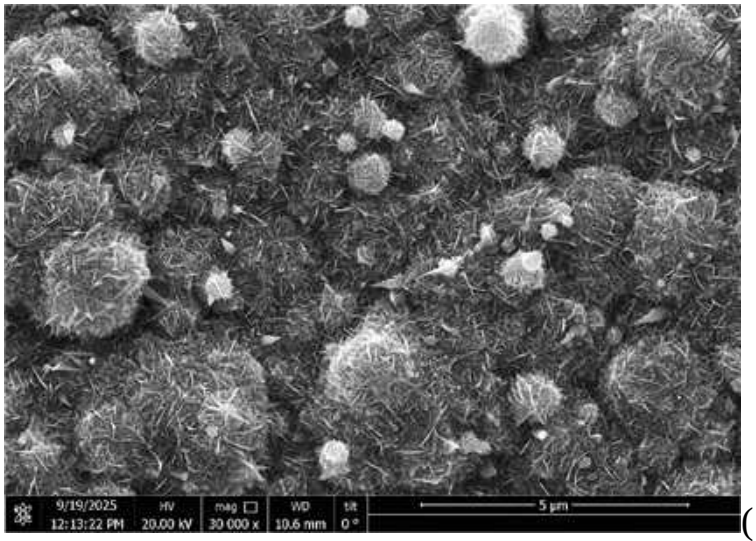
(***8***)

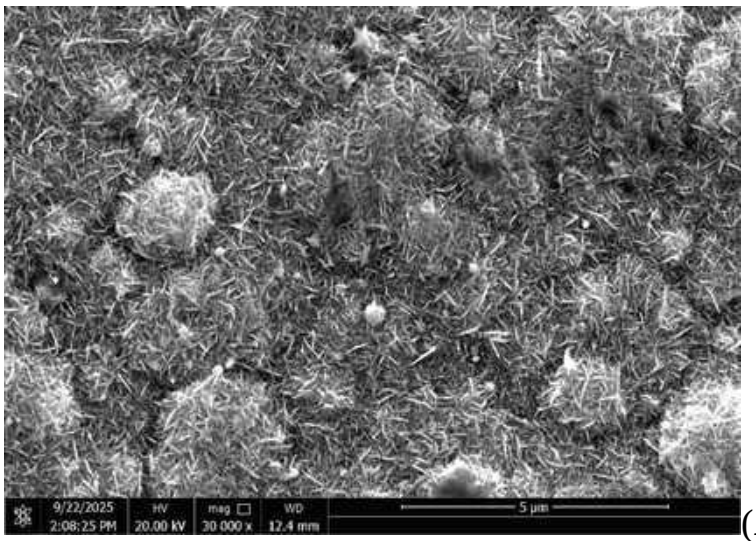

9/17/2025
4:20:01 PM
HV
20.00 kV
mag
30 000 x
WD
11.0 mm
tilt
0 °
5 µm
(***9***)

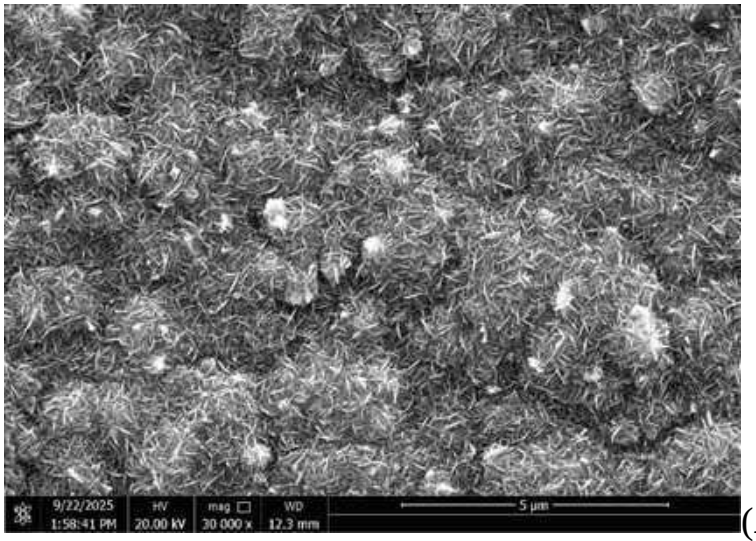

9/17/2025
3:44:55 PM
HV
20.00 kV
mag
30 000 x
WD
11.5 mm
tilt
0 °
5 µm
(***10***)


9/19/2025
12:34:32 PM
HV
20.00 kV
mag
30 000 x
WD
10.6 mm
tilt
0 °
5 µm
(***11***)

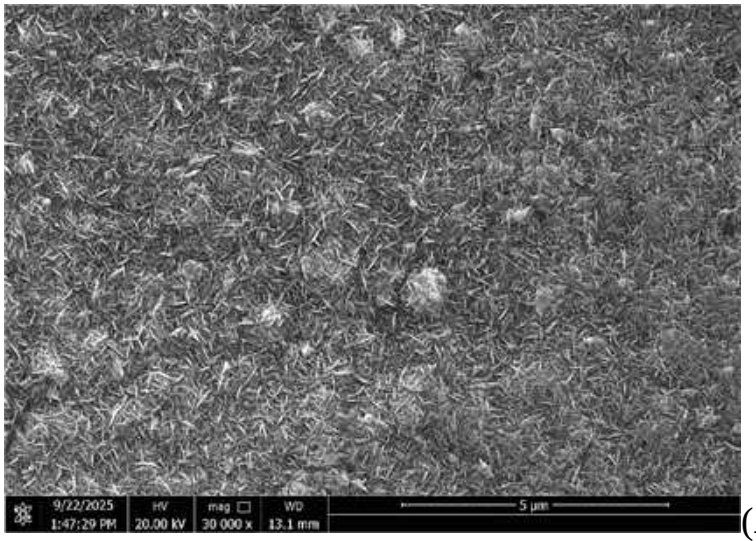

9/19/2025
12:03:39 PM
HV
20.00 kV
mag
30 000 x
WD
10.5 mm
tilt
0 °
5 µm
(***12***)


9/19/2025
12:13:22 PM
HV
20.00 kV
mag
30 000 x
WD
10.6 mm
tilt
0 °
5 µm
(13)

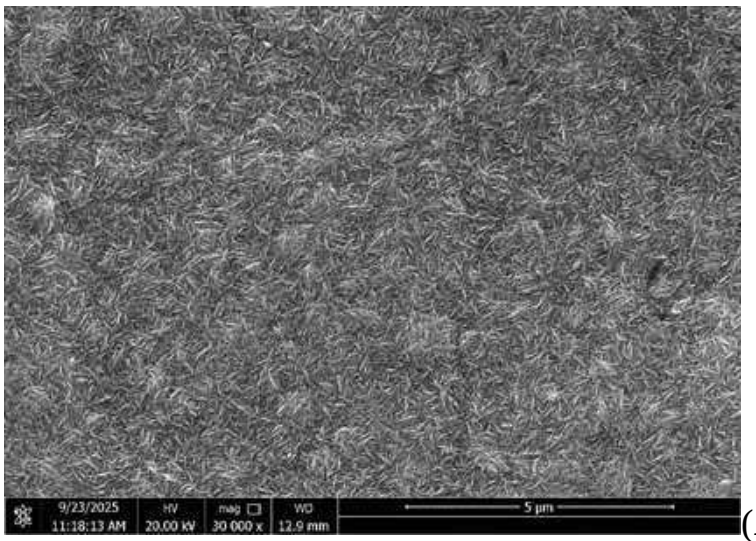

9/22/2025
2:08:25 PM
HV
20.00 kV
mag
30 000 x
WD
12.4 mm
5 µm
(***14***)


9/22/2025
1:58:41 PM
HV
20.00 kV
mag
30 000 x
WD
12.3 mm
5 µm

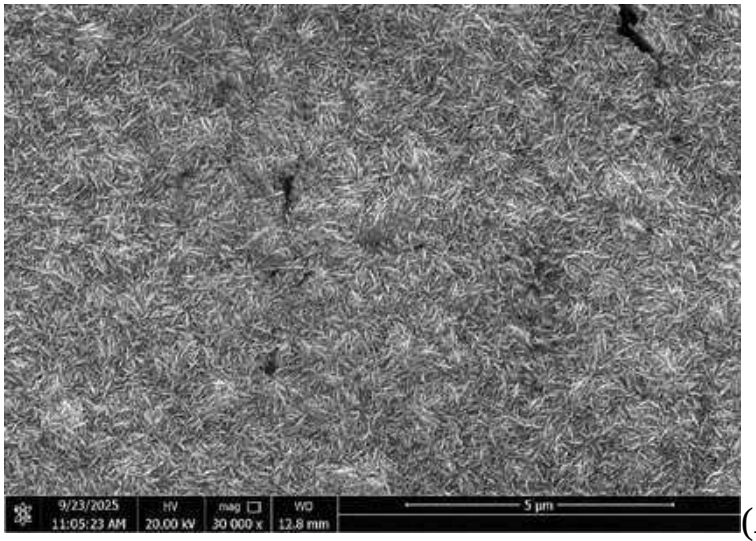
(***15***)


9/22/2025
1:47:29 PM
HV
20.00 kV
mag
30 000 x
WD
13.1 mm
5 µm

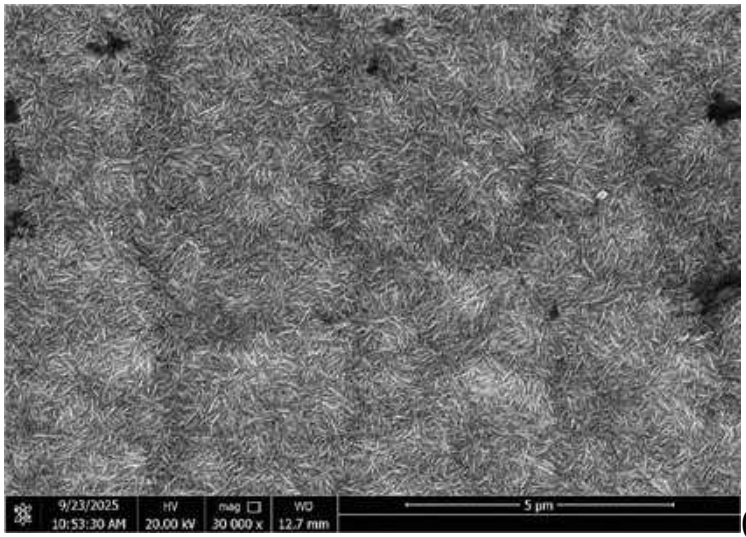
(***16***)


9/23/2025
11:18:13 AM
HV
20.00 kV
mag
30 000 x
WD
12.9 mm
5 µm

(***17***)

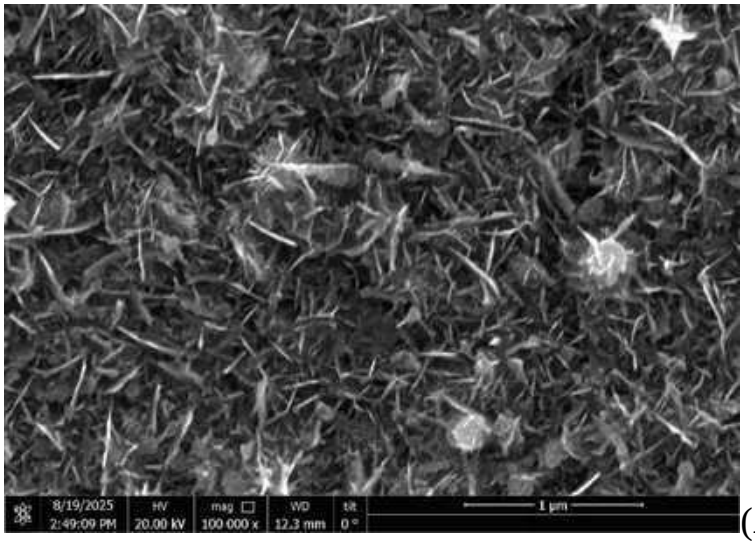


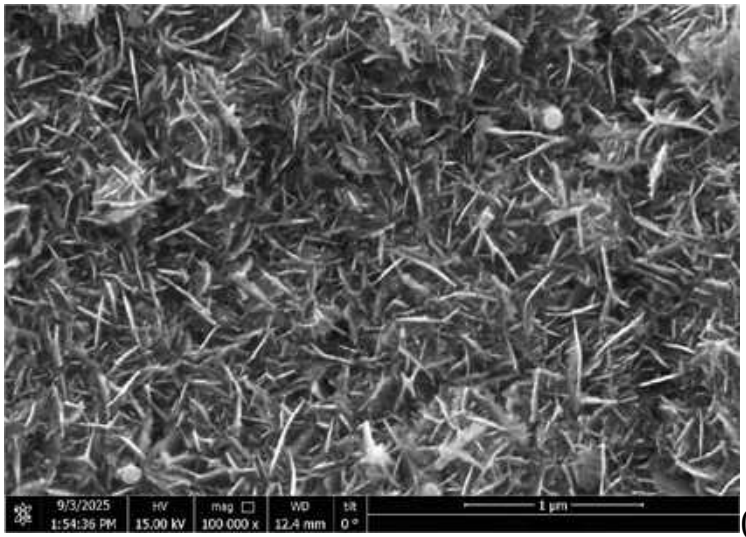
(***18***)

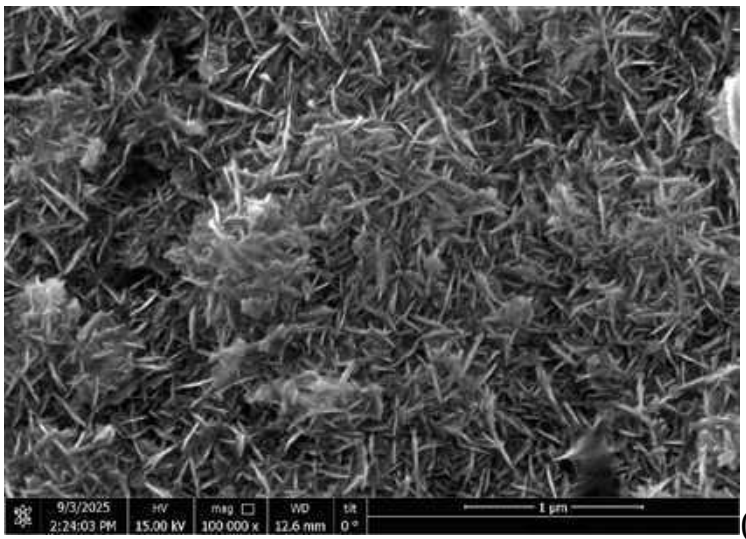


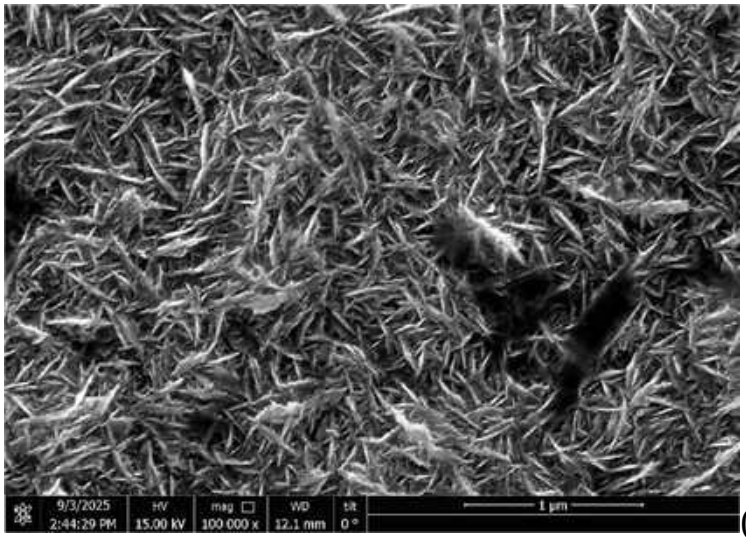
(***20***)

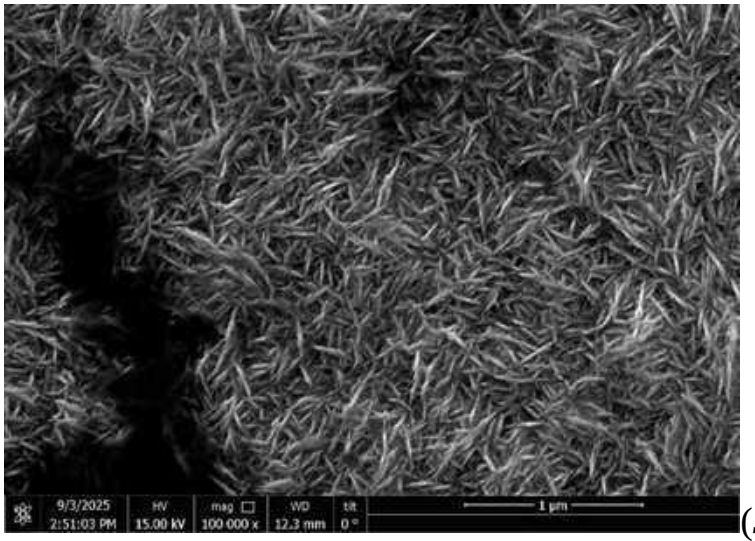
Fig. 6. SEM images of Ni coatings electrodeposited from the Ethaline-based electrolyte under various conditions. Magnification: 30k×; scale bar: 5 μm. Sample numbers correspond to the electrodeposition parameters listed in Table 2.

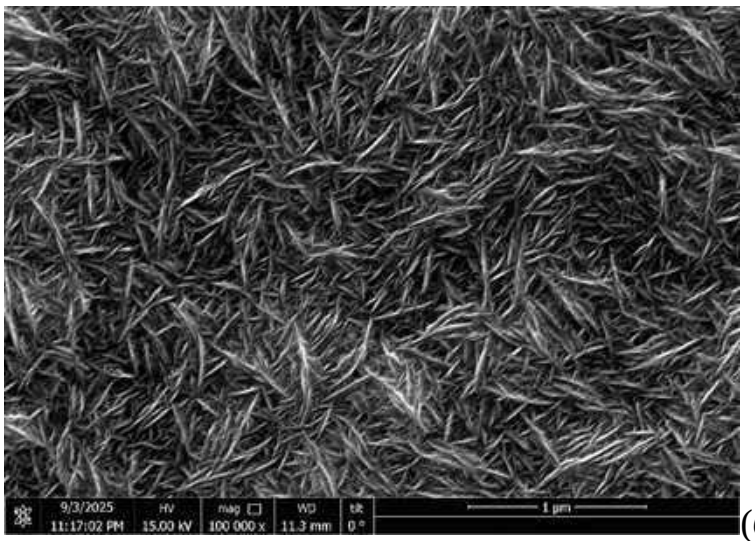

8/19/2025
2:49:09 PM
HV
20.00 kV
mag
100 000 x
WD
12.3 mm
tilt
0 °
1 µm
(***1***)

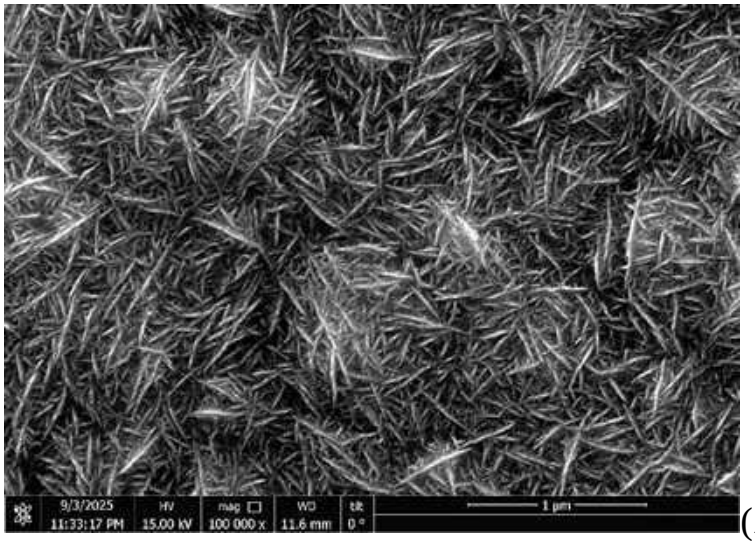

9/3/2025
1:54:36 PM
HV
15.00 kV
mag
100 000 x
WD
12.4 mm
tilt
0 °
1 µm
(***2***)

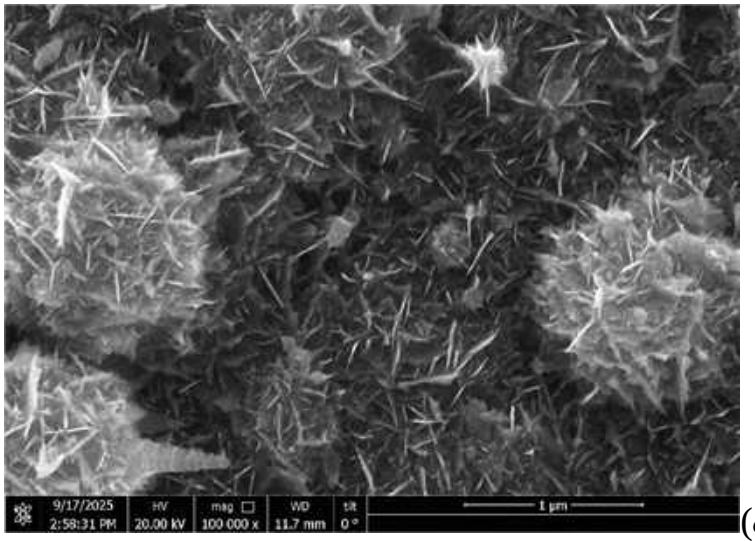

9/3/2025
2:24:03 PM
HV
15.00 kV
mag
100 000 x
WD
12.6 mm
tilt
0 °
1 µm
(***3***)

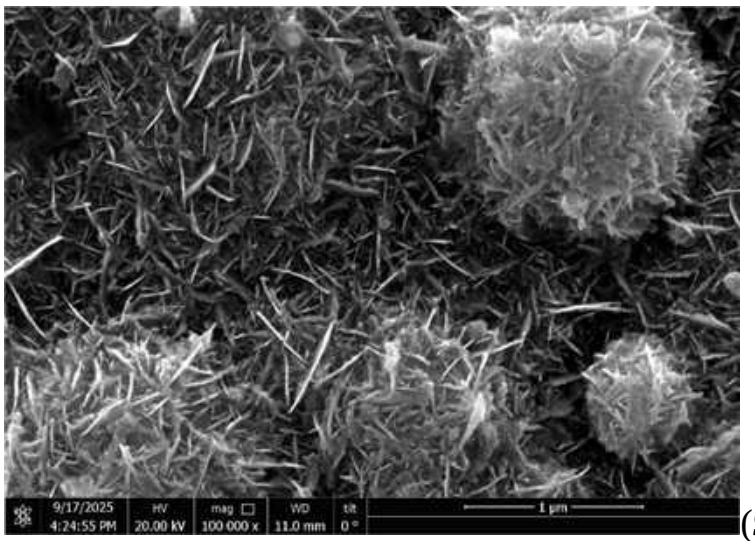

9/3/2025
2:44:29 PM
HV
15.00 kV
mag
100 000 x
WD
12.1 mm
tilt
0 °
1 µm
(*4*)

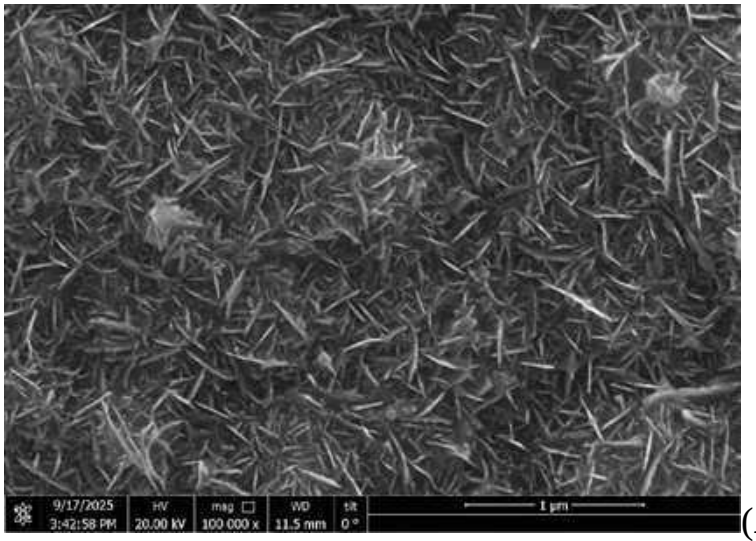

9/3/2025
2:51:03 PM
HV
15.00 kV
mag
100 000 x
WD
12.3 mm
tilt
0 °
1 µm
(*5*)

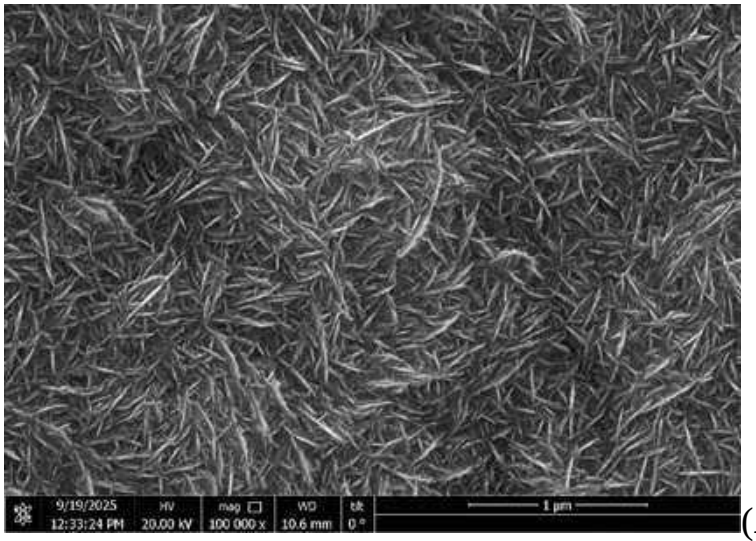

9/3/2025
11:17:02 PM
HV
15.00 kV
mag
100 000 x
WD
11.3 mm
tilt
0 °
1 µm
(*6*)

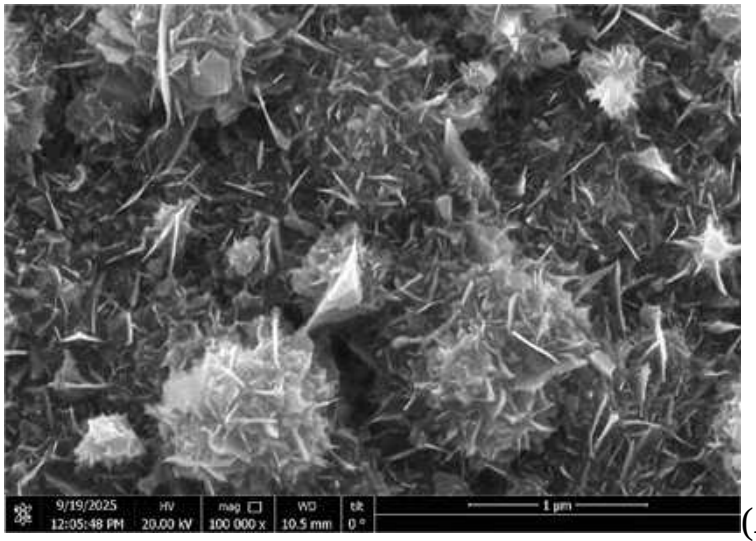

9/3/2025
11:33:17 PM
HV
15.00 kV
mag
100 000 x
WD
11.6 mm
tilt
0 °
1 µm
(***7***)

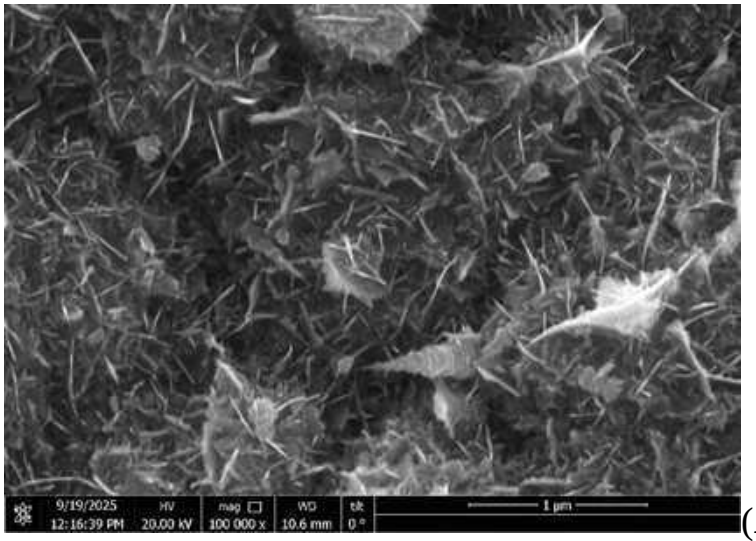

9/17/2025
2:58:31 PM
HV
20.00 kV
mag
100 000 x
WD
11.7 mm
tilt
0 °
1 µm
(***8***)

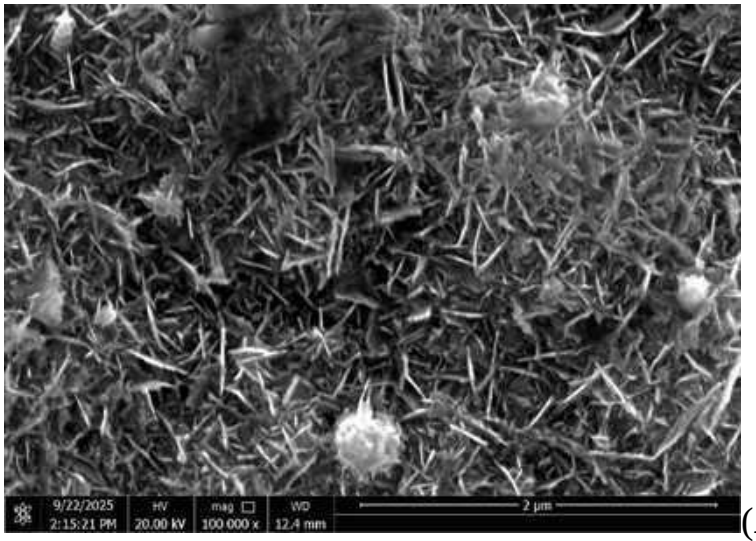

9/17/2025
4:24:55 PM
HV
20.00 kV
mag
100 000 x
WD
11.0 mm
tilt
0 °
1 µm
(***9***)

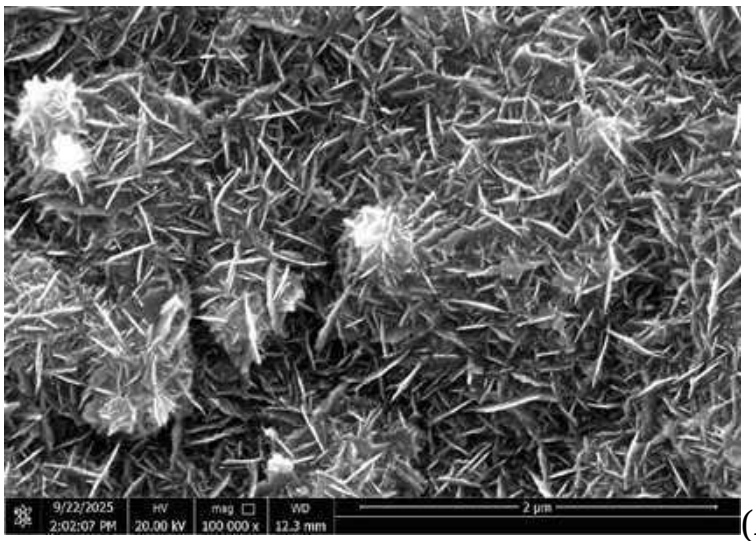

9/17/2025
3:42:58 PM
HV
20.00 kV
mag
100 000 x
WD
11.5 mm
tilt
0 °
1 µm
(***10***)

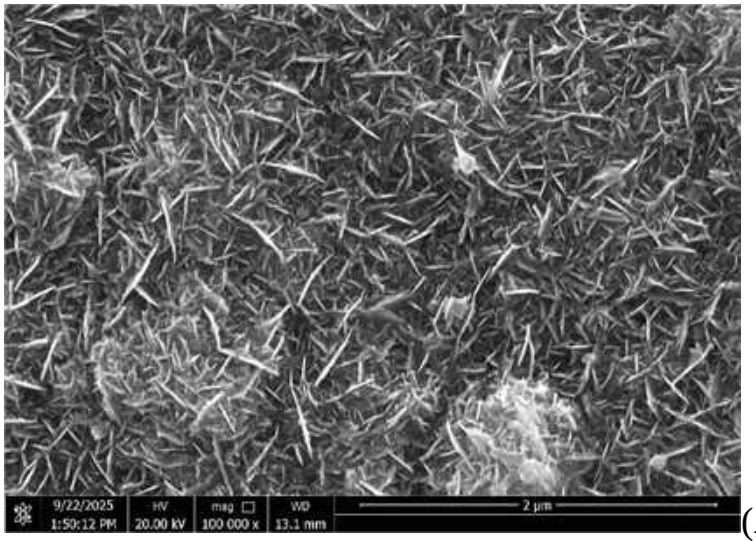

9/19/2025
12:33:24 PM
HV
20.00 kV
mag
100 000 x
WD
10.6 mm
tilt
0 °
1 µm
(***11***)

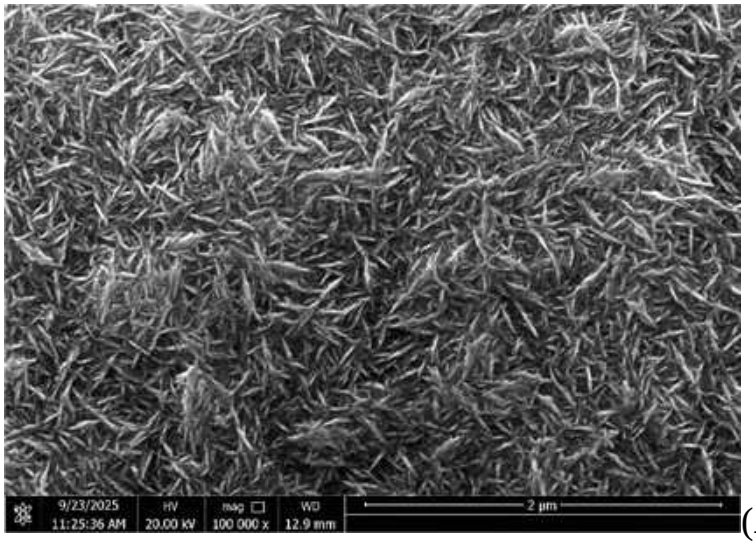

9/19/2025
12:05:48 PM
HV
20.00 kV
mag
100 000 x
WD
10.5 mm
tilt
0 °
1 µm
(***12***)

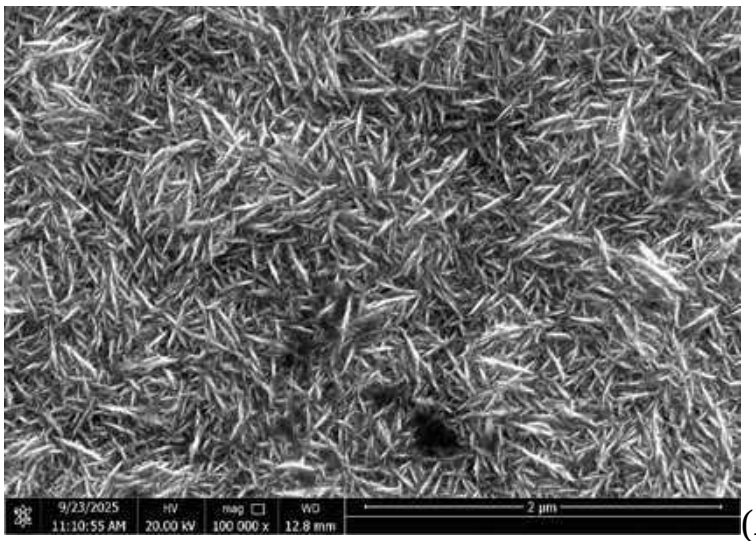

9/19/2025
12:16:39 PM
HV
20.00 kV
mag
100 000 x
WD
10.6 mm
tilt
0 °
1 µm
(***13***)

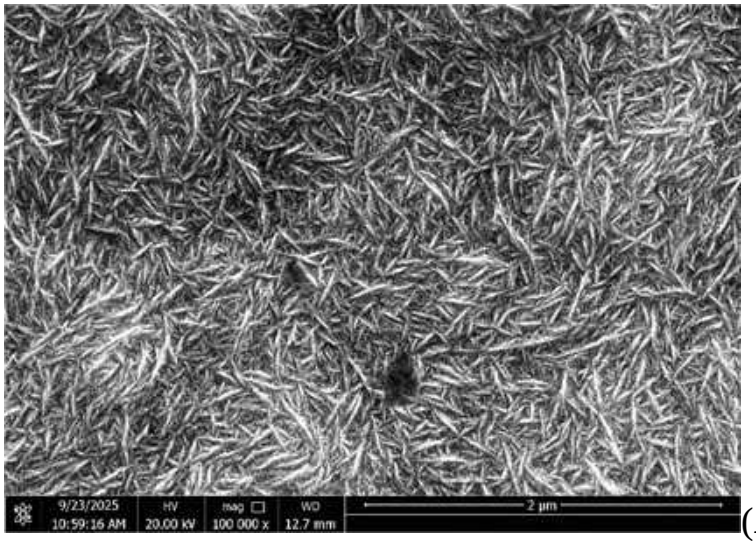

9/22/2025
2:15:21 PM
HV
20.00 kV
mag
100 000 x
WD
12.4 mm
2 µm
(***14***)


9/22/2025
2:02:07 PM
HV
20.00 kV
mag
100 000 x
WD
12.3 mm
2 µm
(***15***)


9/22/2025
1:50:12 PM
HV
20.00 kV
mag
100 000 x
WD
13.1 mm
2 µm
(***16***)


9/23/2025
11:25:36 AM
HV
20.00 kV
mag
100 000 x
WD
12.9 mm
2 µm
(***17***)

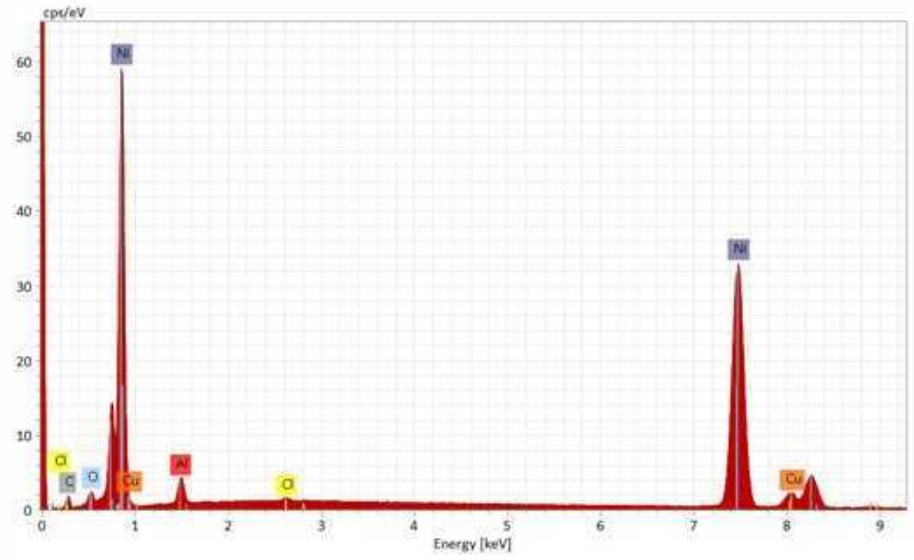

9/23/2025
11:10:55 AM
HV
20.00 kV
mag
100 000 x
WD
12.8 mm
2 µm
(***18***)



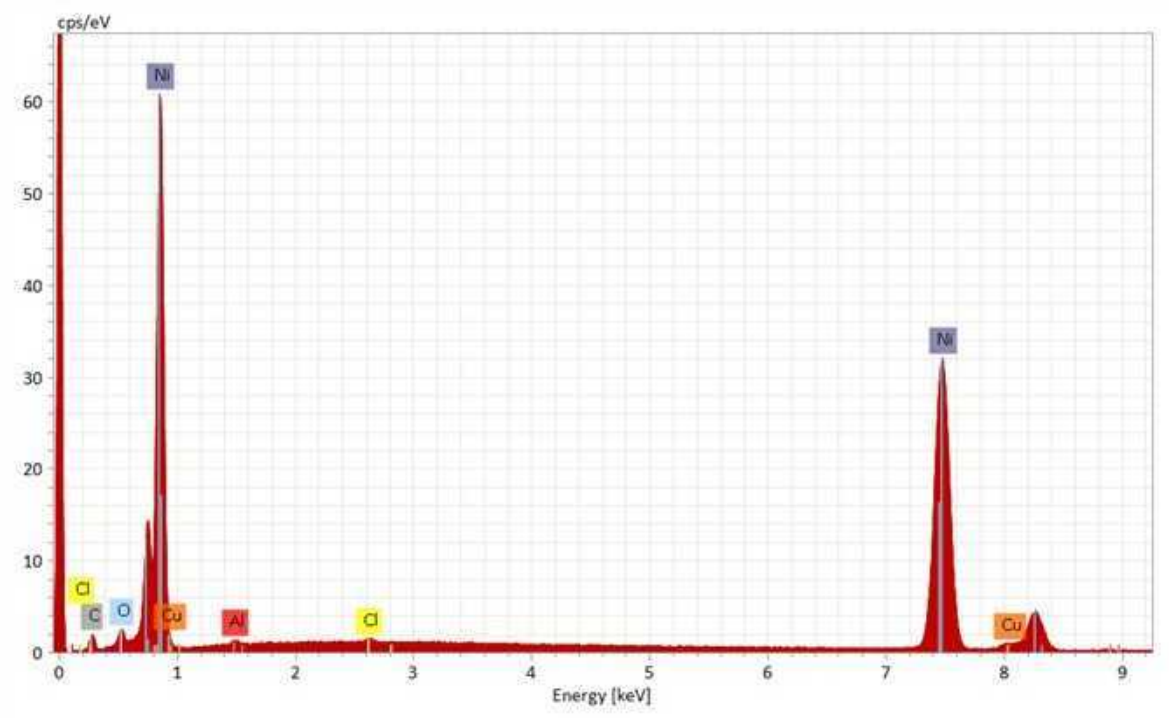
(***19***)

Fig. 7. SEM images of Ni coatings electrodeposited from the Ethaline-based electrolyte under various conditions. Magnification: 100k×; scale bar: 1 µm. Sample numbers correspond to the electrodeposition parameters listed in Table 2.

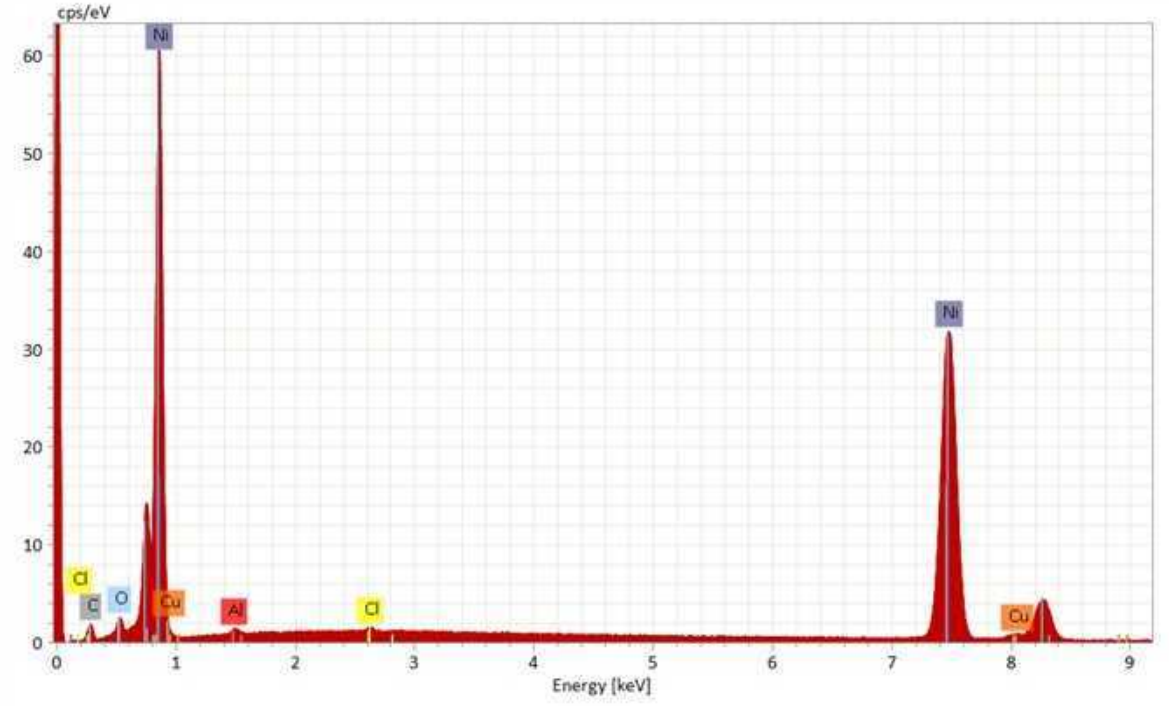
Surface composition is another key factor that can significantly influence the catalytic activity of the coating, as the presence of specific elements or impurities may affect adsorption, reaction kinetics, and overall stability. The EDX spectra of the obtained coatings are shown in Fig. 8, while the corresponding tables presenting the elemental composition of the deposited coatings are provided in Fig. 9.



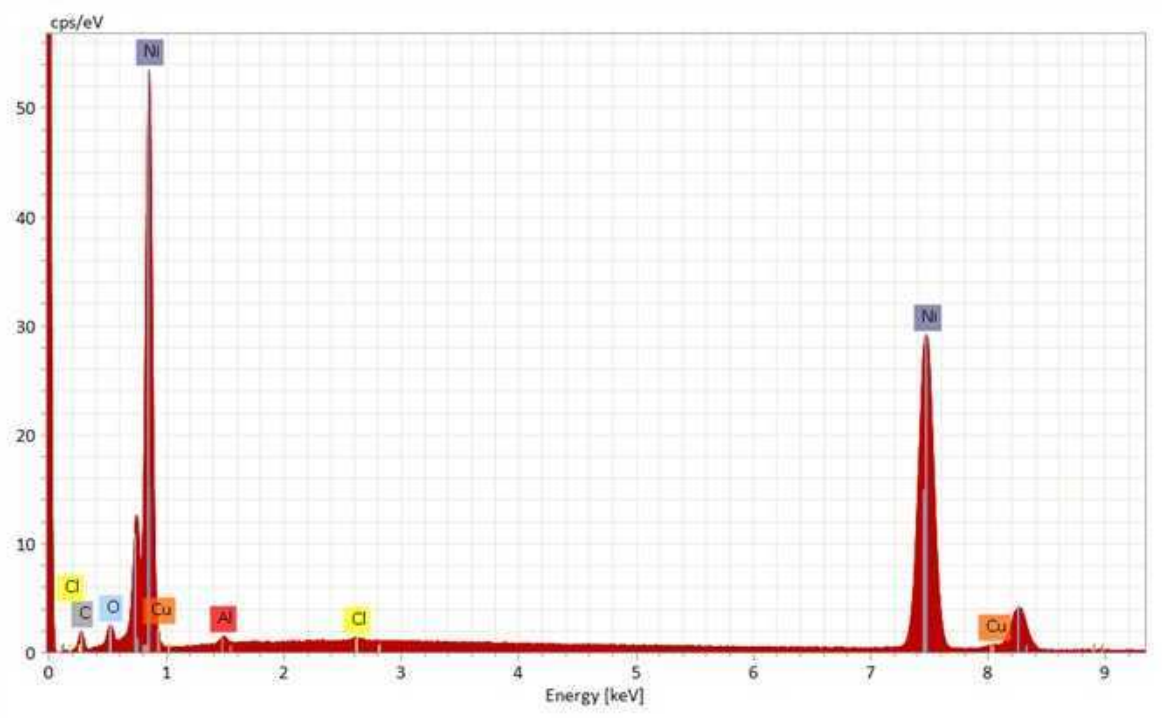
(***1***)


cps/eV
Ni
Ni
Cl
C
O
Cu
Al
Cl
Cu
Energy [keV]

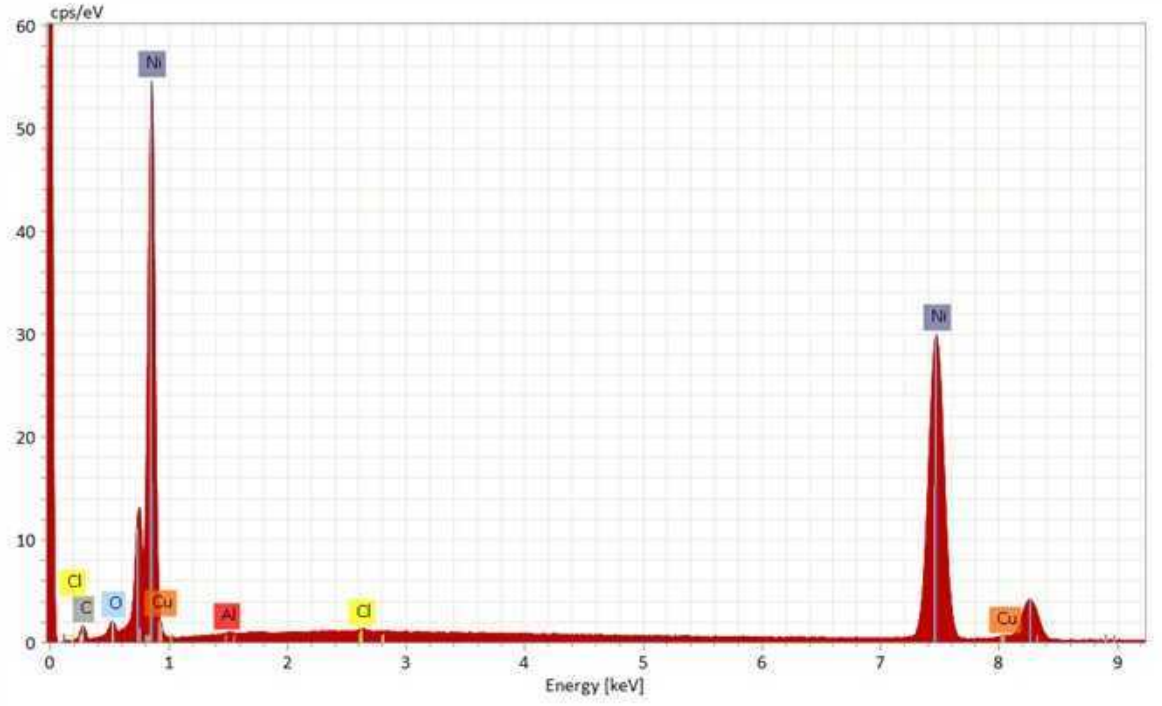
(*2*)


cps/eV
Ni
Ni
Cl
C
O
Cu
Al
Cl
Cu
Energy [keV]

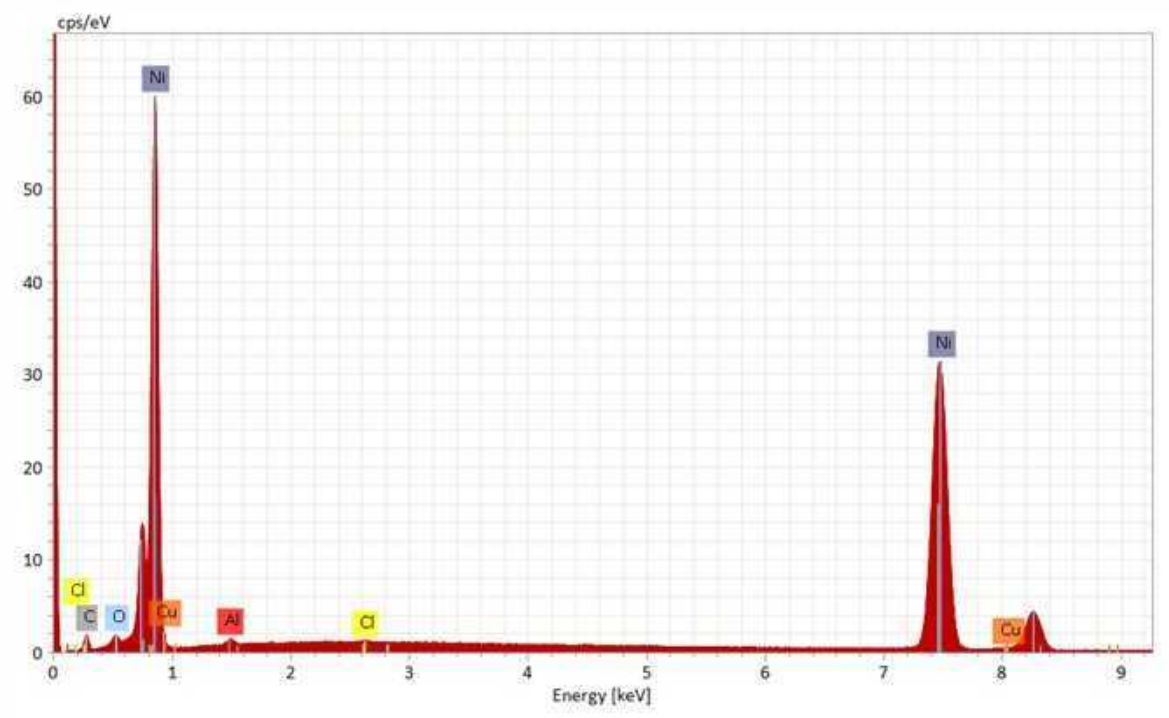
(*3*)


cps/eV
Ni
Ni
Cl
C
O
Cu
Al
Cl
Cu
Energy [keV]

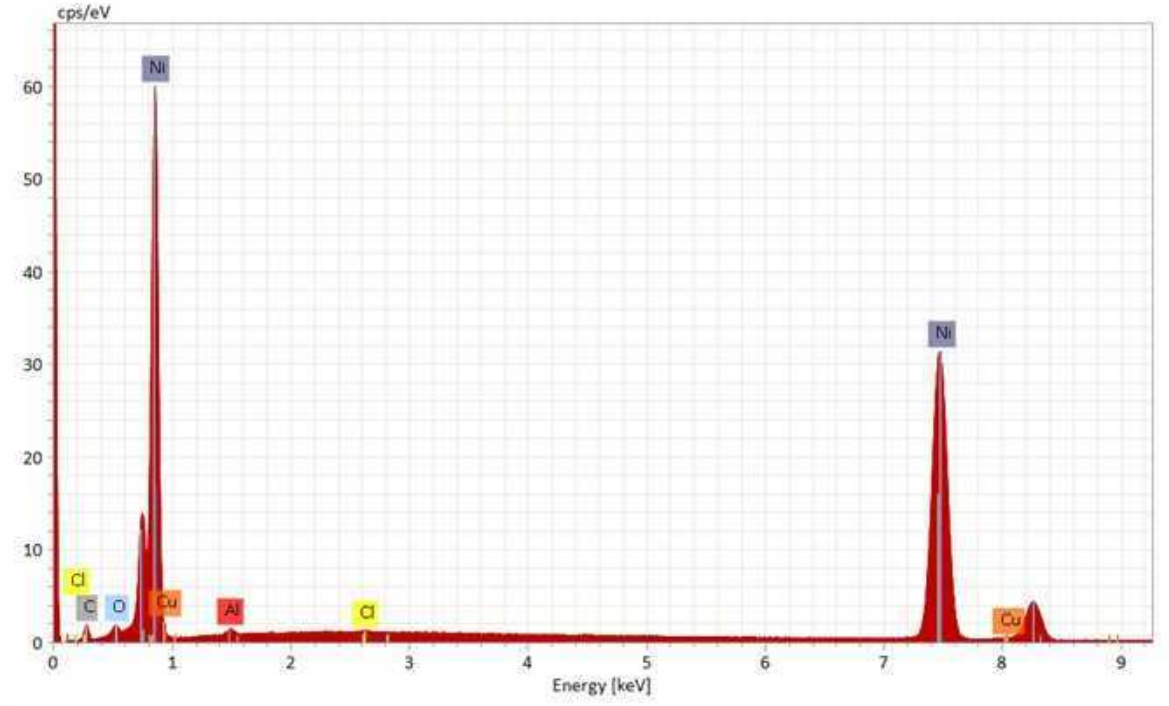
(***4***)


cps/eV
Ni
Ni
Cl
C
O
Cu
Al
Cl
Cu
Energy [keV]

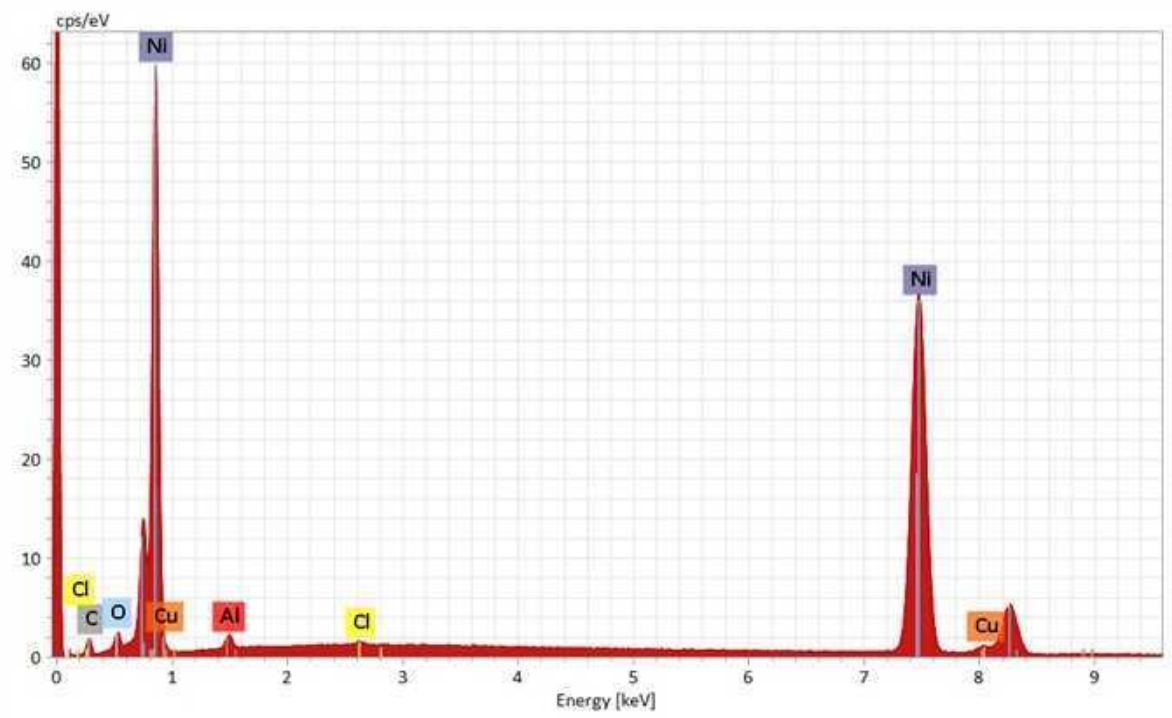
(***5***)


cps/eV
Ni
Ni
Cl
C
O
Cu
Al
Cl
Cu
Energy [keV]

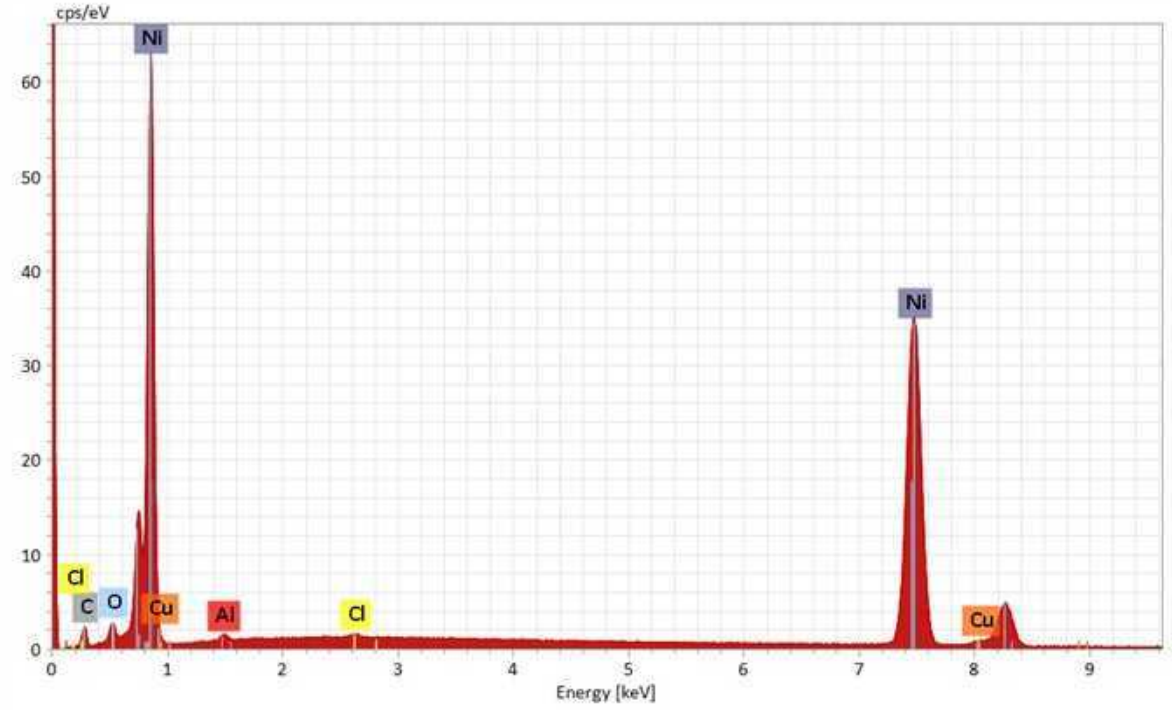
(*6*)


cps/eV
Ni
Ni
Cl
C
O
Cu
Al
Cl
Cu
Energy [keV]

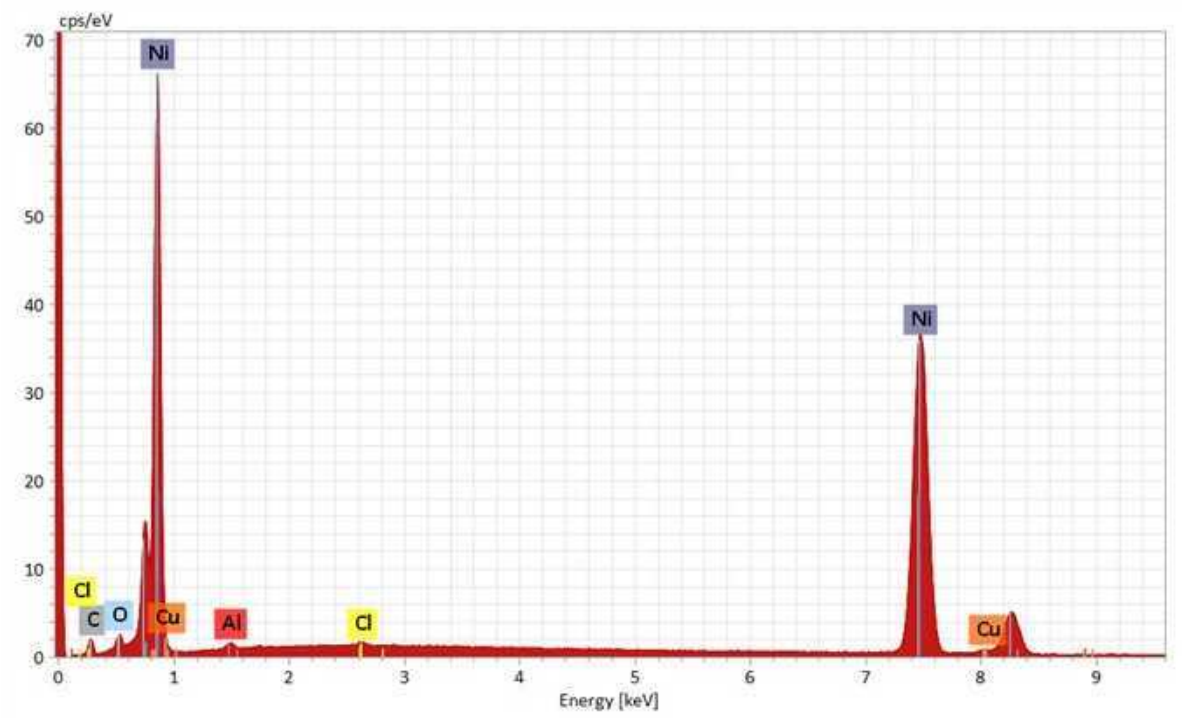
(*7*)


cps/eV
Ni
Ni
Cl
C
O
Cu
Al
Cl
Cu
Energy [keV]

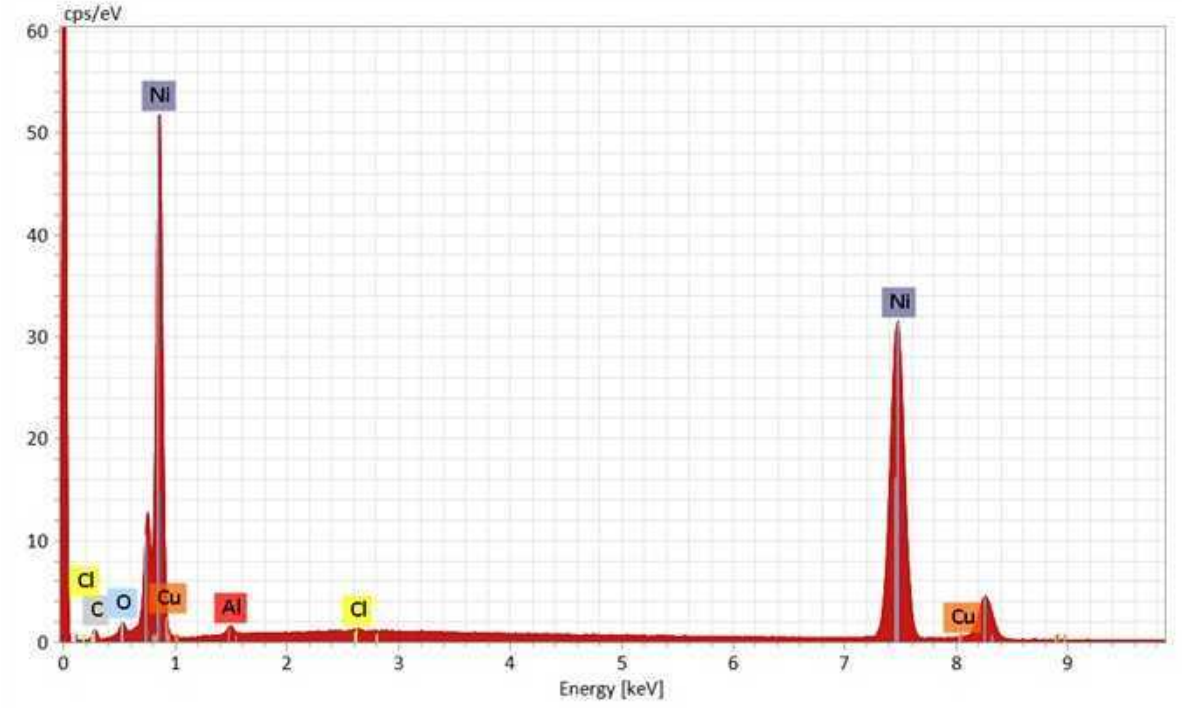
(***8***)


cps/eV
Ni
Ni
Cl
C
O
Cu
Al
Cl
Cu
Energy [keV]

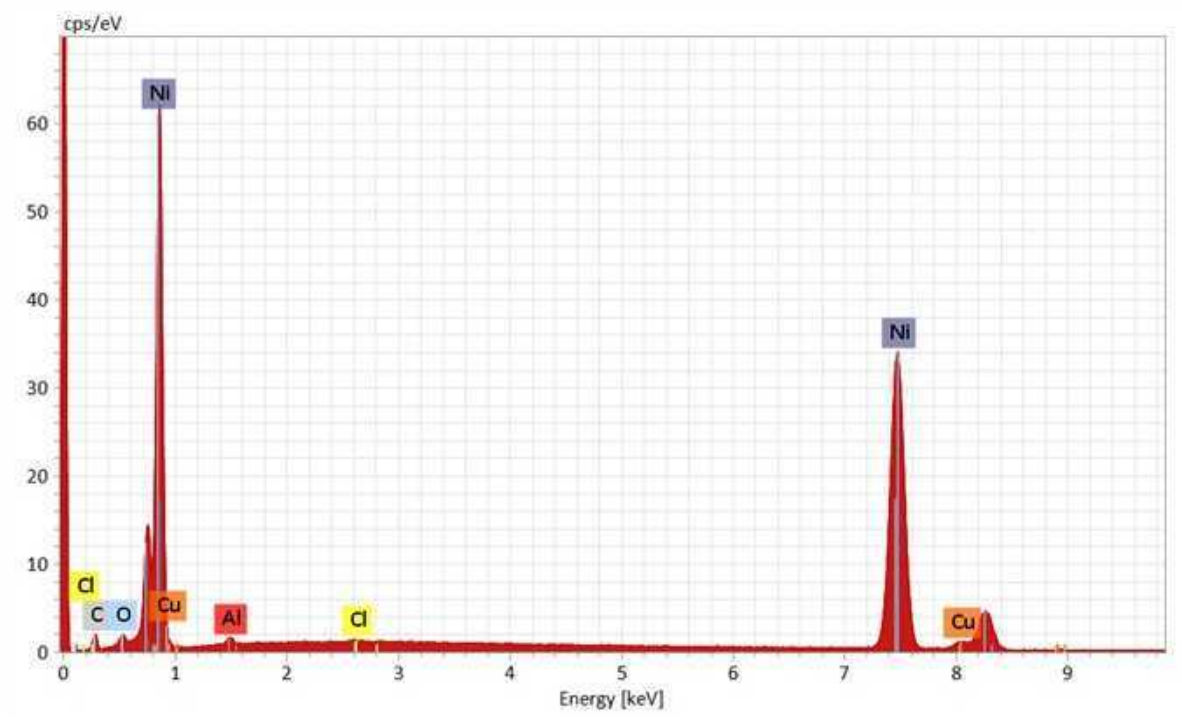
(***9***)


cps/eV
70
60
50
40
30
20
10
0
Ni
Ni
Cl
C
O
Cu
Al
Cl
Cu
0
1
2
3
4
5
6
7
8
9
Energy [keV]

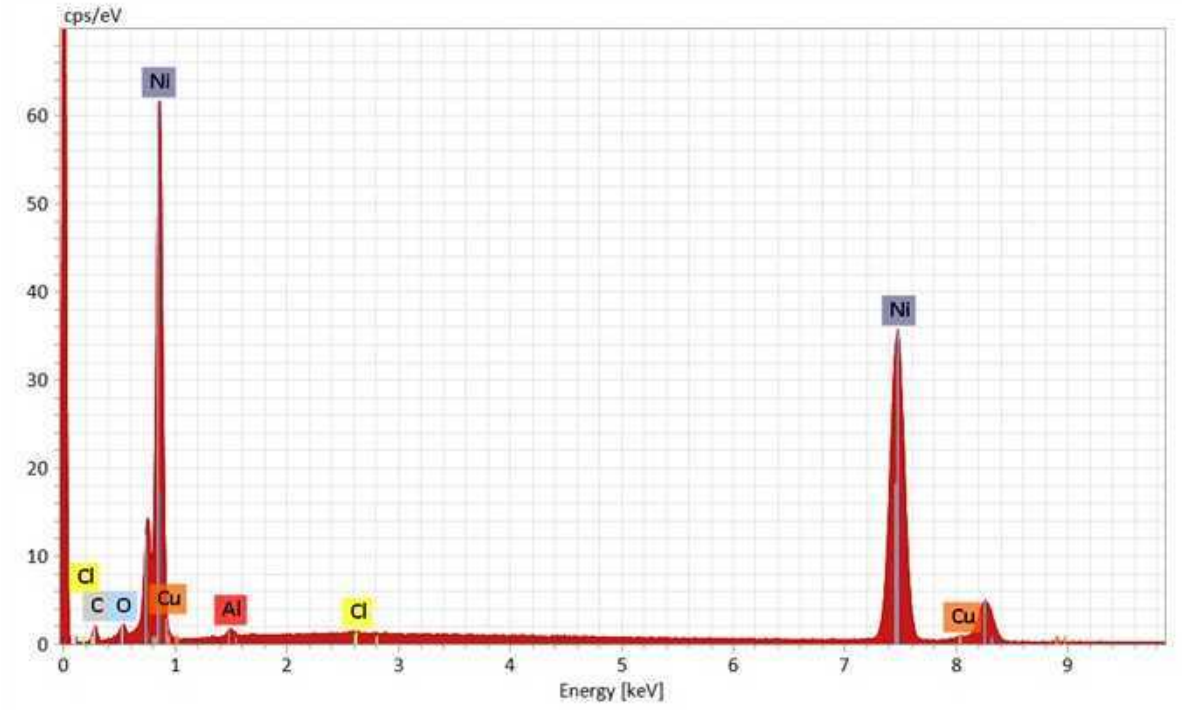
(***10***)


cps/eV
60
50
40
30
20
10
0
Ni
Ni
Cl
C
O
Cu
Al
Cl
Cu
0
1
2
3
4
5
6
7
8
9
Energy [keV]

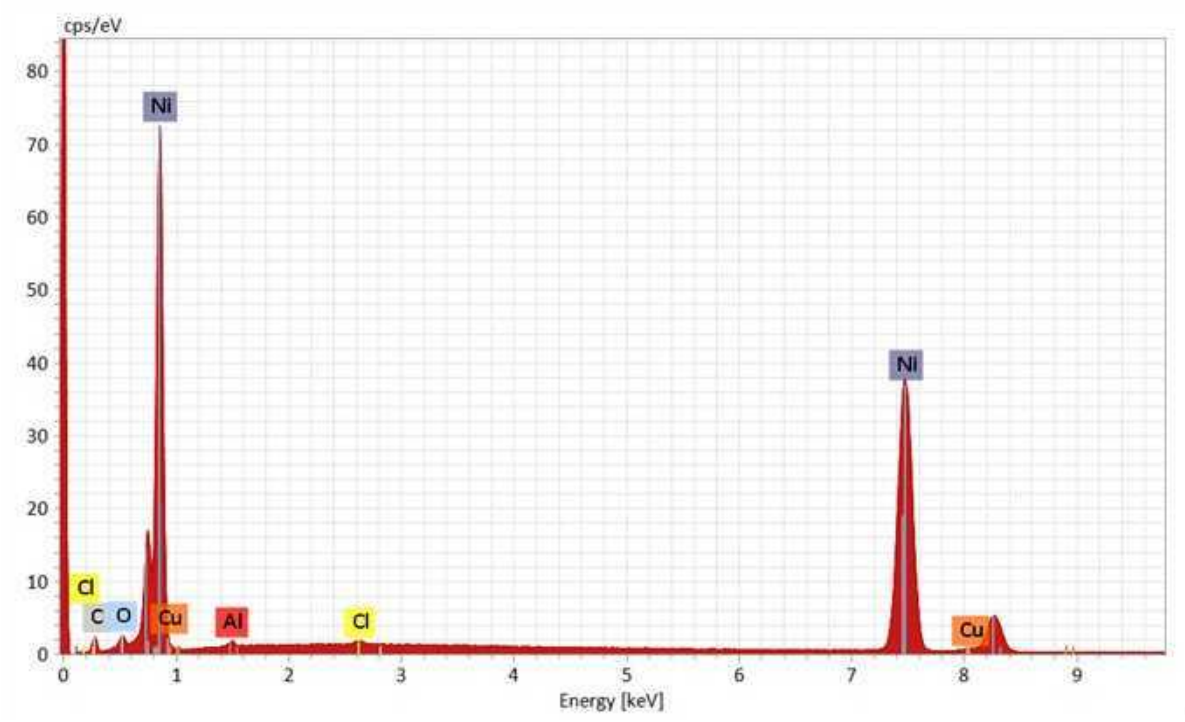
(***11***)


cps/eV
Ni
Ni
Cl
C O
Cu
Al
Cl
Cu
0
10
20
30
40
50
60
0 1 2 3 4 5 6 7 8 9
Energy [keV]

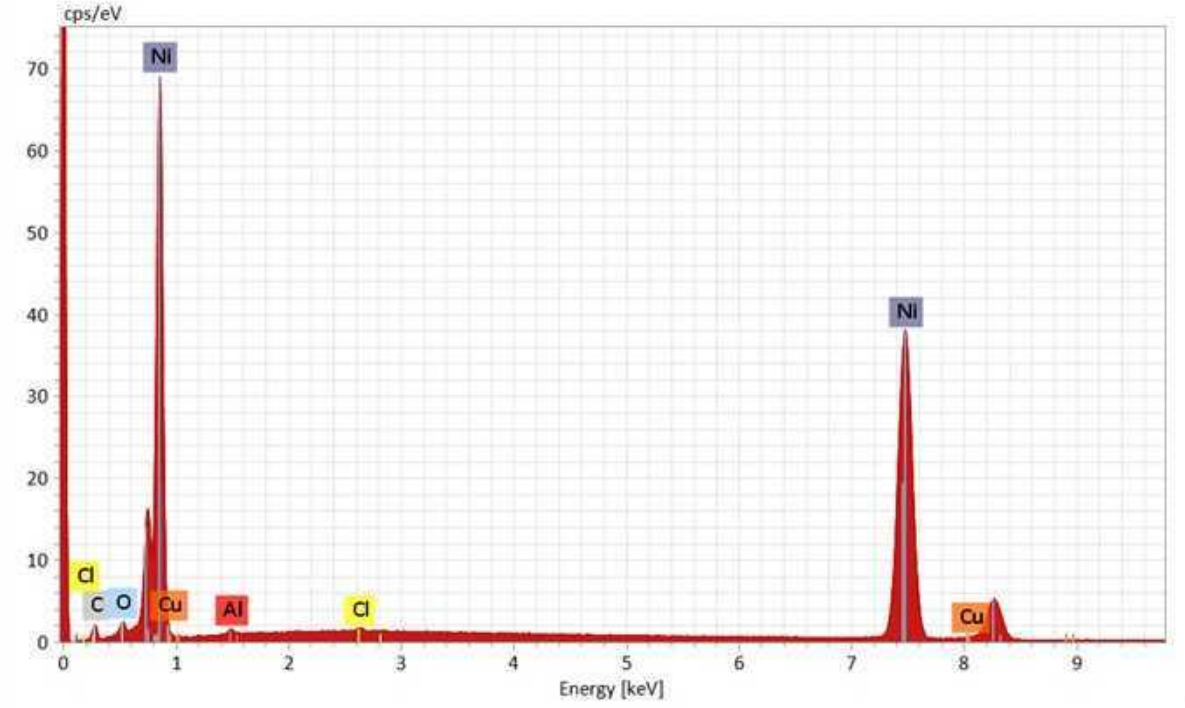
(***12***)


cps/eV
Ni
Ni
Cl
C O
Cu
Al
Cl
Cu
0
10
20
30
40
50
60
0 1 2 3 4 5 6 7 8 9
Energy [keV]

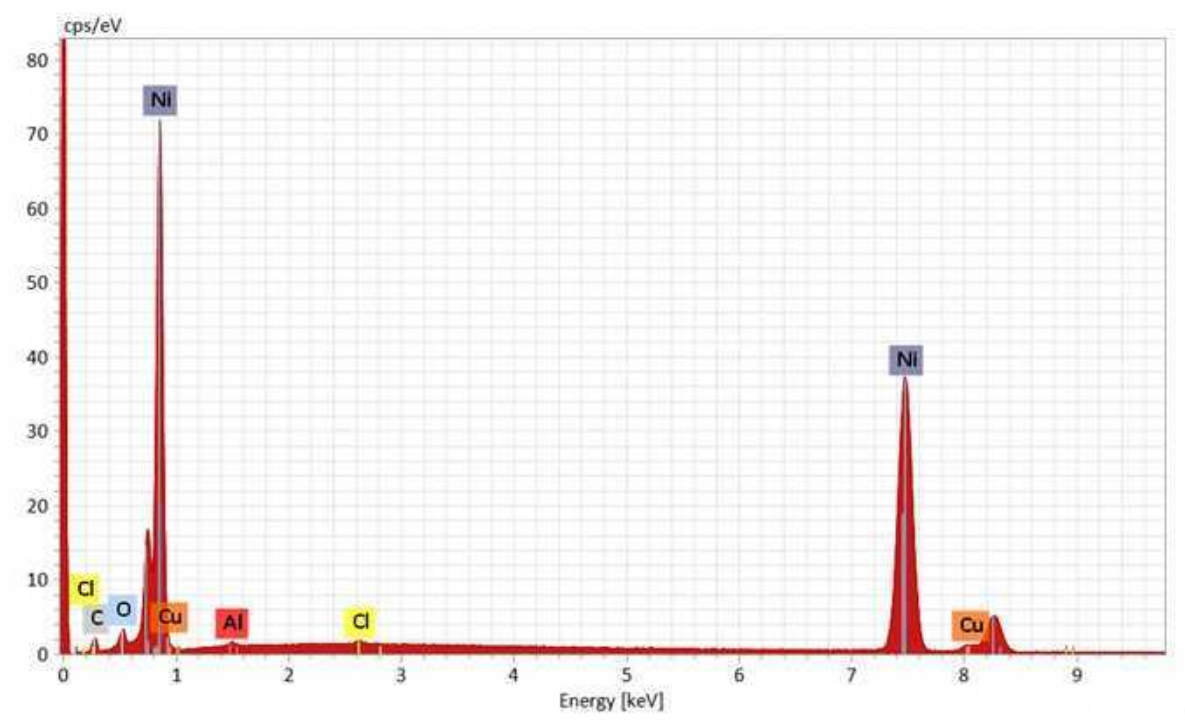
(***13***)


cps/eV
Ni
Ni
Cl
C O
Cu
Al
Cl
Cu
Energy [keV]

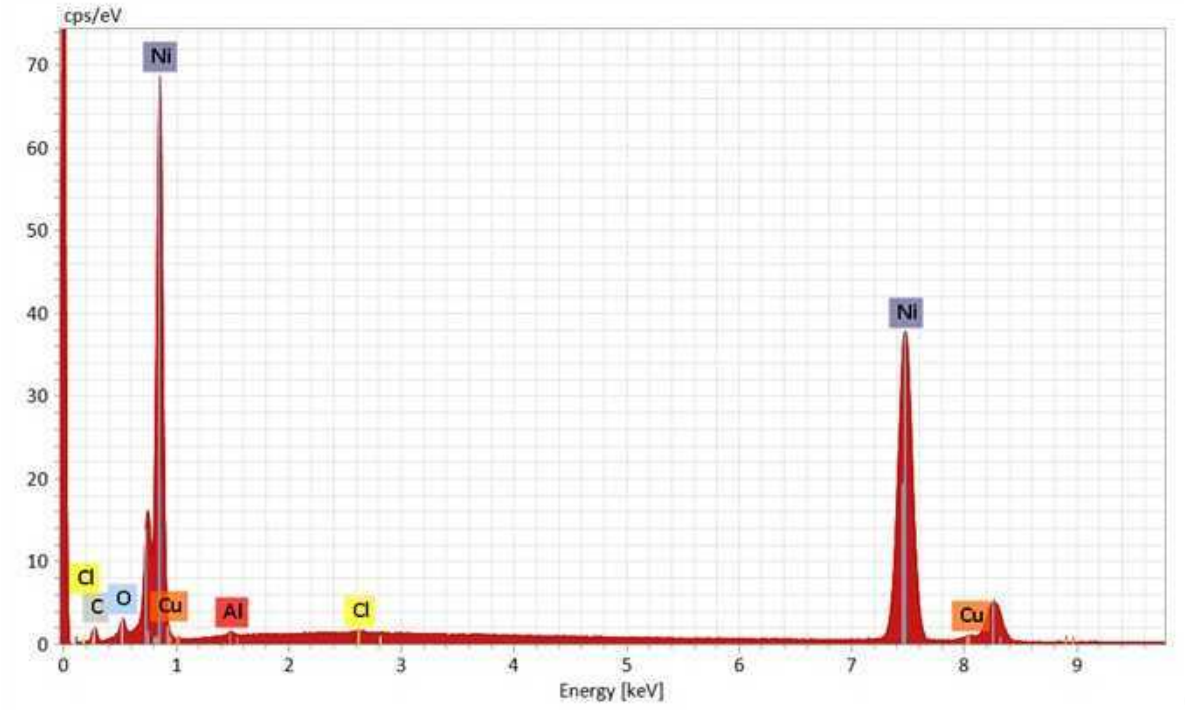
(***14***)


cps/eV
Ni
Ni
Cl
C O
Cu
Al
Cl
Cu
Energy [keV]

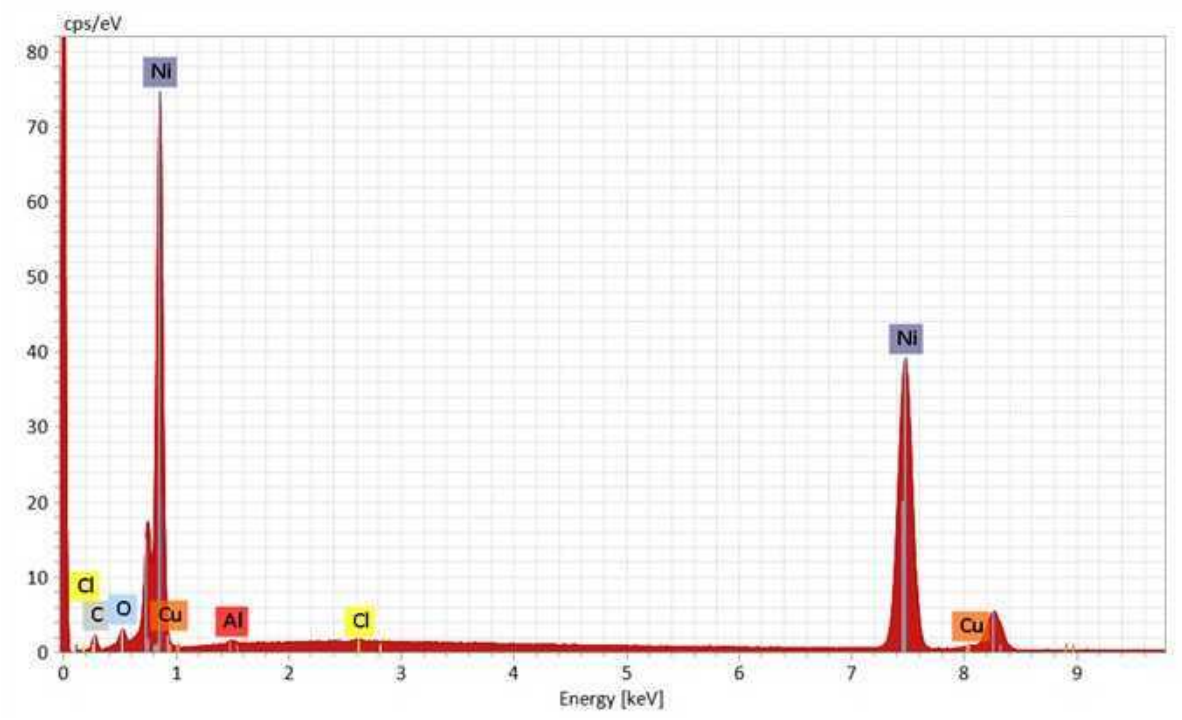
(***15***)


cps/eV
Ni
Ni
Cl
C
O
Cu
Al
Cl
Cu
Energy [keV]

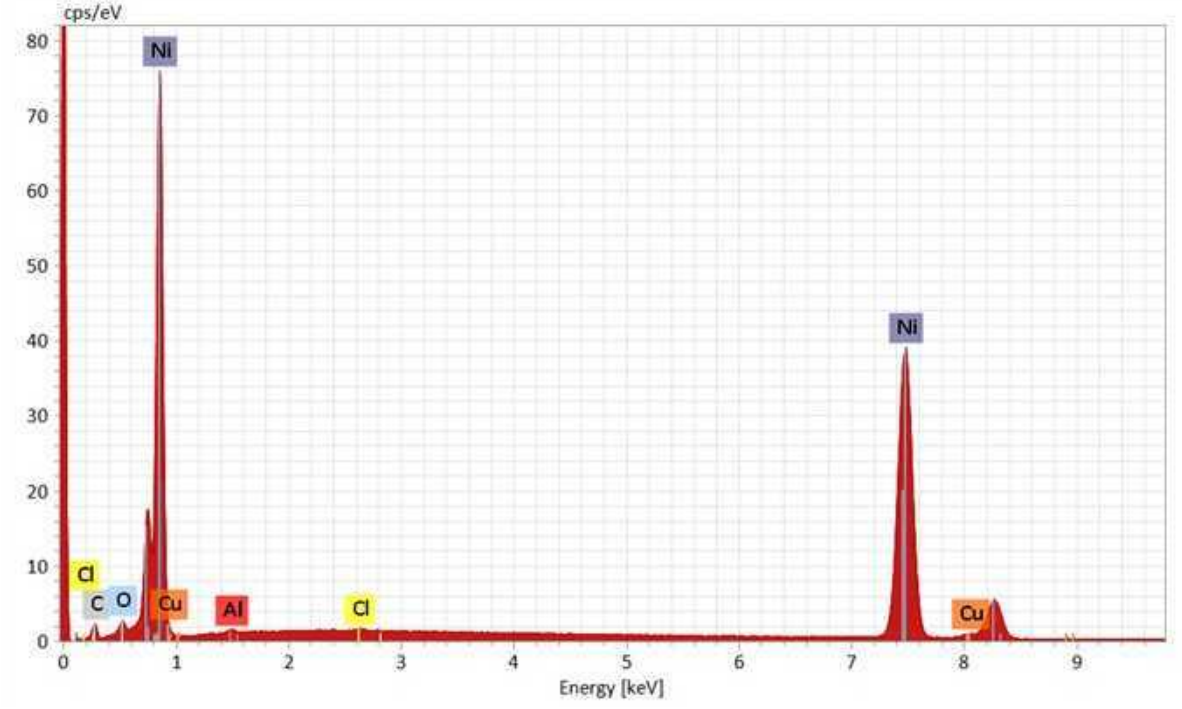
(***16***)


cps/eV
Ni
Ni
Cl
C
O
Cu
Al
Cl
Cu
Energy [keV]

(***17***)



(***18***)



(***19***)

Fig. 8. EDX spectra of Ni coatings electrodeposited from the Ethaline-based electrolyte under various conditions. Sample numbers correspond to the electrodeposition parameters listed in Table 2.

1_20kV

Element	At. No.	Netto	Mass [%]	Mass Norm. [%]	Atom [%]	abs. error [%] (1 sigma)	rel. error [%] (1 sigma)
Carbon	6	3619	4.94	5.16	19.91	0.29	5.81
Oxygen	8	3715	1.34	1.40	4.05	0.07	5.52
Aluminium	13	13796	2.58	2.69	4.63	0.11	4.36
Chlorine	17	1856	0.20	0.21	0.27	0.01	7.50
Nickel	28	295347	80.64	84.12	66.46	1.49	1.85
Copper	29	17601	6.16	6.42	4.69	0.14	2.25
		Sum	**95.86**	**100.00**	**100.00**		

(***1***)

2_20kV

Element	At. No.	Netto	Mass [%]	Mass Norm. [%]	Atom [%]	abs. error [%] (1 sigma)	rel. error [%] (1 sigma)
Carbon	6	4238	5.84	6.08	23.16	0.34	5.83
Oxygen	8	4129	1.56	1.62	4.64	0.08	5.45
Aluminium	13	1778	0.32	0.34	0.57	0.03	7.92
Chlorine	17	1974	0.21	0.22	0.28	0.02	7.19
Nickel	28	300456	85.57	89.04	69.40	1.61	1.88
Copper	29	7110	2.59	2.70	1.94	0.07	2.84
		Sum	**96.10**	**100.00**	**100.00**		

(***2***)

3_20kV

Element	At. No.	Netto	Mass [%]	Mass Norm. [%]	Atom [%]	abs. error [%] (1 sigma)	rel. error [%] (1 sigma)
Carbon	6	3952	5.47	5.72	21.99	0.32	5.87
Oxygen	8	4092	1.54	1.61	4.64	0.08	5.46
Aluminium	13	2243	0.41	0.43	0.74	0.03	7.03
Chlorine	17	1720	0.18	0.19	0.25	0.01	7.98
Nickel	28	302615	86.15	90.04	70.91	1.62	1.88
Copper	29	5329	1.93	2.02	1.47	0.06	3.15
		Sum	**95.69**	**100.00**	**100.00**		

(***3***)

4_20kV

Element	At. No.	Netto	Mass [%]	Mass Norm. [%]	Atom [%]	abs. error [%] (1 sigma)	rel. error [%] (1 sigma)
Carbon	6	4425	5.87	6.24	23.43	0.34	5.80
Oxygen	8	5069	1.85	1.97	5.54	0.10	5.28
Aluminium	13	2985	0.55	0.58	0.97	0.03	6.25
Chlorine	17	2000	0.21	0.22	0.29	0.02	7.15
Nickel	28	306991	84.24	89.62	68.81	1.57	1.86
Copper	29	3716	1.28	1.37	0.97	0.05	3.83
		Sum	**94.00**	**100.00**	**100.00**		

(***4***)

5_20kV

Element	At. No.	Netto	Mass [%]	Mass Norm. [%]	Atom [%]	abs. error [%] (1 sigma)	rel. error [%] (1 sigma)
Carbon	6	4009	5.40	5.73	22.24	0.32	5.97
Oxygen	8	3376	1.24	1.31	3.83	0.07	5.62
Aluminium	13	533	0.10	0.10	0.18	0.02	17.47
Chlorine	17	1342	0.14	0.15	0.20	0.01	9.69
Nickel	28	310907	86.25	91.63	72.76	1.61	1.86
Copper	29	2845	1.01	1.07	0.79	0.05	4.51
		Sum	**94.14**	**100.00**	**100.00**		

(***5***)

6_20kV

Element	At. No.	Netto	Mass [%]	Mass Norm. [%]	Atom [%]	abs. error [%] (1 sigma)	rel. error [%] (1 sigma)
Carbon	6	3713	5.14	5.49	21.55	0.30	5.86
Oxygen	8	2363	0.88	0.94	2.78	0.05	6.20
Aluminium	13	2385	0.44	0.47	0.82	0.03	6.85
Chlorine	17	982	0.11	0.11	0.15	0.01	11.59
Nickel	28	305062	86.36	92.21	74.12	1.61	1.87
Copper	29	2005	0.73	0.78	0.58	0.04	5.59
		Sum	**93.66**	**100.00**	**100.00**		

(***6***)

7_20kV

Element	At. No.	Netto	Mass [%]	Mass Norm. [%]	Atom [%]	abs. error [%] (1 sigma)	rel. error [%] (1 sigma)
Carbon	6	2873	3.73	3.99	16.42	0.22	6.00
Oxygen	8	2877	0.97	1.04	3.21	0.06	5.77
Aluminium	13	1984	0.42	0.45	0.82	0.03	7.31
Chlorine	17	520	0.06	0.06	0.08	0.01	20.01
Nickel	28	334423	87.64	93.88	79.02	1.59	1.82
Copper	29	1603	0.54	0.57	0.45	0.04	6.84
		Sum	**93.35**	**100.00**	**100.00**		

(***7***)

8_20kV

Element	At. No.	Netto	Mass [%]	Mass Norm. [%]	Atom [%]	abs. error [%] (1 sigma)	rel. error [%] (1 sigma)
Carbon	6	3635	4.64	5.01	19.69	0.27	5.88
Oxygen	8	3764	1.28	1.38	4.07	0.07	5.47
Aluminium	13	5128	1.03	1.11	1.95	0.05	5.20
Chlorine	17	1790	0.19	0.21	0.28	0.01	7.68
Nickel	28	321828	83.18	89.89	72.24	1.51	1.82
Copper	29	6662	2.21	2.39	1.77	0.06	2.90
		Sum	**92.53**	**100.00**	**100.00**		

(***8***)

9_20kV

Element	At. No.	Netto	Mass [%]	Mass Norm. [%]	Atom [%]	abs. error [%] (1 sigma)	rel. error [%] (1 sigma)
Carbon	6	4696	6.11	6.53	24.46	0.35	5.78
Oxygen	8	4462	1.61	1.72	4.83	0.09	5.37
Aluminium	13	2419	0.46	0.49	0.82	0.03	6.78
Chlorine	17	1931	0.20	0.22	0.28	0.01	7.31
Nickel	28	309368	83.46	89.26	68.36	1.54	1.85
Copper	29	4853	1.66	1.77	1.25	0.05	3.29
		Sum	**93.49**	**100.00**	**100.00**		

(***9***)

10_20kV

Element	At. No.	Netto	Mass [%]	Mass Norm. [%]	Atom [%]	abs. error [%] (1 sigma)	rel. error [%] (1 sigma)
Carbon	6	3678	4.96	5.32	20.87	0.29	5.89
Oxygen	8	3126	1.13	1.21	3.58	0.06	5.73
Aluminium	13	2413	0.47	0.50	0.87	0.03	6.76
Chlorine	17	1801	0.19	0.21	0.28	0.01	7.70
Nickel	28	309659	85.23	91.37	73.38	1.58	1.85
Copper	29	3722	1.30	1.39	1.03	0.05	3.83
		Sum	**93.28**	**100.00**	**100.00**		

(***10***)

11_20kV

Element	At. No.	Netto	Mass [%]	Mass Norm. [%]	Atom [%]	abs. error [%] (1 sigma)	rel. error [%] (1 sigma)
Carbon	6	2730	3.68	3.94	16.14	0.22	5.96
Oxygen	8	2981	1.04	1.12	3.43	0.06	5.75
Aluminium	13	3484	0.70	0.75	1.38	0.04	5.84
Chlorine	17	1133	0.12	0.13	0.18	0.01	11.65
Nickel	28	322031	87.18	93.38	78.34	1.60	1.84
Copper	29	1861	0.64	0.69	0.53	0.04	6.03
		Sum	**93.37**	**100.00**	**100.00**		

(***11***)

12_20kV

Element	At. No.	Netto	Mass [%]	Mass Norm. [%]	Atom [%]	abs. error [%] (1 sigma)	rel. error [%] (1 sigma)
Carbon	6	4151	5.55	5.92	22.95	0.33	5.91
Oxygen	8	2410	0.88	0.94	2.73	0.05	6.15
Aluminium	13	2993	0.57	0.61	1.05	0.04	6.19
Chlorine	17	1252	0.14	0.14	0.19	0.02	15.27
Nickel	28	305567	83.71	89.41	70.90	1.56	1.86
Copper	29	7889	2.78	2.97	2.18	0.08	2.72
		Sum	**93.62**	**100.00**	**100.00**		

(***12***)

13_20kV

Element	At. No.	Netto	Mass [%]	Mass Norm. [%]	Atom [%]	abs. error [%] (1 sigma)	rel. error [%] (1 sigma)
Carbon	6	4059	5.38	5.70	22.13	0.31	5.84
Oxygen	8	3068	1.10	1.17	3.41	0.06	5.75
Aluminium	13	2952	0.58	0.61	1.06	0.04	6.21
Chlorine	17	1490	0.16	0.17	0.23	0.01	8.81
Nickel	28	314347	85.28	90.49	71.82	1.57	1.84
Copper	29	5027	1.75	1.85	1.36	0.06	3.23
		Sum	**94.25**	**100.00**	**100.00**		

(***13***)

14_20kV

Element	At. No.	Netto	Mass [%]	Mass Norm. [%]	Atom [%]	abs. error [%] (1 sigma)	rel. error [%] (1 sigma)
Carbon	6	4266	6.18	6.45	24.48	0.36	5.88
Oxygen	8	2833	1.14	1.19	3.38	0.07	5.97
Aluminium	13	2120	0.41	0.43	0.72	0.03	7.20
Chlorine	17	2181	0.25	0.26	0.33	0.02	6.61
Nickel	28	290426	86.77	90.55	70.28	1.64	1.89
Copper	29	2823	1.08	1.12	0.81	0.05	4.44
		Sum	**95.82**	**100.00**	**100.00**		

(***14***)

15_20kV

Element	At. No.	Netto	Mass [%]	Mass Norm. [%]	Atom [%]	abs. error [%] (1 sigma)	rel. error [%] (1 sigma)
Carbon	6	3810	5.44	5.75	22.30	0.32	5.91
Oxygen	8	2856	1.11	1.18	3.42	0.07	5.91
Aluminium	13	1767	0.35	0.37	0.64	0.03	7.83
Chlorine	17	1371	0.15	0.16	0.22	0.01	9.36
Nickel	28	295982	86.73	91.64	72.76	1.63	1.88
Copper	29	2276	0.85	0.90	0.66	0.04	5.09
		Sum	**94.64**	**100.00**	**100.00**		

(***15***)

16_20kV

Element	At. No.	Netto	Mass [%]	Mass Norm. [%]	Atom [%]	abs. error [%] (1 sigma)	rel. error [%] (1 sigma)
Carbon	6	4121	5.93	6.18	23.25	0.34	5.73
Oxygen	8	5052	2.00	2.09	5.90	0.11	5.26
Aluminium	13	1697	0.32	0.33	0.55	0.03	8.12
Chlorine	17	1896	0.21	0.22	0.28	0.02	7.34
Nickel	28	284156	84.76	88.42	68.05	1.60	1.89
Copper	29	6991	2.65	2.76	1.96	0.08	2.84
		Sum	**95.86**	**100.00**	**100.00**		

(***16***)

17_20kV

Element	At. No.	Netto	Mass [%]	Mass Norm. [%]	Atom [%]	abs. error [%] (1 sigma)	rel. error [%] (1 sigma)
Carbon	6	4012	5.65	5.93	22.66	0.33	5.78
Oxygen	8	4150	1.60	1.68	4.83	0.09	5.39
Aluminium	13	1751	0.35	0.37	0.62	0.03	7.89
Chlorine	17	927	0.10	0.11	0.14	0.01	12.10
Nickel	28	294166	85.60	89.91	70.31	1.60	1.87
Copper	29	5131	1.91	2.00	1.45	0.06	3.22
		Sum	**95.21**	**100.00**	**100.00**		

(***17***)

18_20kV

Element	At. No.	Netto	Mass [%]	Mass Norm. [%]	Atom [%]	abs. error [%] (1 sigma)	rel. error [%] (1 sigma)
Carbon	6	4052	5.86	6.14	23.32	0.34	5.78
Oxygen	8	4021	1.61	1.68	4.79	0.09	5.44
Aluminium	13	1359	0.26	0.27	0.46	0.03	9.97
Chlorine	17	894	0.10	0.10	0.13	0.01	12.42
Nickel	28	287680	86.33	90.33	70.24	1.64	1.89
Copper	29	3673	1.42	1.48	1.07	0.05	3.78
		Sum	**95.58**	**100.00**	**100.00**		

(***18***)

19_20kV

Element	At. No.	Netto	Mass [%]	Mass Norm. [%]	Atom [%]	abs. error [%] (1 sigma)	rel. error [%] (1 sigma)
Carbon	6	3944	5.75	6.05	23.32	0.35	6.07
Oxygen	8	2685	1.08	1.13	3.28	0.06	5.96
Aluminium	13	1191	0.22	0.23	0.40	0.02	10.00
Chlorine	17	935	0.11	0.11	0.14	0.01	11.81
Nickel	28	286310	86.14	90.64	71.52	1.63	1.90
Copper	29	4529	1.74	1.83	1.34	0.06	3.43
		Sum	**95.03**	**100.00**	**100.00**		

(***19***)

Fig. 9. Elemental composition of Ni coatings electrodeposited from the Ethaline-based electrolyte under different conditions. Sample numbers correspond to the electrodeposition parameters listed in Table 2.

Surface analysis indicated that variations in temperature and current density had almost no effect on the chemical composition of the coating surfaces. As expected, nickel was identified as the main component. In addition, the coatings contained approximately 5–6 wt.% carbon, 1–2 wt.% oxygen, some amount of copper originating from the substrate, and trace amounts of chlorine derived from the choline chloride present in the electrolyte. The detected carbon is also attributed to the organic components of the Ethaline-based electrolyte. Importantly, no significant influence of the deposition parameters on the elemental composition of the coating surfaces was observed.

An efficient strategy to modify the surface composition of Ni coatings for improved HER catalysis is the incorporation of nanoparticles of transition metal sulfides, phosphides, or nitrides during electrodeposition, resulting in composite coatings with a nickel matrix. In the present work, MoS_2 nanoparticles were selected as the catalytic additive due to their well-known high activity toward HER.

MoS_2 acts as an efficient HER catalyst because its edge sites possess a favorable Gibbs free energy for hydrogen adsorption ($\Delta G_H \approx 0$), enabling efficient proton reduction and hydrogen desorption. In contrast, the basal planes are relatively inert, but their activity can be enhanced by structural defects, doping, or interaction with conductive supports such as metallic Ni. When dispersed within a Ni matrix, MoS_2 provides numerous catalytically active edge sites and improves electron transfer pathways, thereby synergistically enhancing the overall HER performance of the composite coating.

3.3 Preparation of a colloidal Ethaline-based electrolyte for the electrodeposition of MoS_2-containing Ni composites

The preparation of a colloidal electrolyte for MoS_2/Ni composite coating electrodeposition can be realized using three possible strategies.

The first approach involves the *in-situ* synthesis of MoS_2 nanoparticles directly within the electrolyte used for Ni electrodeposition. This method ensures a high degree of dispersion and intimate interaction between MoS_2 and the electrolyte components, which may improve particle incorporation and adhesion to the Ni matrix. However, controlling the size, stoichiometry, and stability of the in situ–formed nanoparticles can be challenging, and side reactions may alter the electrolyte composition or affect the nickel deposition process.

The second approach is to synthesize MoS_2 nanoparticles separately in an Ethaline medium, followed by isolation, purification, and re-dispersion into the Ni electrodeposition bath. This method allows better control over particle size, crystallinity, and surface chemistry before incorporation. Nevertheless, the additional synthesis and separation steps make this route more complex and time-consuming, and re-dispersion of MoS_2 particles without aggregation can be difficult.

The third and most practical approach is the use of commercially available MoS_2 nanopowders, which can be directly dispersed into the Ni electrolyte to form a colloidal suspension. This method is straightforward, reproducible, and suitable for scale-up. However, ensuring uniform and stable dispersion of the particles in the viscous Ethaline-based electrolyte may require optimization of surfactant concentration, stirring rate, or ultrasonic treatment to prevent sedimentation and agglomeration.

3.3.1 Synthesis of MoS_2 in Ethaline-based electrolytes

To prepare colloidal dispersions of MoS_2 nanoparticles for Ni–MoS_2 composite electrodeposition, several synthesis routes were explored using an Ethaline-based deep eutectic solvent (DES) as the reaction medium. The syntheses were conducted according to different precursor concentrations, reducing agent ratios, and solvent compositions, as summarized in samples MOS-1 to MOS-10.

In all experiments, ammonium tetrathiomolybdate ($(NH_4)_2MoS_4$) served as the molybdenum precursor, while L-ascorbic acid acted as a mild reducing agent promoting the conversion of Mo(VI) to Mo(IV) and subsequent formation of MoS_2. Ethaline (a 1:2 molar mixture of choline chloride and ethylene glycol) was used either in its pure form or in combination with deionized water to form a mixed solvent system (DES:H_2O = 3:1, v/v). The reaction temperature was maintained at 65 °C, providing sufficient thermal energy to drive reduction and sulfide formation under mild conditions.

The general procedure involved dissolving a weighed amount of $(NH_4)_2MoS_4$ in 40 mL of DES (or in 30 mL DES + 10 mL water for mixed systems). The solution was stirred for 1 hour at 65 °C until complete dissolution of the precursor. Subsequently, the required amount of L-ascorbic acid was added under continuous stirring. The reaction mixture was then maintained at 65 °C for an additional 2 hours,

during which the color of the solution gradually changed from orange-red to dark brown or black, indicating the formation of colloidal MoS_2.

Different synthesis routes (MOS-1 – MOS-10) varied in the precursor concentration, L-ascorbic acid amount, and solvent composition, as outlined below:

- ***Effect of Reducing Agent Amount***:

In MOS-1 and MOS-2 (using 3.124 mmol of $(NH_4)_2MoS_4$ in 40 mL DES), the L-ascorbic acid amount was varied from equimolar (3.124 mmol) to double molar ratio (6.248 mmol). Similarly, in MOS-5 and MOS-6 (lower precursor concentration, same solvent), and MOS-3/MOS-4 (DES–water mixture), the same molar ratios were applied. A higher L-ascorbic acid amount resulted in a faster color change and denser colloid formation, indicating more efficient reduction and nucleation of MoS_2 particles.

- ***Effect of Solvent Composition:***

In samples MOS-3, MOS-4, MOS-7, and MOS-8, partial replacement of DES with water reduced the viscosity of the medium, improving mass transport and promoting more uniform particle formation. However, excessive water content may affect DES stability and particle dispersion.

- ***Effect of Precursor Concentration:***

Higher precursor concentration (MOS-1, MOS-2, MOS-7, MOS-8) led to more concentrated colloidal dispersions with stronger coloration, while lower concentrations (MOS-3 – MOS-6, MOS-9, MOS-10) produced lighter suspensions with potentially smaller and more dispersed particles.

In all cases, visual observation of the color change confirmed successful reduction and formation of MoS_2 nanoparticles within the Ethaline-based medium.

The obtained MoS_2-containing extracts were used as additive components for preparing composite electrolytes for Ni–MoS_2 electrodeposition. A base Ethaline-based nickel electrolyte was first prepared by dissolving the required amounts of nickel(II) chloride hexahydrate ($NiCl_2 \cdot 6H_2O$) as the Ni source and boric acid (H_3BO_3) as the buffering agent in Ethaline, followed by the addition of a small, controlled amount of deionized water to adjust conductivity and viscosity.

The MoS_2-containing extracts obtained from synthesis steps indicated above were then thoroughly mixed with this base Ni electrolyte to achieve the final electrolyte compositions specified in Table 1, additionally containing MoS_2 particles in a concentration of 5 $g \cdot L^{-1}$. The prepared mixtures were continuously stirred and ultrasonicated to ensure uniform dispersion of the MoS_2 nanoparticles and to prevent sedimentation before electrodeposition.

These prepared composite electrolytes were subsequently utilized for the electrodeposition of Ni–MoS_2 composite coatings, enabling the incorporation of catalytically active MoS_2 particles into the Ni matrix to enhance hydrogen evolution reaction performance.

3.3.2 Synthesis, isolation, and re-dispersion of MoS_2 nanoparticles in Ethaline-based electrolyte for Ni/MoS_2 composite electrodeposition

An alternative approach for preparing Ni–MoS_2 composite electrolytes involves the separate synthesis of MoS_2 nanoparticles in an Ethaline-based medium, followed by their isolation, purification, and re-dispersion into the Ni electrodeposition bath. This route allows for precise control over the structural and chemical properties of MoS_2 before its incorporation into the Ni matrix.

Synthesis of MoS_2 Nanoparticles in Ethaline:

The synthesis can be carried out using ammonium tetrathiomolybdate ($(NH_4)_2MoS_4$) as the Mo precursor and L-ascorbic acid as a mild reducing agent.

Typically, a known amount of $(NH_4)_2MoS_4$ is dissolved in Ethaline under magnetic stirring at 65–80 °C until complete dissolution. Subsequently, L-ascorbic acid is added in equimolar or slightly excess ratio relative to the precursor to initiate the reduction of Mo(VI) to Mo(IV) and the formation of MoS_2 nanoparticles according to the reaction:

$$(NH_4)_2MoS_4 + \text{reducing agent} \rightarrow MoS_2 + S + \text{byproducts}.$$

The reaction mixture is maintained under stirring for several hours until the color changes from orange-red to dark brown or black, indicating MoS_2 formation. The resulting colloidal suspension typically contains uniformly distributed MoS_2 nanoparticles stabilized by weak interactions with the Ethaline components (choline chloride and ethylene glycol).

Isolation and Purification:

After synthesis, the MoS_2 nanoparticles are separated from the reaction medium by centrifugation (e.g., 8000–10,000 rpm for 10–15 min). The solid product is then washed several times with ethanol and deionized water to remove unreacted precursors, organic residues, and excess Ethaline components. Finally, the purified MoS_2 powder is dried under vacuum or mild heating (50–60 °C) until constant weight is achieved.

This step yields a clean MoS_2 nanopowder with minimal surface contamination, suitable for re-dispersion in electroplating baths.

Re-Dispersion into Ni Electrodeposition Bath:

The purified MoS_2 nanoparticles are re-dispersed in the Ethaline-based Ni electrolyte, which contains nickel(II) chloride hexahydrate ($NiCl_2 \cdot 6H_2O$) as the metal source and boric acid (H_3BO_3) as a buffer component. To achieve a uniform dispersion and prevent agglomeration, the MoS_2 powder is first ultrasonicated in a small amount of Ethaline or water–Ethaline mixture for 30–60 minutes. The

resulting suspension is then added to the Ni electrolyte under continuous stirring to obtain the final composite bath with a MoS_2 concentration of approximately 5 $g \cdot L^{-1}$ (other components as specified in Table 1).

Proper dispersion of MoS_2 is critical to ensure homogeneous incorporation of nanoparticles into the Ni matrix during electrodeposition. Ultrasonic agitation and mechanical stirring before deposition help maintain colloidal stability.

Advantages and Considerations:

This synthesis route offers several advantages, including precise control over particle size, crystallinity, and purity, as well as the possibility to modify surface chemistry through post-synthesis treatments. However, it is more labor-intensive and involves additional steps such as separation, washing, and re-dispersion. Moreover, care must be taken to maintain particle stability and prevent aggregation upon introduction into the viscous Ethaline-based Ni electrolyte.

Thus, this proposed method provides a versatile and tunable pathway for producing well-defined MoS_2 nanoparticles suitable for controlled incorporation into Ni composite coatings for enhanced HER catalytic performance.

3.3.3 Preparation of Ni–MoS_2 containing electrolyte using commercial MoS_2 powder

To prepare the electrolyte for Ni–MoS_2 composite electrodeposition, commercial MoS_2 nanopowder (Japan origin, average particle size ≈ 90 nm) was utilized as the source of catalytic nanoparticles. This approach allows for straightforward preparation, good reproducibility, and controlled addition of MoS_2 into the Ni electrolyte without requiring *in-situ* synthesis or chemical reduction steps.

Electrolyte Composition and Preparation Procedure:

A total of 200 ml of composite electrolyte was prepared with the composition presented in table 3.

Table 3. Formulation and component concentrations of the Ni–MoS_2 composite electrolyte.

Component	Content
$NiCl_2 \cdot 6H_2O$	1.0 M
H_3BO_3 (Boric acid)	0.13 M
Additional water	30 wt.%
Ethaline (choline chloride + ethylene glycol, 1:2 molar ratio)	balance
MoS_2 nanopowder	1 g L^{-1}

The preparation was carried out as follows:

1. **Base electrolyte preparation:** The required amounts of $NiCl_2 \cdot 6H_2O$ and boric acid were dissolved in a mixture of Ethaline and deionized water (30 wt.% water) under constant stirring at 60 °C until complete dissolution. This produced a homogeneous Ni-based plating solution with appropriate conductivity and buffering capacity.
2. **Addition of MoS_2 nanoparticles:** The commercial MoS_2 nanopowder was gradually added to the base electrolyte to achieve a final concentration of 1 g L^{-1}. To ensure uniform dispersion and to minimize particle agglomeration, the suspension was ultrasonicated for 30 minutes and subsequently stirred magnetically for an additional hour at 50–60 °C.
3. **Stabilization:** Before electrodeposition, the prepared composite electrolyte was kept under gentle stirring to maintain a stable colloidal suspension and uniform particle distribution.

The use of commercial MoS_2 nanoparticles simplifies the electrolyte preparation process, avoiding multiple synthesis or purification steps. The small particle size (≈ 90 nm) ensures a large active surface area and promotes uniform incorporation into the Ni matrix during electrodeposition. However, due to the relatively high viscosity of Ethaline and the hydrophobic nature of MoS_2, proper dispersion control via ultrasonication and continuous stirring is essential to prevent sedimentation and achieve reproducible coating morphology.

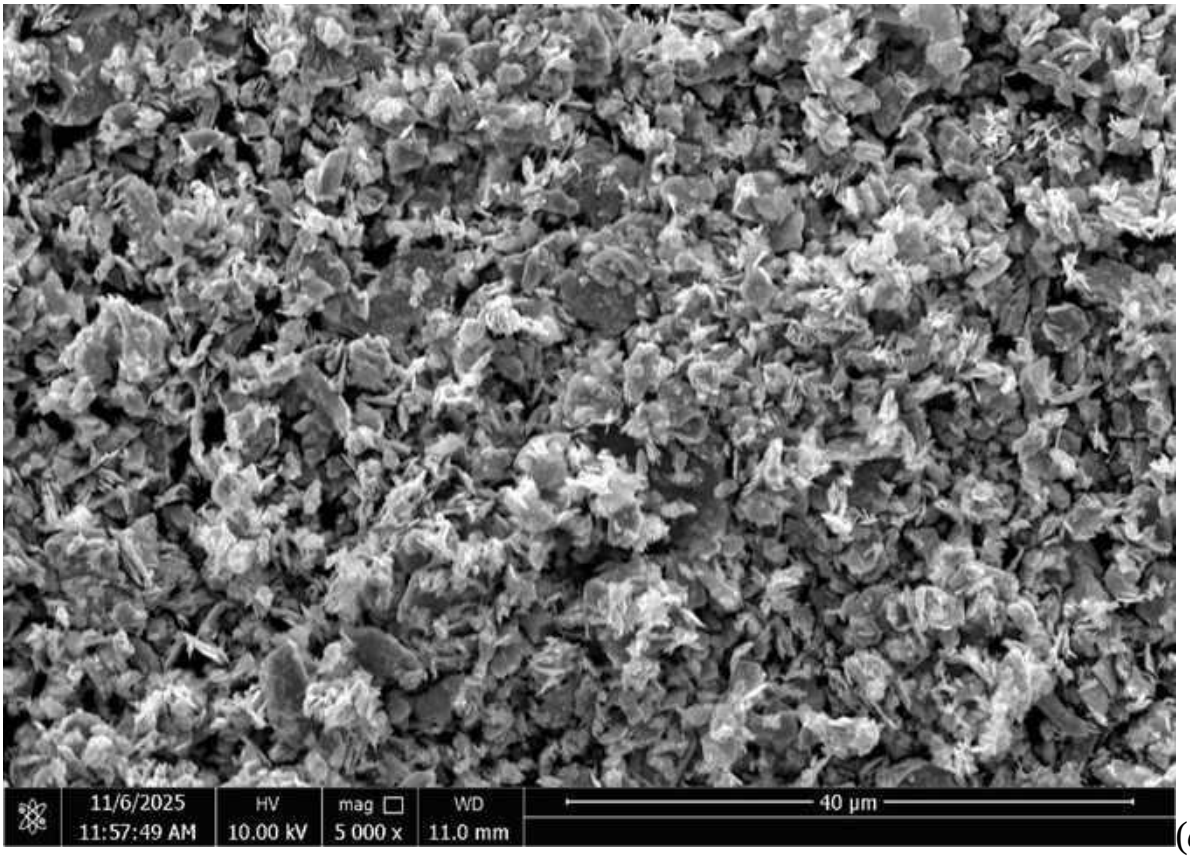
It should be noted that the resulting Ni–MoS_2 composite electrolyte was stable, homogeneous, and prepared for subsequent electrodeposition experiments aimed at creating catalytic coatings with improved HER activity.

3.4 Comparison of commercial and synthesized MoS_2 powders

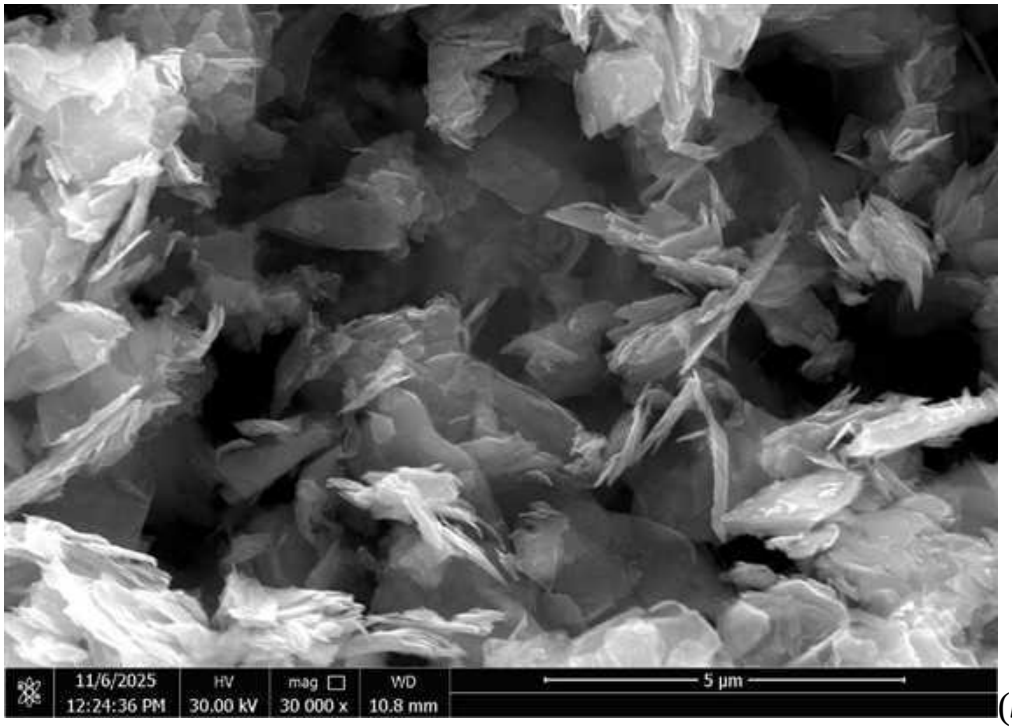
Before depositing Ni/MoS_2 composite coatings, it was necessary to compare the commercial MoS_2 powder with those synthesized in Ethaline. The chemical composition, crystallinity, and particle size and shape can significantly impact how MoS_2 particles are incorporated into the Ni matrix. Additionally, these factors may influence the growth characteristics of the Ni matrix itself. Therefore, the dried MoS_2 powders were analyzed using SEM and EDX. Figures 10 and 11 show the morphology, structure, and elemental composition of the examined powders.

SEM images of the commercial MoS_2 powder at different magnifications are shown in Fig. 10***a*** and 10***b***. The corresponding EDX spectrum is presented in Fig. 10***c***. The EDX analysis revealed the presence of small amounts of oxygen and carbon. The detected carbon signal most likely originated from the carbon tape used to mount the powder particles, rather than from the powder itself. The minor oxygen signal can be attributed to slight surface oxidation of MoS_2 or to adsorbed oxygen-containing species resulting from exposure to air.

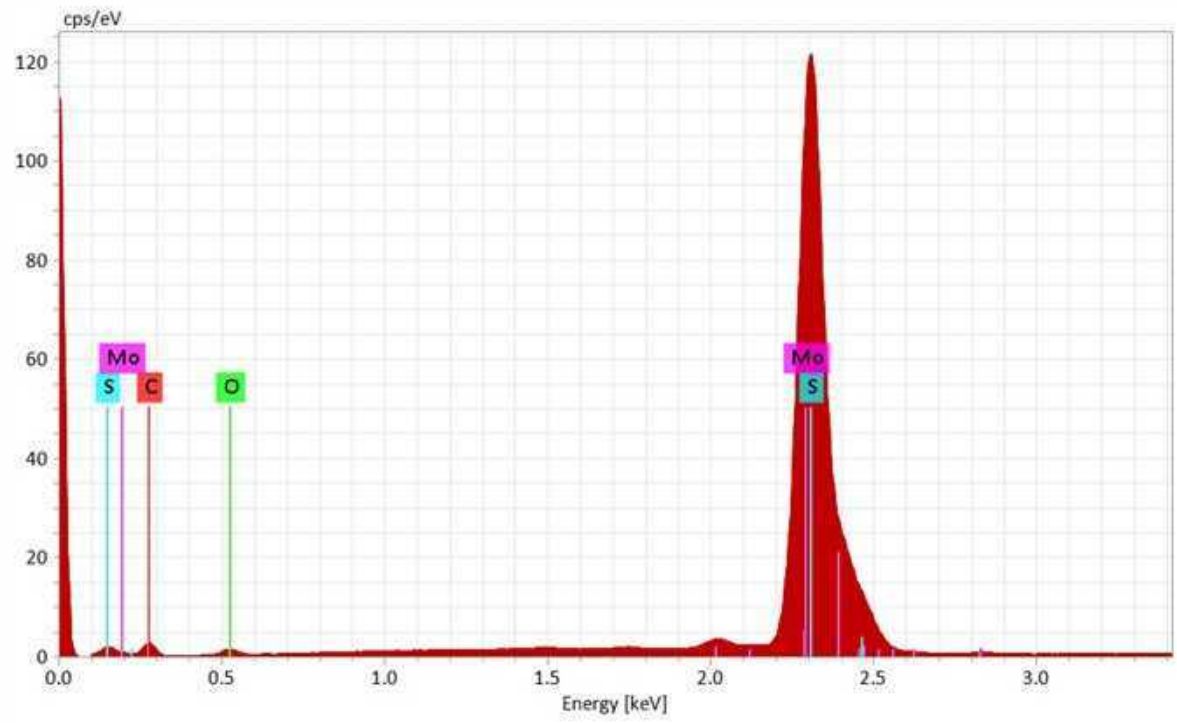
As shown in Fig. 11***a*** and 11***b***, the MoS_2 powder synthesized in Ethaline displays a morphology significantly different from that of the commercial MoS_2 powder. The data clearly indicate that the synthesized powder mainly consists of much smaller, nanosized particles. It is important to note that the elemental composition of the synthesized powder (Fig. 11***c***) is similar to that of the commercial product. The smaller nanosized particles of the synthesized MoS_2 powder have great potential as a catalytic component and may offer higher efficiency for HER compared with commercially available MoS_2 particles.



(***a***)

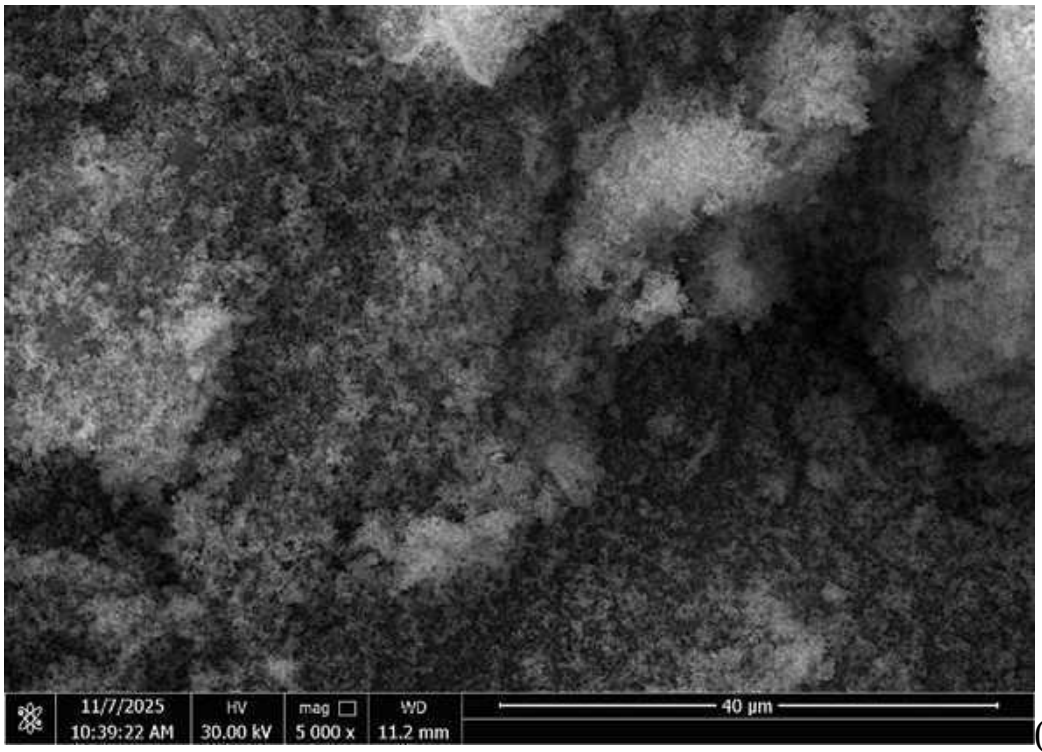


(***b***)

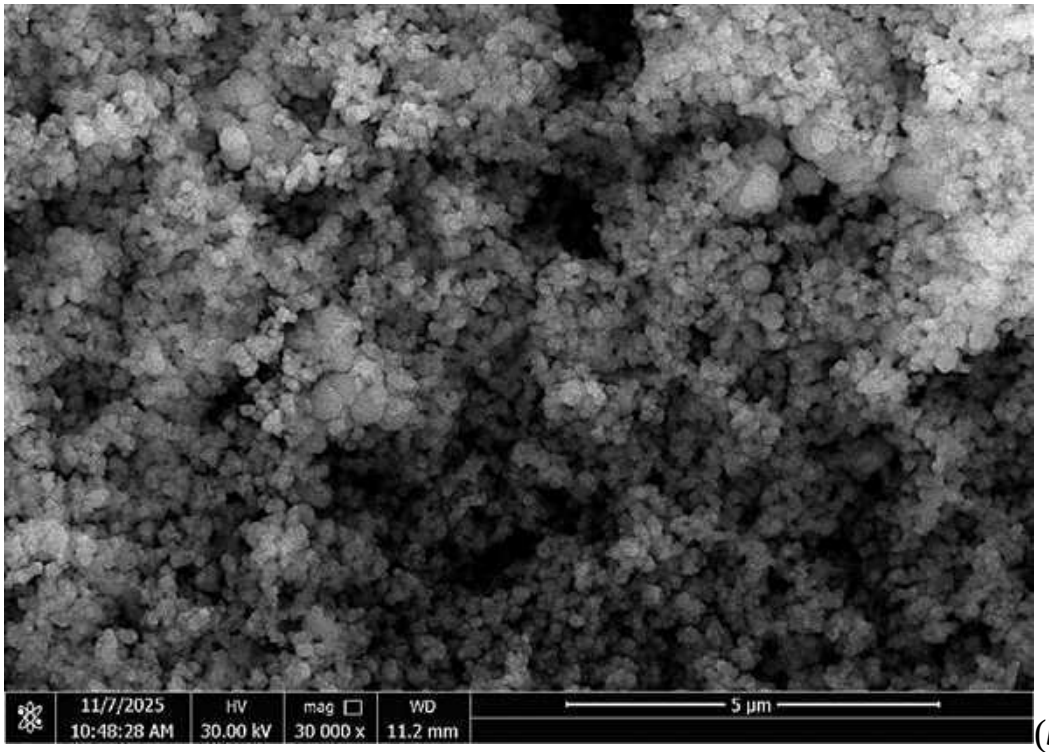


(***c***)

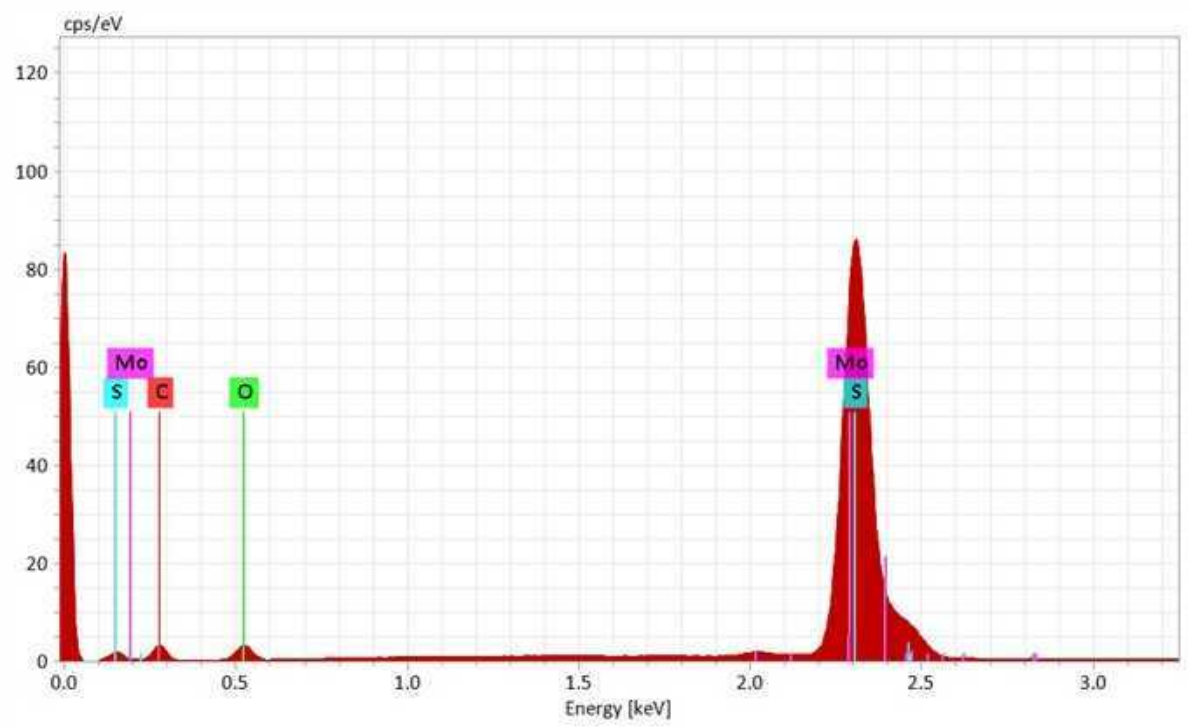
Fig. 10. SEM images (***a***, ***b***) and EDX spectrum (***c***) of the commercial MoS_2 powder. (***a***) Magnification: 5k, scale bar: 40 µm; (***b***) Magnification: 30k, scale bar: 5 µm.


11/7/2025
10:39:22 AM
HV
30.00 kV
mag
5 000 x
WD
11.2 mm
40 µm

(***a***)


11/7/2025
10:48:28 AM
HV
30.00 kV
mag
30 000 x
WD
11.2 mm
5 µm

(***b***)



(***c***)

Fig. 11. SEM images (***a***, ***b***) and EDX spectrum (***c***) of the synthesized in Ethaline MoS_2 powder. (***a***) Magnification: 5k, scale bar: 40 µm; (***b***) Magnification: 30k, scale bar: 5 µm.

3.5 Electrodeposition and characterization of Ni/MoS_2 composite coatings from the Ethaline-based electrolyte

The electrolyte composition used for the electrodeposition of Ni/MoS_2 composite coatings is presented in Table 3, while the electrodeposition conditions are summarized in Table 4.

Stationary i–E curves for Ni and Ni/MoS_2 electrodeposition from the Ethaline-based electrolyte were derived from the steady-state potentials measured during chronopotentiometric experiments and are shown in Figure 12. Figure 13 compares the deposition rates of Ni and Ni/MoS_2 coatings at different current densities. As seen, both datasets exhibit nearly identical behavior for Ni and Ni/MoS_2, indicating

that adding MoS_2 does not significantly affect the kinetics of the electrodeposition process.

Table 4. Electrodeposition conditions for Ni/MoS_2 composite coatings.

Sample	i, mA/cm^2	t, ^{o}C	τ, min
1	5	40	20
2	10		
3	15		
4	20		
5	25		

In light of this, it becomes particularly interesting to investigate whether the incorporation of MoS_2 influences the morphological features of the resulting coatings. Therefore, a detailed SEM analysis was carried out to examine the surface morphology.

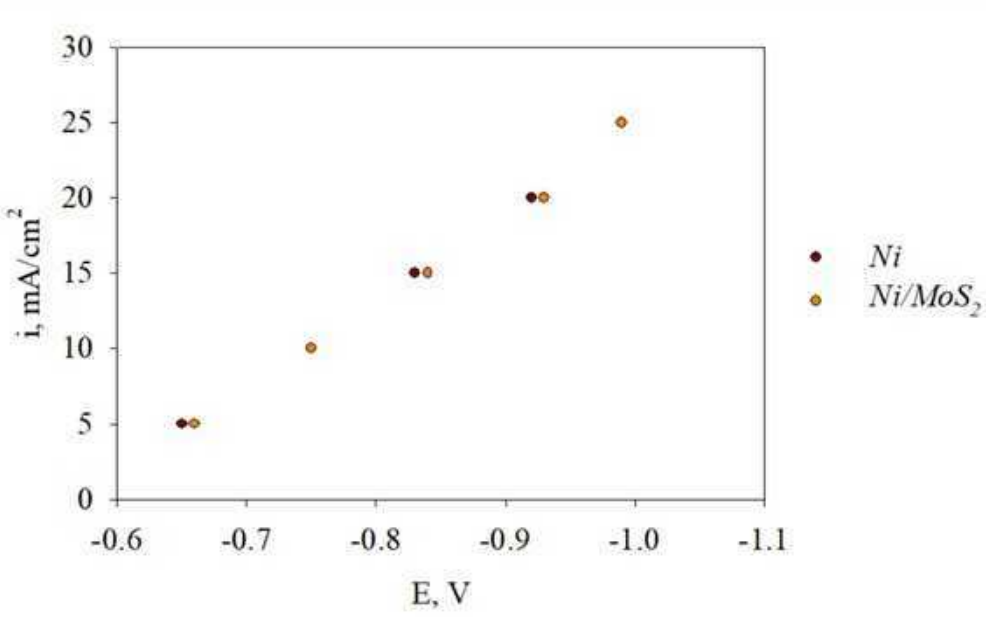


Fig. 12. Stationary i-E curves of Ni and Ni/MoS_2 electrodeposition from an Ethaline-based electrolyte constructed from steady-state potentials obtained during chronopotentiometric measurements (t = 40 ^{o}C).

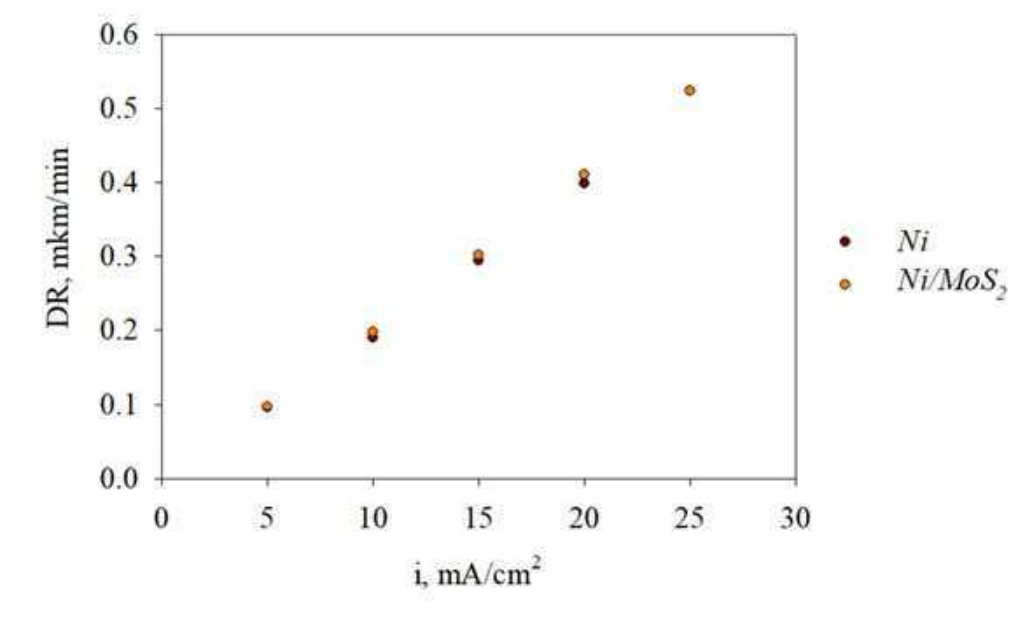
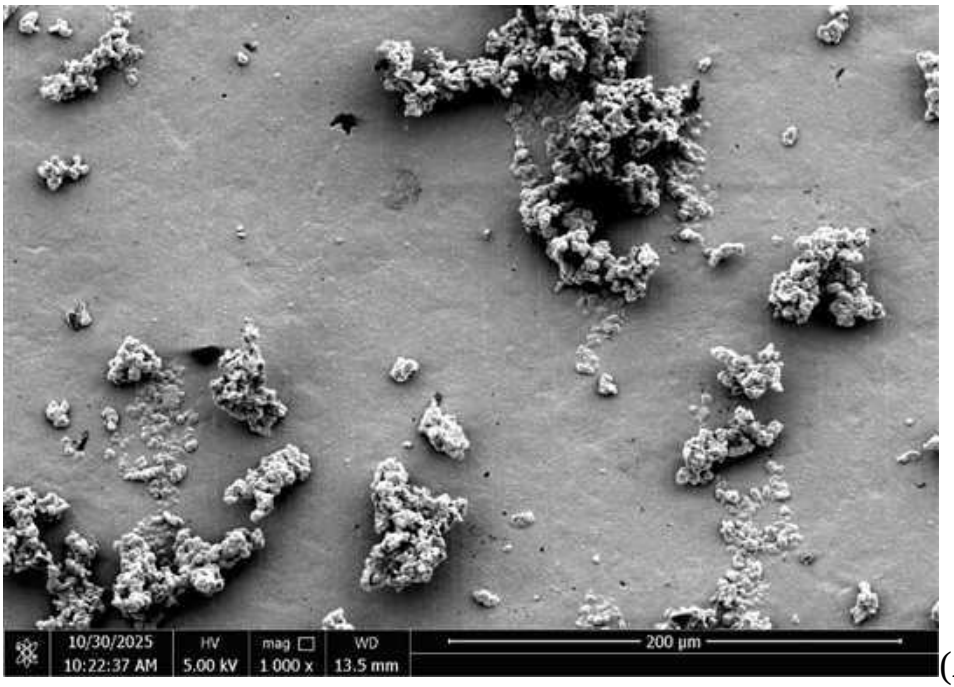
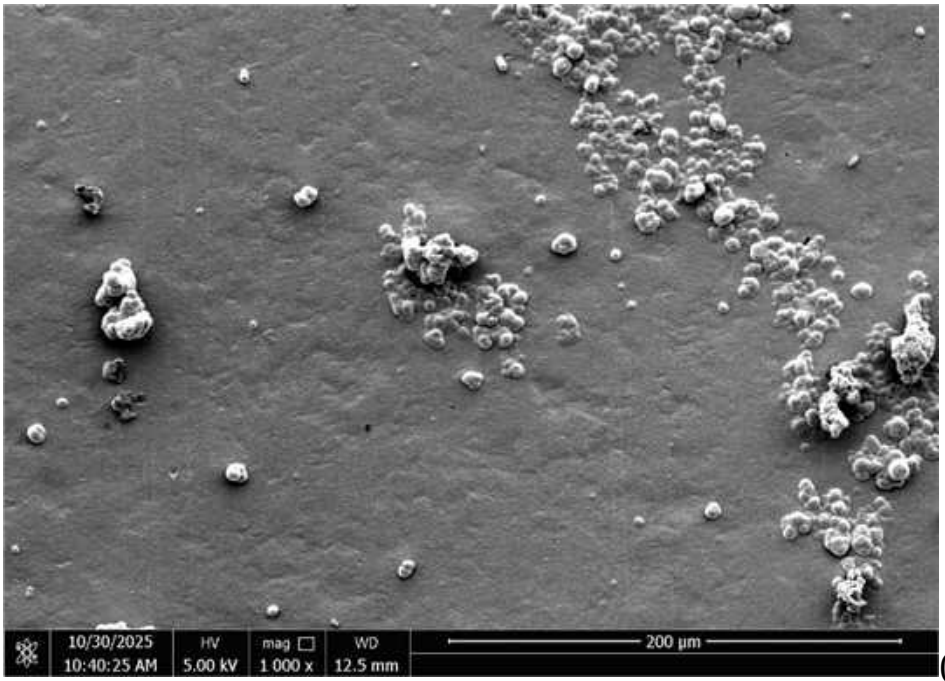


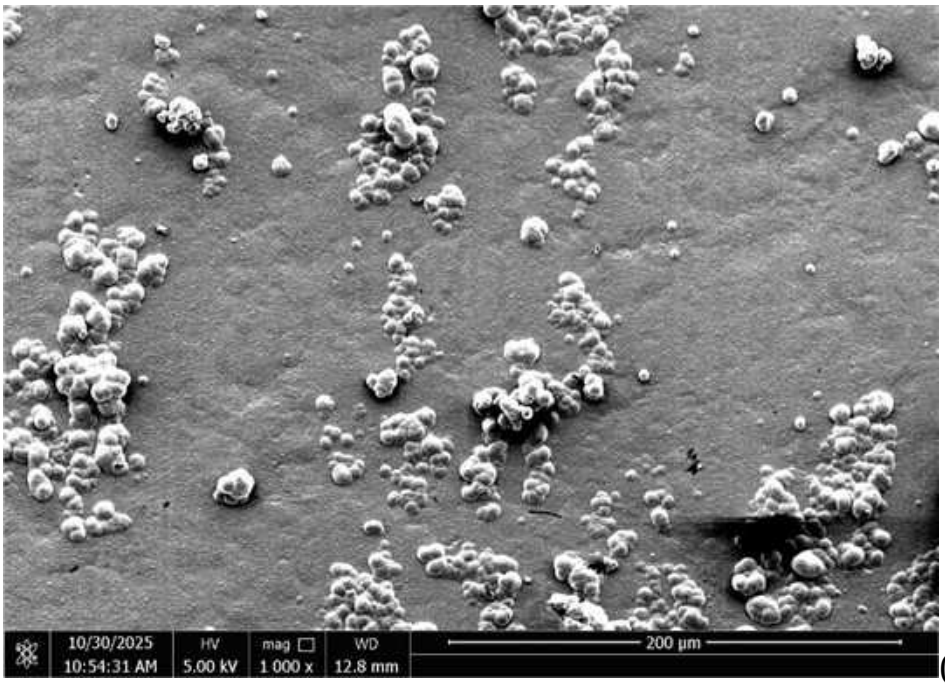
Fig. 13. Influence of deposition current density on deposition rate of Ni and Ni/MoS_2 coatings in Ethaline-based electrolyte (t = 40 °C).

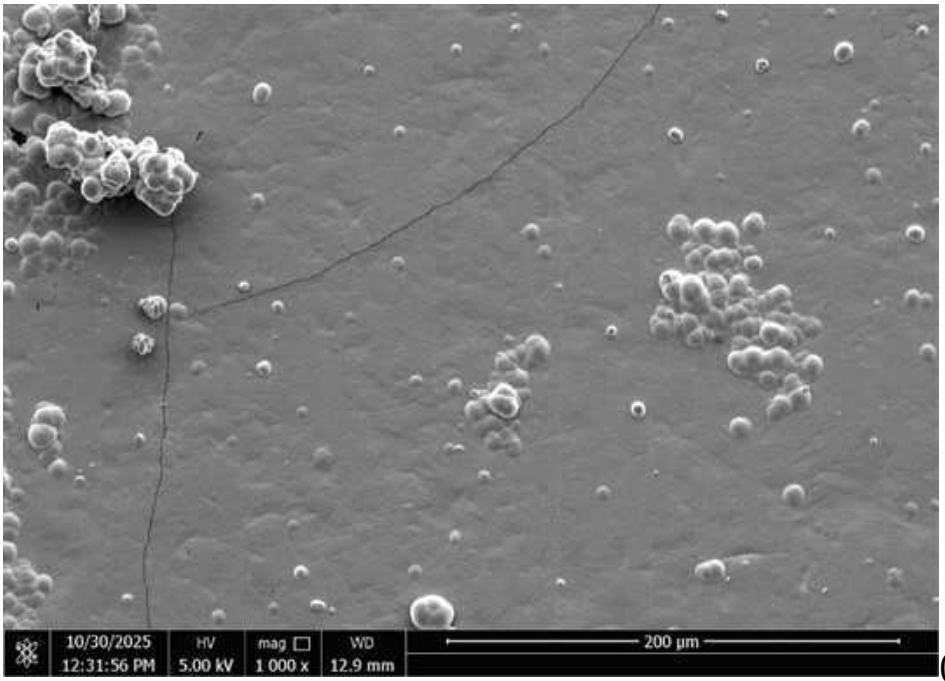
SEM images of samples (***1***) – (***5***) are presented in Figs. 14-16 that represent surfaces under different magnifications.



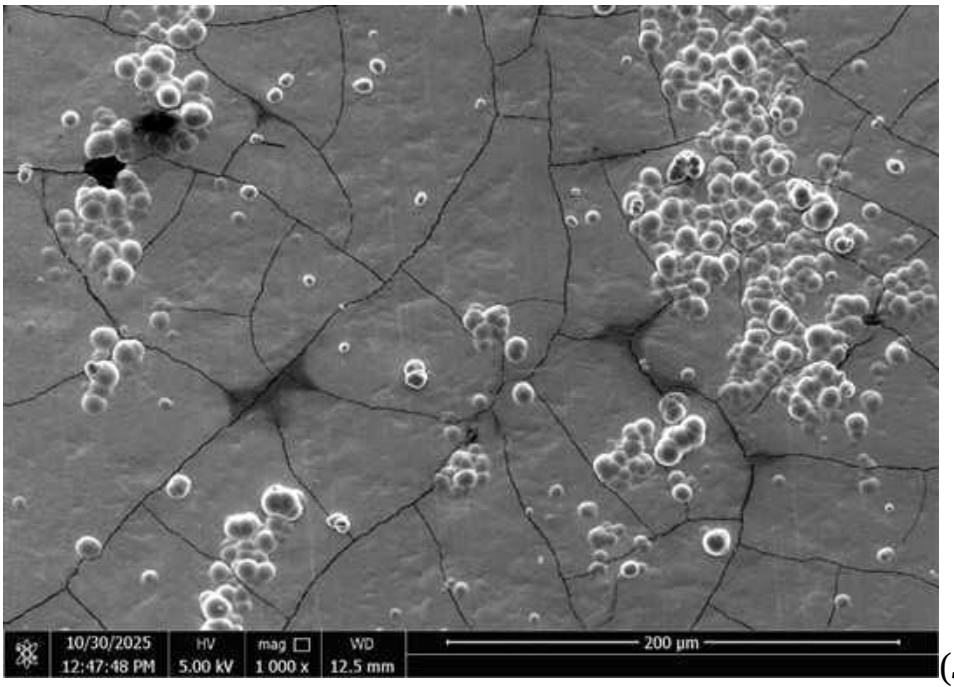
(***1***)


10/30/2025
10:40:25 AM
HV
5.00 kV
mag
1 000 x
WD
12.5 mm
200 µm
(*2*)


10/30/2025
10:54:31 AM
HV
5.00 kV
mag
1 000 x
WD
12.8 mm
200 µm
(*3*)

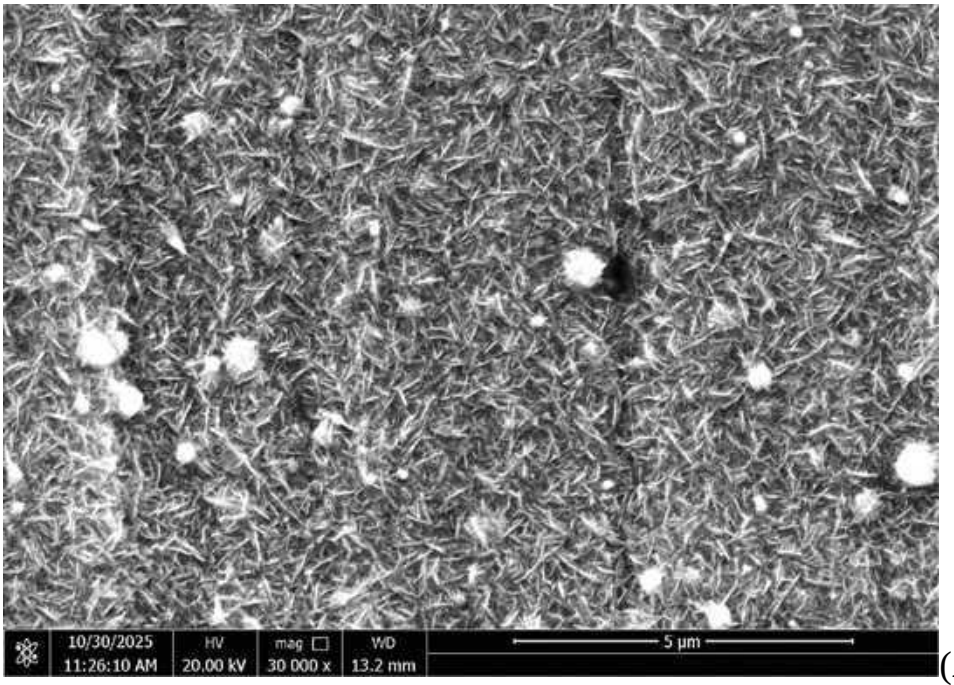


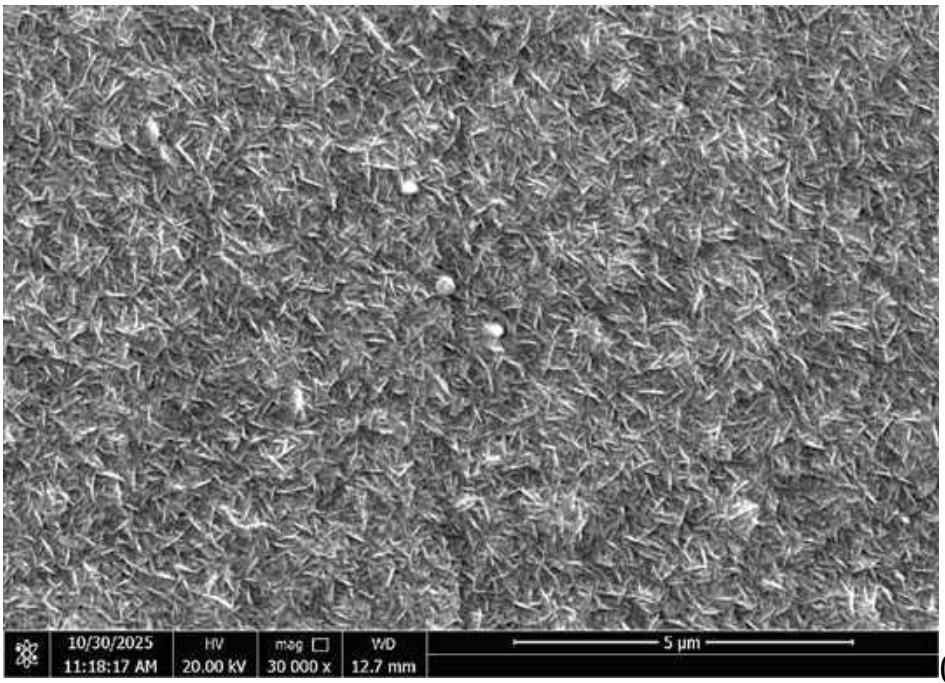
(*4*)

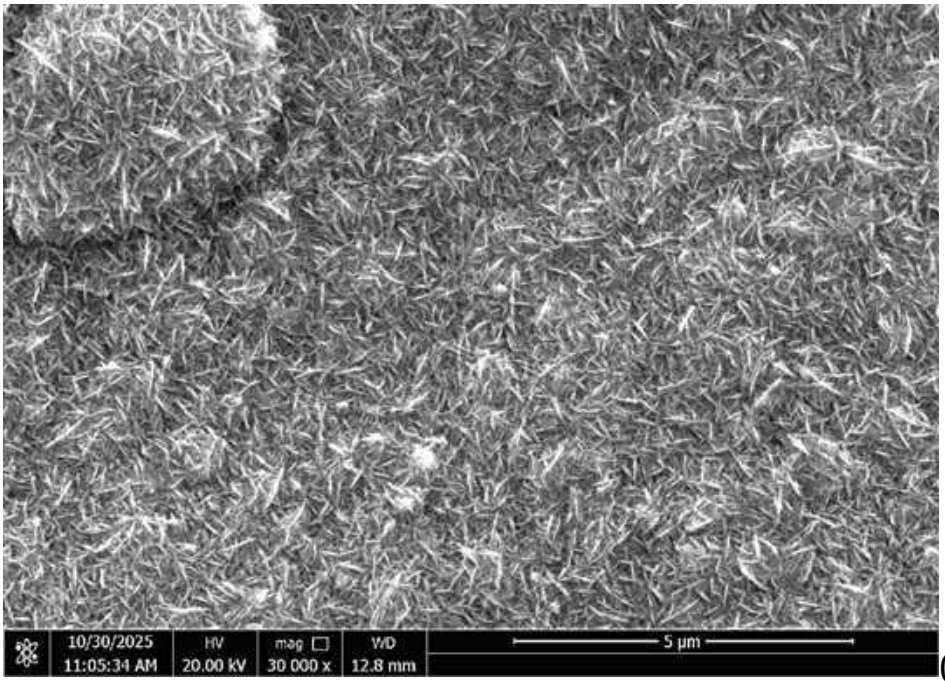


(*5*)

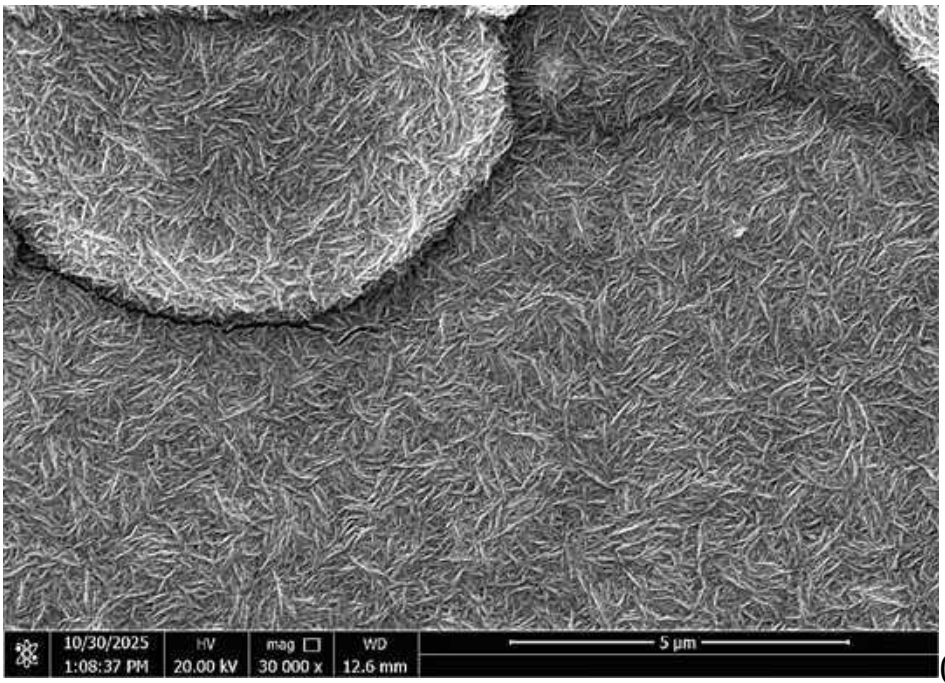
Fig. 14. SEM images of Ni/MoS_2 coatings electrodeposited from the Ethaline-based electrolyte at 40 °C for 20 min under different current densities. Magnification: 1k×; scale bar: 200 µm. Sample numbers correspond to the electrodeposition parameters listed in Table 4.


10/30/2025
11:26:10 AM
HV
20.00 kV
mag
30 000 x
WD
13.2 mm
5 µm
(*1*)

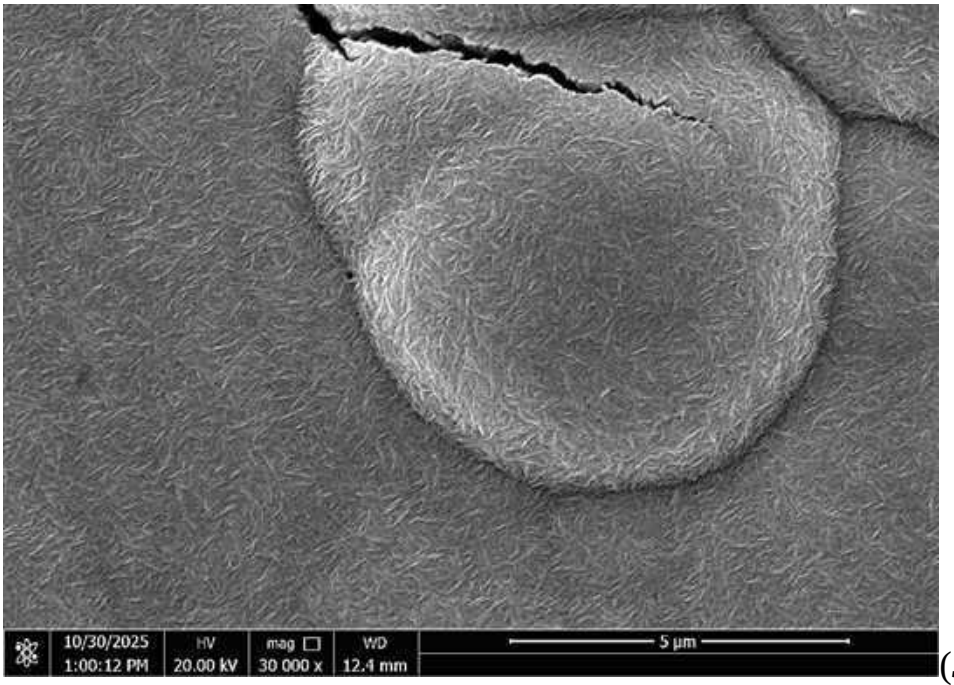

10/30/2025
11:18:17 AM
HV
20.00 kV
mag
30 000 x
WD
12.7 mm
5 µm
(*2*)


10/30/2025
11:05:34 AM
HV
20.00 kV
mag
30 000 x
WD
12.8 mm
5 µm

(*3*)

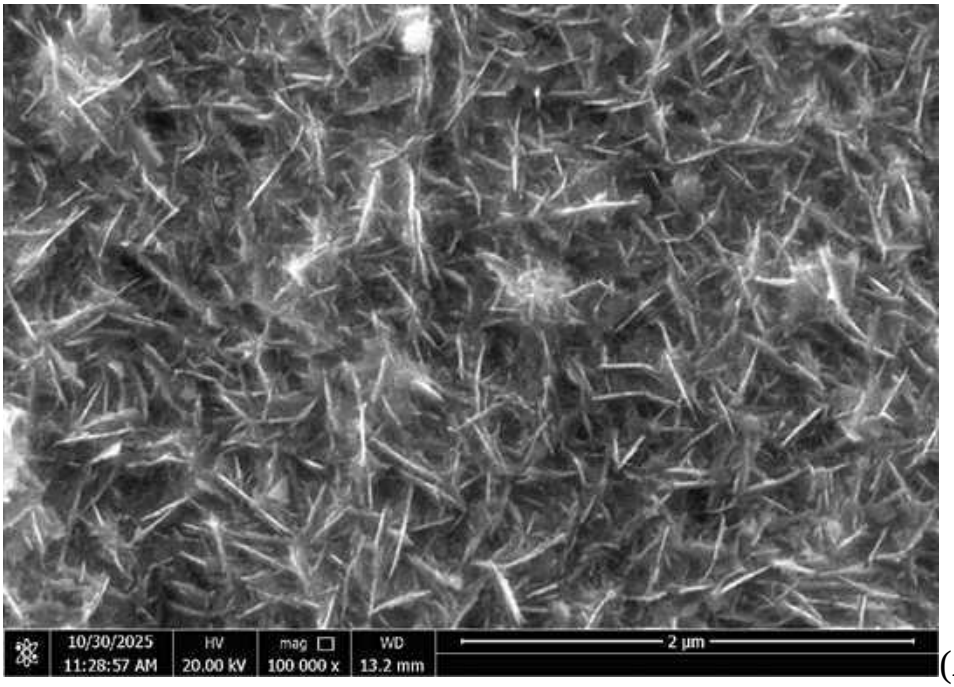

10/30/2025
1:08:37 PM
HV
20.00 kV
mag
30 000 x
WD
12.6 mm
5 µm

(*4*)

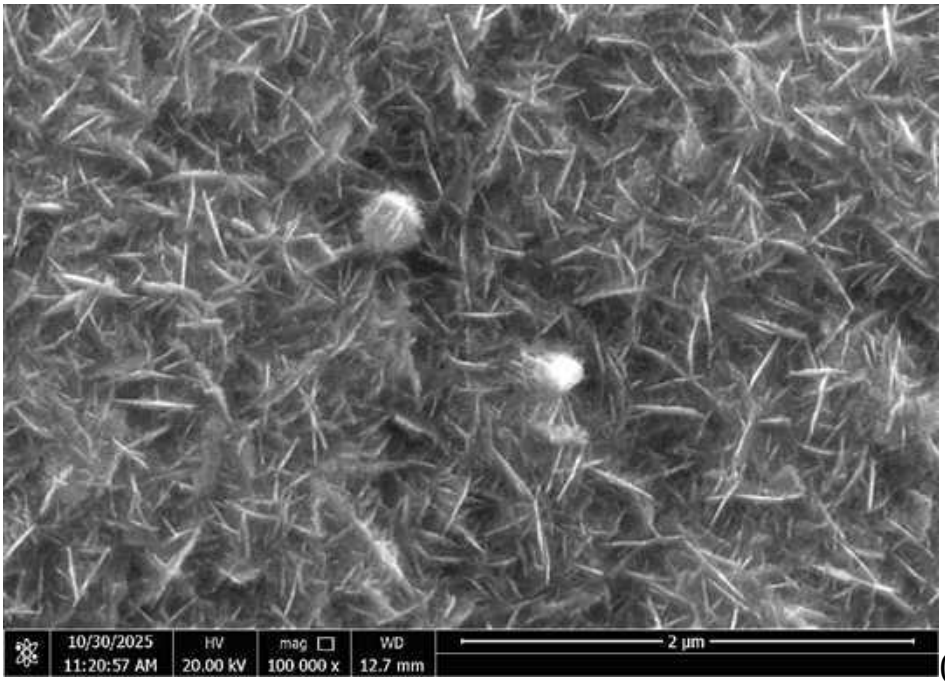


(***5***)

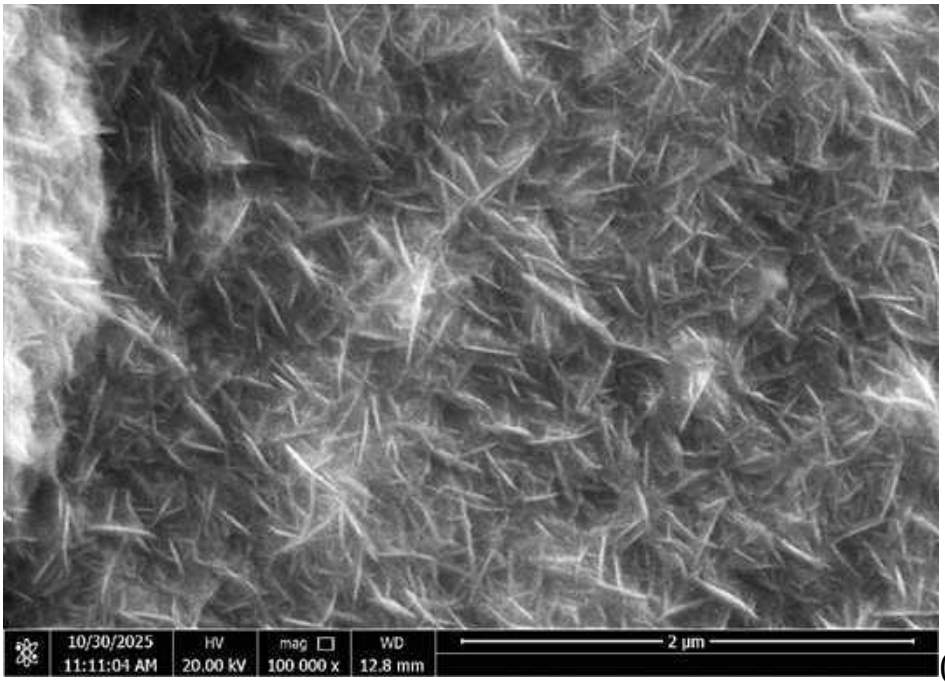
Fig. 15. SEM images of Ni/MoS_2 coatings electrodeposited from the Ethaline-based electrolyte at 40 °C for 20 min under different current densities. Magnification: 30k×; scale bar: 5 µm. Sample numbers correspond to the electrodeposition parameters listed in Table 4.



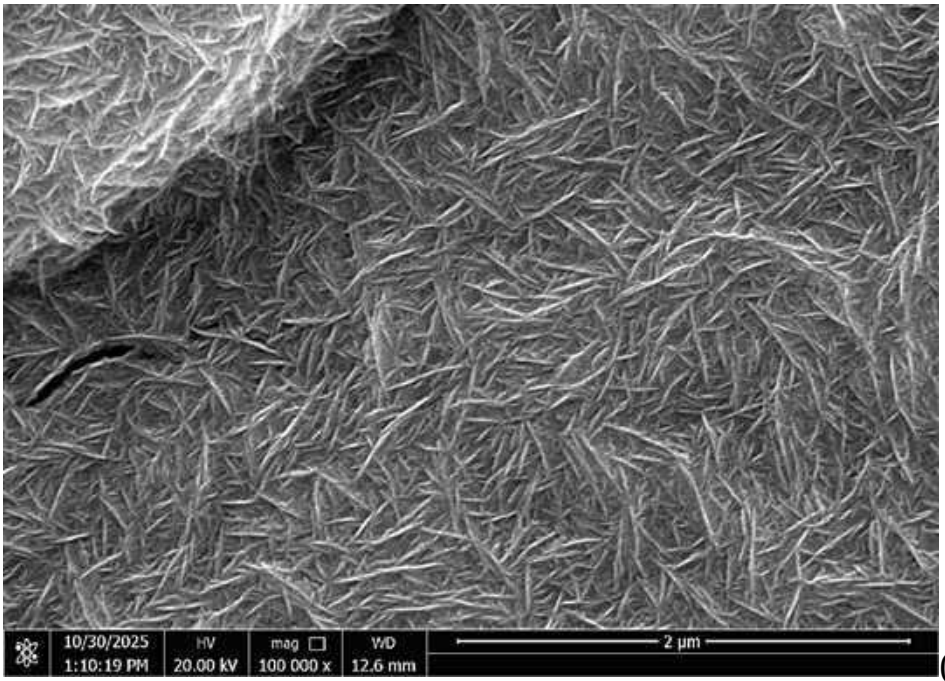
(***1***)


10/30/2025
11:20:57 AM
HV
20.00 kV
mag
100 000 x
WD
12.7 mm
2 µm

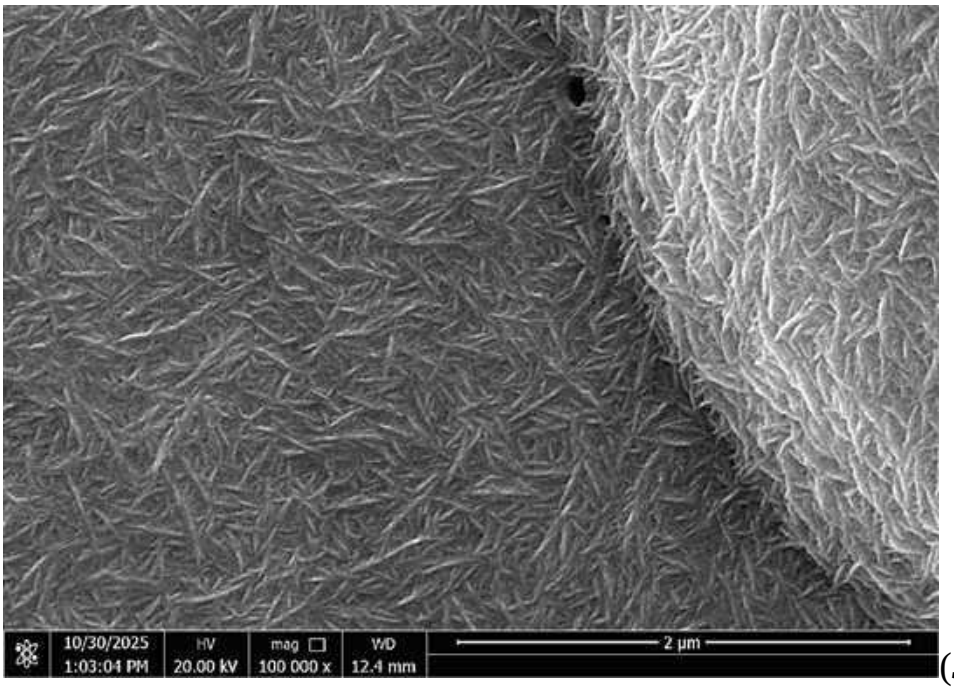
(*2*)


10/30/2025
11:11:04 AM
HV
20.00 kV
mag
100 000 x
WD
12.8 mm
2 µm

(*3*)



(*4*)



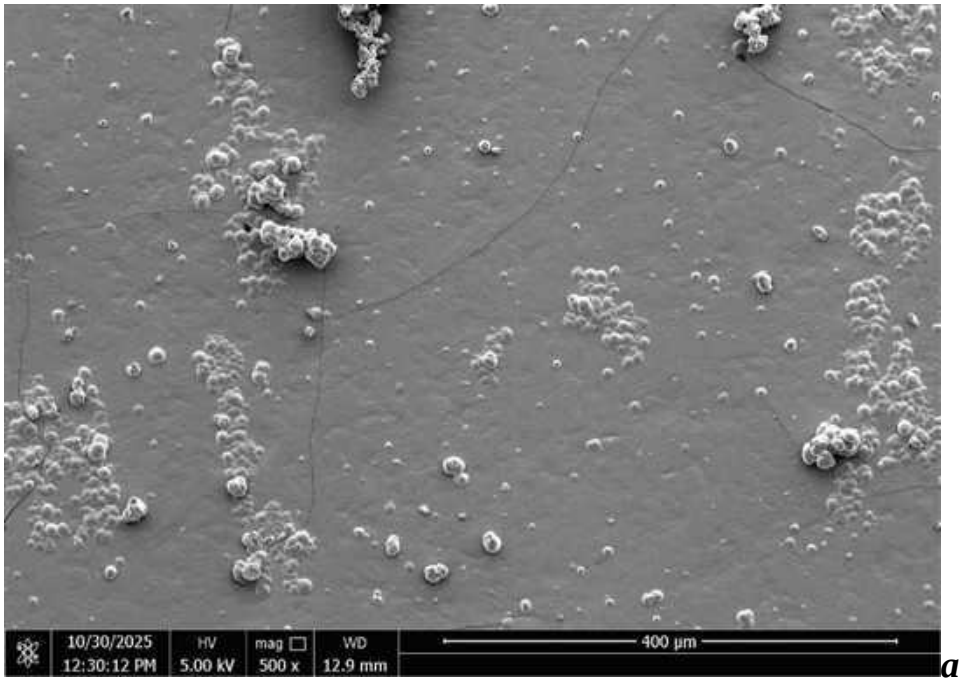
(*5*)

Fig. 16. SEM images of Ni/MoS_2 coatings electrodeposited from the Ethaline-based electrolyte at 40 °C for 20 min under different current densities. Magnification: 100k×; scale bar: 2 µm. Sample numbers correspond to the electrodeposition parameters listed in Table 4.

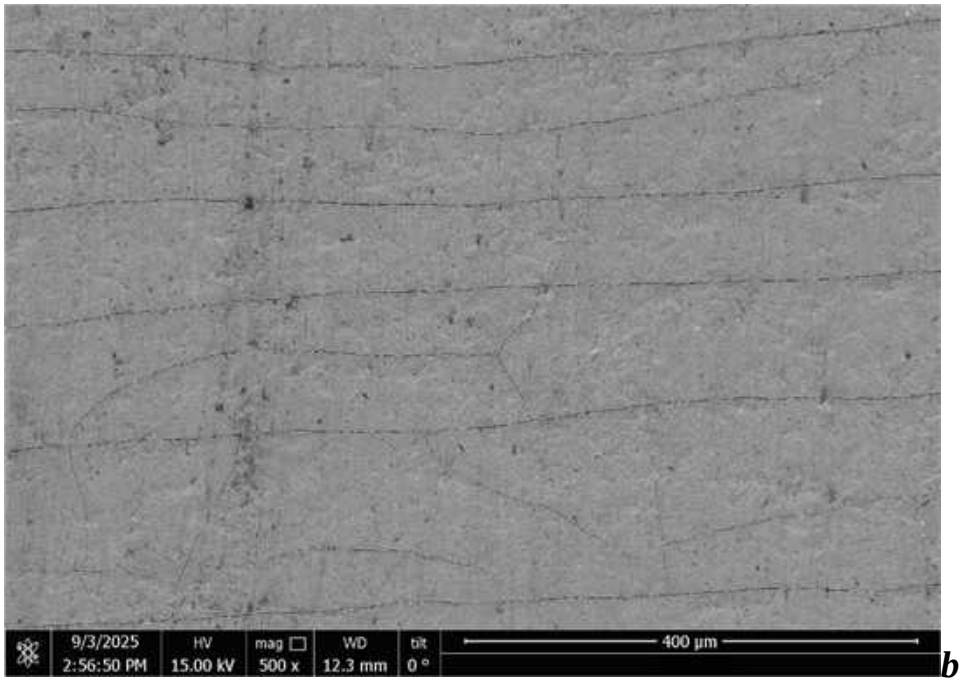
As shown in Fig. 14, which presents the coating surfaces at the lowest magnification, Ni/MoS_2 composite coatings electrodeposited at current densities of 20 mA cm^{-2} and higher exhibit cracks similar to those observed in pure Ni coatings, although their number and severity are reduced in the presence of MoS_2 particles. The formation of cracks at high current densities can be attributed to the accumulation of internal stresses during rapid deposition, while the incorporation of MoS_2 particles appears to mitigate these stresses, resulting in fewer cracks.

Admit that Ni/MoS_2 coating surfaces display islands of hemispherical features, with diameters that increase as the current density rises (Fig. 14). These hemispherical structures likely result from localized rapid Ni deposition around nucleation sites, where faster metal ion reduction at higher current densities favors the growth of larger deposits. The incorporation of MoS_2 particles may also influence this morphology by acting as preferential nucleation centers, locally modifying the deposition rate. As demonstrated in Fig. 17, such hemispherical features are absent in pure Ni coatings, confirming the role of MoS_2 particles in their formation.

Figures 15-16 reveal that the Ni/MoS_2 coatings exhibit the same lamellar structure as observed for pure Ni coatings. It is evident, however, that the Ni/MoS_2 coatings possess a more pronounced hierarchical architecture, combining micro- and nanoscale structural features. Such a combination may positively influence the catalytic properties of the MoS_2-containing coatings, not only due to changes in their chemical composition and related factors but also as a result of the observed morphological variations.



a

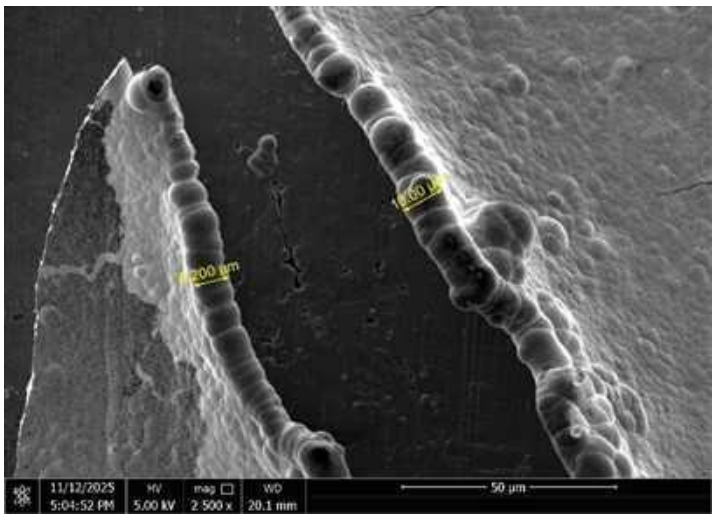


b

Fig. 17. SEM images of Ni/MoS_2 coating (a) and Ni (b) electrodeposited from the Ethaline-based electrolyte at 40 °C for 20 min under current density 20 mA cm^{-2}. Magnification: 500×; scale bar: 400 µm.

For Ni and Ni/MoS_2 coatings, it was observed that layers with a thickness of 7–12 μm, deposited at high current densities (≥20 mA cm^{-2}), tend to develop cracks due to the accumulation of internal stresses (Fig. 18). As previously discussed, the incorporation of MoS_2 slightly mitigates this effect, suggesting that a further increase in the MoS_2 content could reduce the tendency toward cracking by enhancing coating ductility and facilitating stress relaxation.

To further reduce internal stresses and prevent crack formation, several strategies can be implemented. Optimizing deposition parameters is especially crucial. For preparing thick Ni or Ni/MoS_2 coatings (>10 μm), applying lower current densities (<20 mA cm^{-2}) and extending the deposition time promotes more consistent growth and minimizes stress accumulation. Adding surfactants or stress-relief additives such as sodium dodecyl sulfate, saccharin, or polyethylene glycol to the electrolyte can also enhance coating uniformity and decrease internal stresses. Another effective technique involves using pulse or pulse-reverse electrodeposition, which improves ion transport and provides better control over the microstructure of the coating, thereby reducing residual stress. Lastly, moderate post-deposition annealing can further alleviate internal stresses without compromising the coating's mechanical integrity or surface quality.



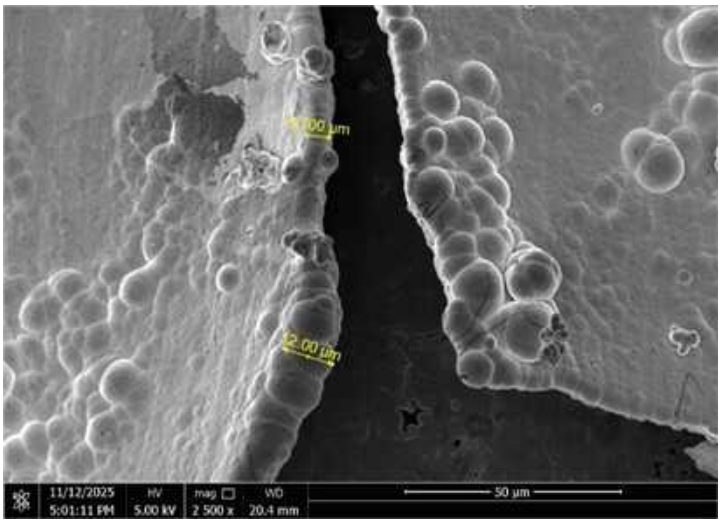


Fig. 18. SEM images of Ni/MoS_2 coating electrodeposited from the Ethaline-based electrolyte at 40 °C for 20 min under a current density of 20 mA cm^{-2}. Magnification: 2.5k×; scale bar: 50 µm.

Let us consider the distribution of MoS_2 on the surfaces of Ni/MoS_2 composite coatings obtained under different deposition conditions. As shown in Fig. 19, at low current densities, agglomerates of MoS_2 particles are observed on the surface of the electrodeposits (sample ***1*** is considered). When higher current densities are applied, the MoS_2 content increases substantially, and the particle distribution becomes homogeneous (Fig. 20). The results indicate that MoS_2 particles homogeneously cover the entire surface of sample ***5***.

The MoS_2 content and its surface distribution may play a crucial role in determining the catalytic performance of the coatings toward the HER. A higher MoS_2 load generally increases the number of exposed active edge sites, thereby enhancing catalytic activity. Moreover, a homogeneous distribution of MoS_2 particles ensures more uniform accessibility of these active sites and facilitates efficient charge transfer across the surface. In contrast, particle agglomeration at low current densities can reduce the effective catalytic area and hinder electron transport,

ultimately lowering HER efficiency. Thus, both the amount of incorporated MoS_2 and the uniformity of its dispersion are key factors governing the overall electrocatalytic behavior.

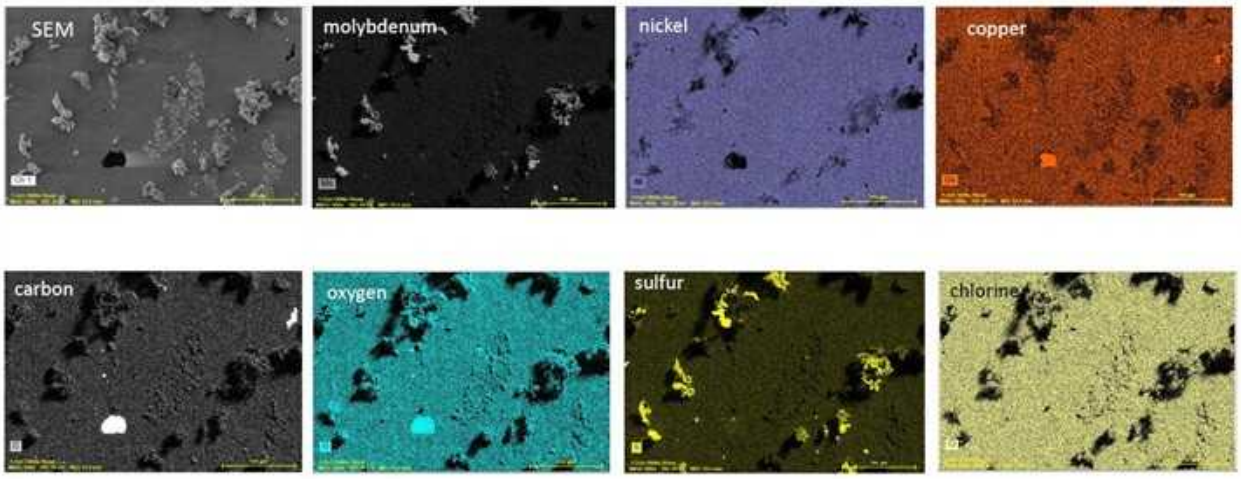


Fig. 19. EDX elemental maps acquired from sample (***1***). Magnification: 1k×; scale bar: 100 µm. A sample number corresponds to the electrodeposition parameters listed in Table 4.

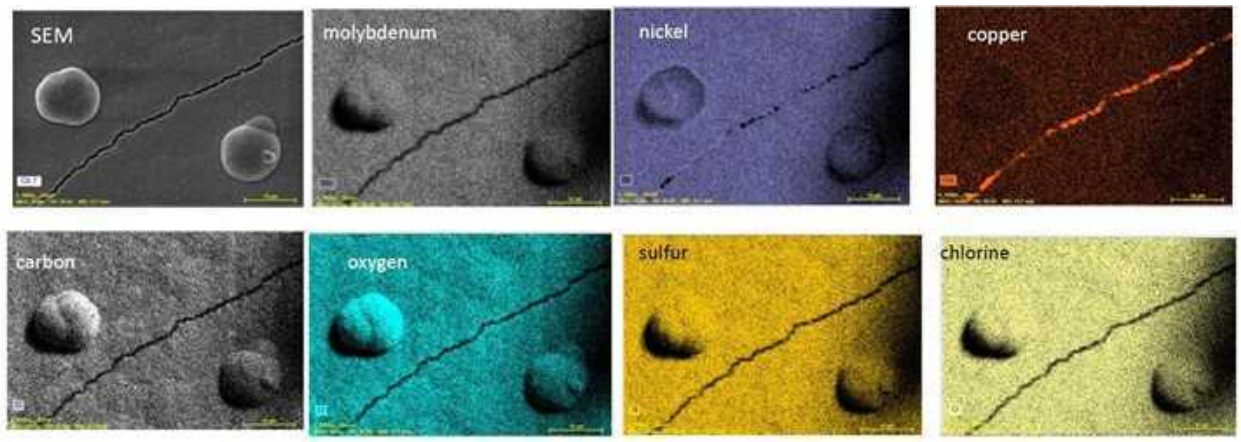


Fig. 20. EDX elemental maps acquired from sample (***5***). Magnification: 3.5k×; scale bar: 10 µm. A sample number corresponds to the electrodeposition parameters listed in Table 4.

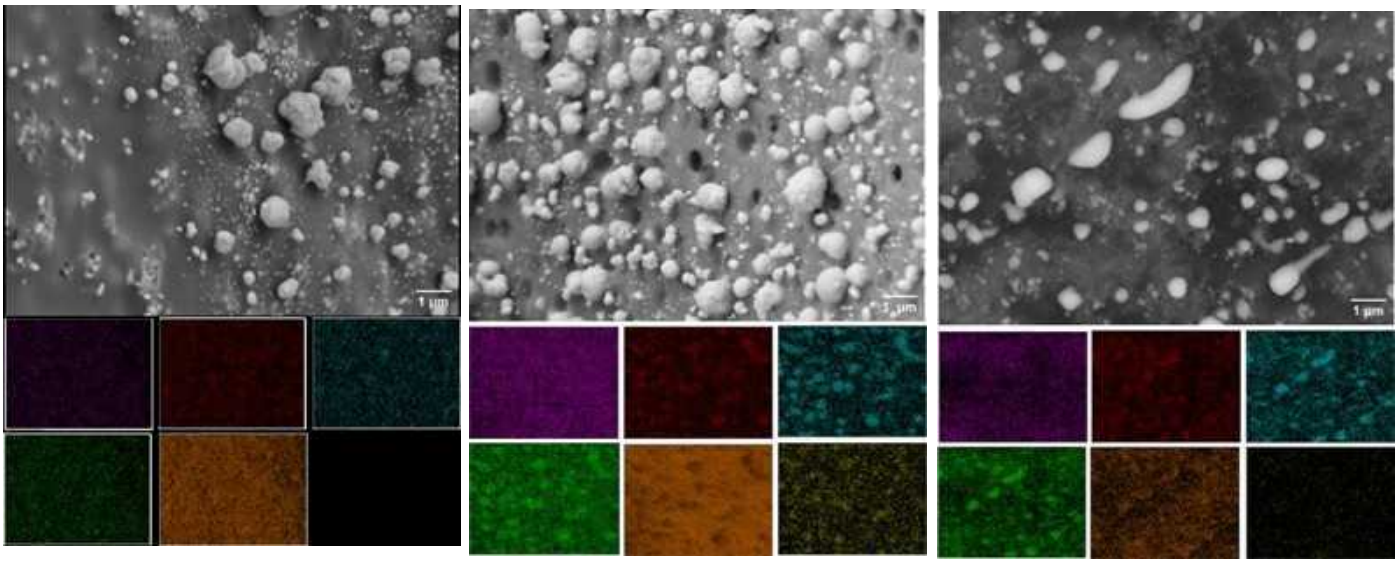
3.6 Thermal engineering of MoFeNiP carbon electrocatalysts for efficient hydrogen evolution in acidic and alkaline media

Hydrogen is a key clean-energy vector, and electrochemical water splitting represents an efficient pathway for producing high-purity hydrogen. HER is kinetically sluggish, especially in alkaline electrolyte, requiring high-performance electrocatalysts. Transition metal phosphides (TMPs) are promising low-cost alternatives to platinum due to their tunable electronic structure, good conductivity, and strong metal–phosphorus synergy.

The presented part of the study investigates multimetallic MoFeNiP catalysts supported on carbon, synthesized via a polymer-metal precursor gel and thermally treated at different temperatures. Unlike traditional Co- or Ni-rich phosphides, the material aims to reduce reliance on critical/raw strategic elements by integrating Fe and Mo.

3.6.1 Catalyst synthesis

A PAN-based polymer gel containing Mo, Fe, Ni chloride salts and H_3PO_4 was prepared in DMF. After drying, the gel was subjected to heat treatment procedure as follow: (i) Stabilization at 270 °C, (ii) Pyrolysis under Ar at 800, 1000, or 1200 °C and (i) Final reduction in Ar/H_2 at 780 °C to form the MoFeNiP phosphides. The resulting powders are designated C-MoFeNiP-800, C-MoFeNiP-1000, and C-MoFeNiP-1200 (Fig. 21).



(a) (b) (c)

Fig. 21. SEM images and corresponding mappings for (a) MoFeNiP-800, (b) MoFeNiP-1000, and (c) MoFeNiP-1200. Elemental distributions are color-labeled as Mo (purple), Fe (red), Ni (blue), P (green), C (orange), and O (yellow). The elemental mapping images correspond to the SEM micrographs shown above (scale bar as indicated).

3.6.2 Characterization techniques

The structural and chemical properties of the synthesized catalysts were examined using several complementary analytical methods. X-ray diffraction (XRD) was employed to identify the crystalline phases formed during thermal treatment. To assess the ordering and defect density of the carbon matrix, Raman spectroscopy was performed. The surface morphology, particle dispersion, and elemental distribution within the materials were investigated using scanning electron microscopy (SEM) coupled with energy-dispersive X-ray spectroscopy (EDX).

Thermal decomposition behavior of the polymer–metal precursor was analyzed by thermogravimetric (TG) and differential scanning calorimetry (DSC)

measurements. The electrocatalytic performance toward the hydrogen evolution reaction was evaluated through a range of electrochemical techniques, including linear sweep voltammetry (LSV), Tafel analysis, electrochemical impedance spectroscopy (EIS), cyclic voltammetry (CV), and long-term chronoamperometry. All measurements were conducted in both 0.5 M H_2SO_4 (acidic medium) and 1 M KOH (alkaline medium) to assess catalytic activity across different pH environments (Fig. 22).



Fig. 22. Three electrode set-up for TMP powder measurement. Working electrode glassy carbon rotation disc electrode (rpm 500), reference electrode Ag/Ag/Cl (3M) and Pt plate as a counter electrode.

3.6.3 Structural and morphological properties – thermal decomposition

The thermal decomposition behavior of the polymer–metal precursor was examined using TG/DSC analysis, which revealed three distinct stages of transformation (Fig. 23). The first stage, occurring between 23 and 233 °C,

corresponds to the stabilization of the PAN polymer accompanied by hydrolysis of the incorporated metal salts. During this phase, the release of HCl and other gaseous by-products contributes to the development of a porous internal structure. The second stage takes place between 233 and 600 °C, where progressive dehydration and decomposition of the Fe- and Ni-chloride hydrates occur. This step is characterized by continued mass loss associated with the breakdown of crystallization water and intermediate hydrolysis products. In the third stage, observed between 600 and 800 °C, the precursor undergoes final dechlorination and conversion of the decomposed metal species into a mixed $MoFeNi(PO_4)_2$ oxide phase. This thermally stable oxide serves as the intermediate precursor for subsequent phosphide formation. The insights obtained from the TG/DSC profiles provided the basis for selecting pyrolysis temperatures of 800, 1000, and 1200 °C for the controlled synthesis of the MoFeNiP catalysts.

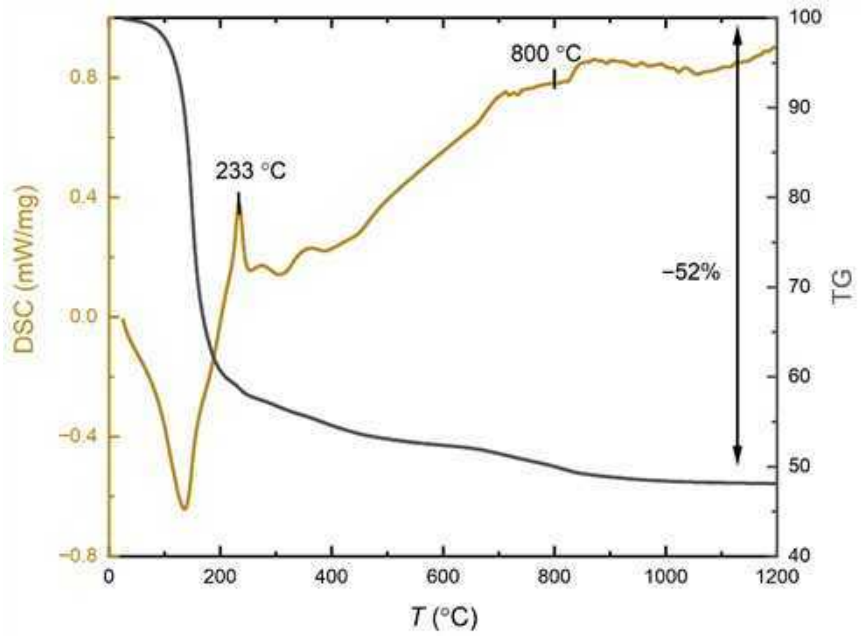


Fig. 23. Thermogravimetric (TG) and differential scanning calorimetry (DSC) analysis profiles recorded for the precursor gel sample.

3.6.4 XRD analysis and Raman spectroscopy

X-ray diffraction analysis confirmed that all synthesized samples exhibited a combination of crystalline phases, including orthorhombic MoFeP, hexagonal NiMoP, and a graphitic carbon phase (Fig. 24). Although the phase composition remained consistent across the series, increasing the pyrolysis temperature enhanced the overall crystallinity of the metal phosphides. This improvement was reflected in sharper and more intense diffraction peaks, indicating better structural ordering and more well-defined phosphide domains at higher temperatures. Raman spectra of all samples displayed the characteristic D band at approximately 1340 cm^{-1} and the G band at around 1586 cm^{-1}, corresponding to disordered and graphitic carbon structures, respectively (Fig. 25). The intensity ratio ID/IG was close to unity for every sample, revealing that the carbon matrix is highly defect-rich and only partially graphitized. Such structural disorder is advantageous for electrocatalytic applications, as it increases the number of edge sites and active regions that can contribute to enhanced HER performance.

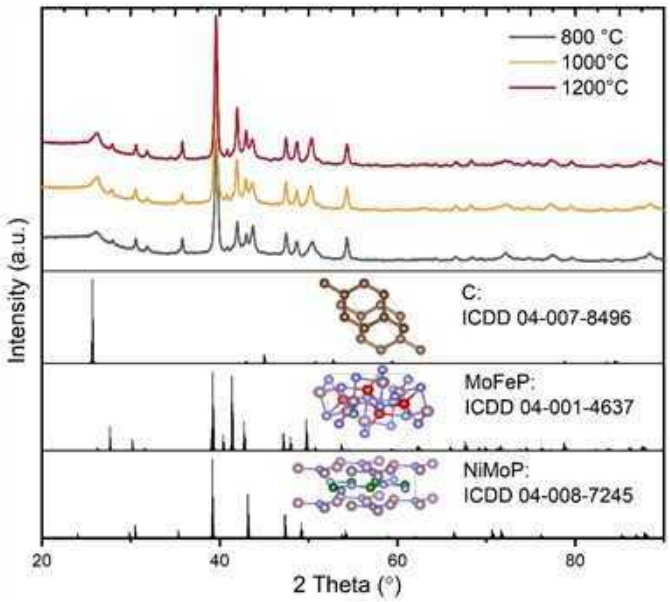


Fig. 24. XRD of C-MoFeNiP samples heat treated at different temperatures.

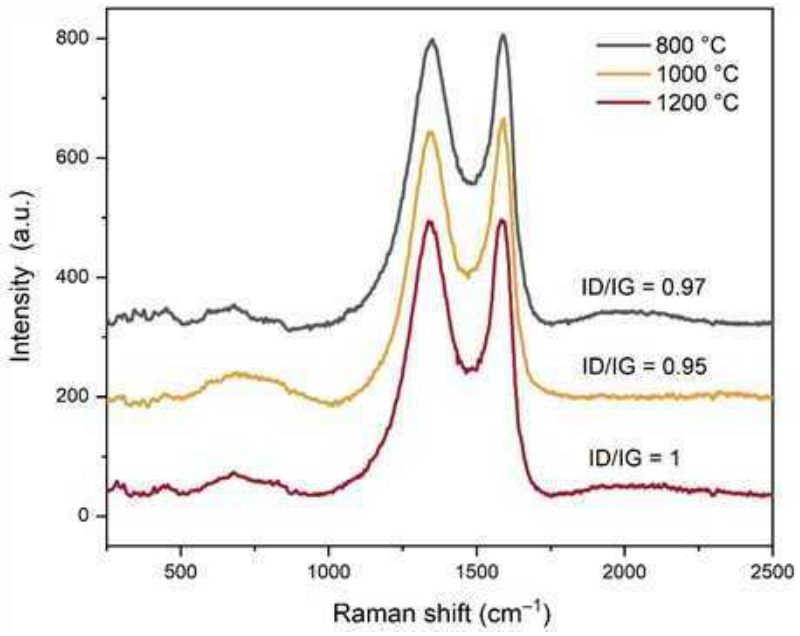
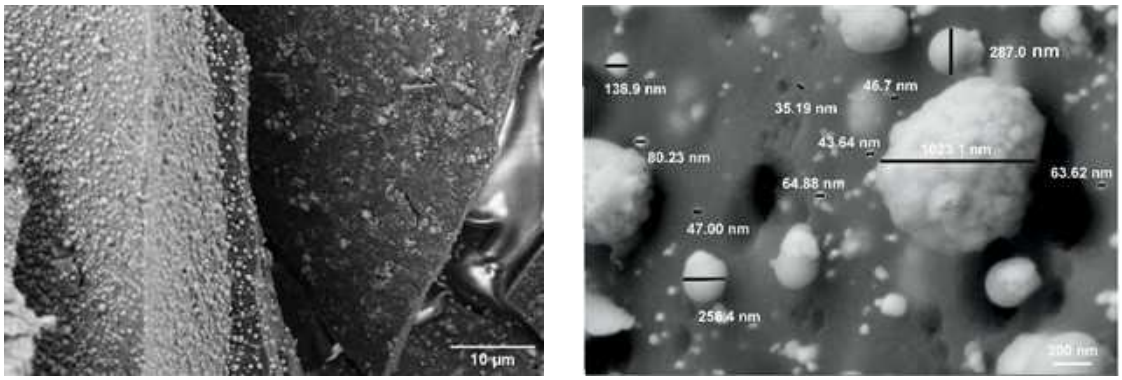


Fig. 25. Raman spectra of C-MoFeNiP samples treated at different temperatures with the ID/IG ratio.

3.6.5. SEM/EDX analysis

SEM observations revealed that the synthesized materials consist of nanoparticles ranging from approximately 30 nm to 1 µm, uniformly dispersed throughout the carbon matrix (Fig. 26). With increasing pyrolysis temperature, the particles exhibited a subtle morphological shift from predominantly spherical to slightly ellipsoidal shapes, a change attributed to enhanced atomic mobility and anisotropic growth at elevated temperatures. Complementary EDX analysis confirmed a homogeneous distribution of Mo, Fe, Ni, and P within the observed particles, verifying the successful formation of multimetallic phosphide domains. A marginally lower detected content of molybdenum was noted, likely arising from partial X-ray absorption within the surrounding carbon matrix, which can attenuate Mo signals during EDX measurement.



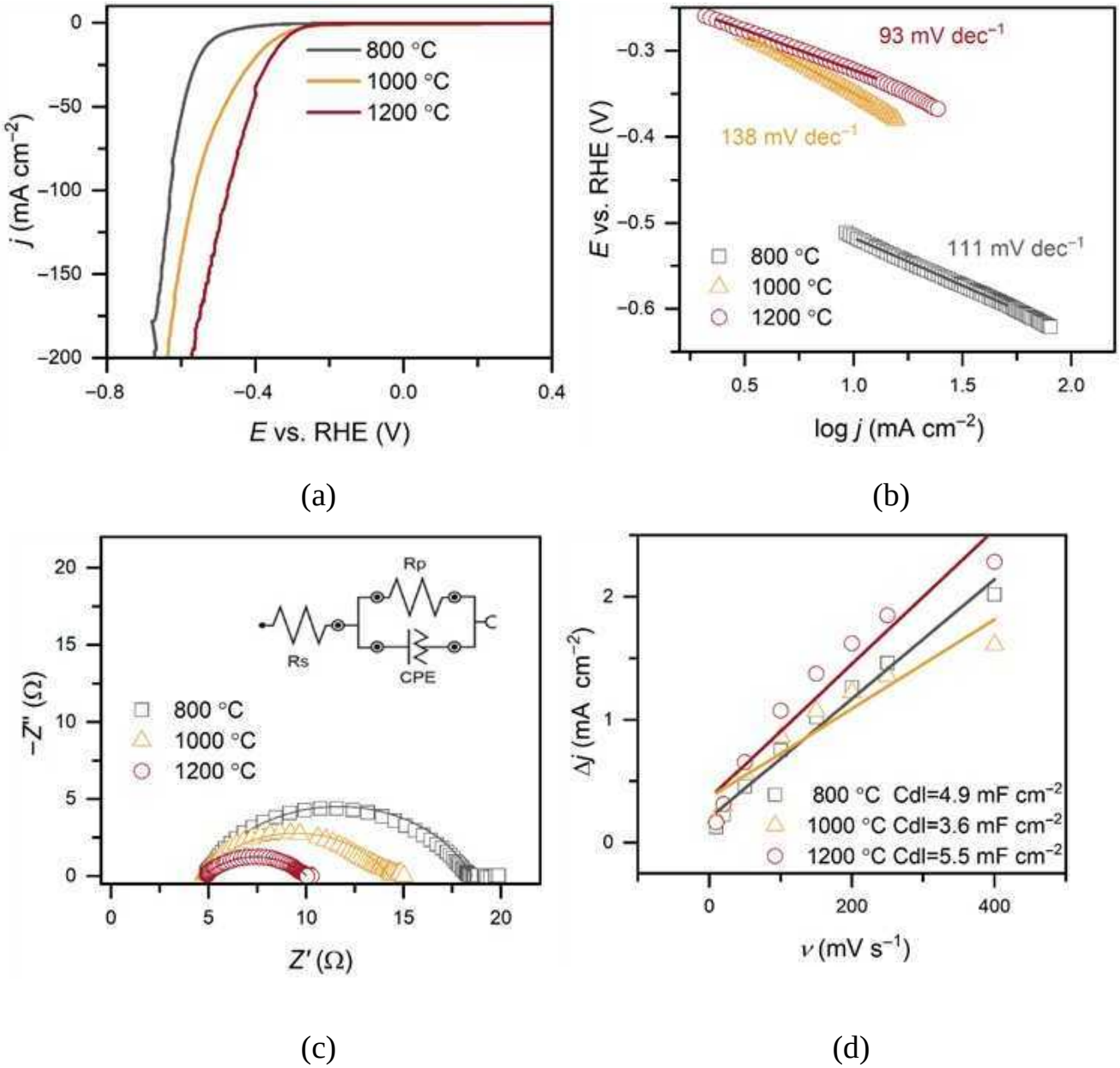
(a) (b)

Fig. 26. SEM image of the C-MoFeNiP-1000: (a) dispersion of MoFeNiP particle within the carbon matrix, (b) particle size distribution.

3.6.6. Electrochemical characterization

The electrocatalytic performance of C-MoFeNiP materials synthesized at different pyrolysis temperatures was systematically studied for HER in both alkaline and acidic media. In alkaline conditions, HER activity increased with higher pyrolysis temperatures, with C-MoFeNiP-1200 showing the best performance (η_{10} = 321 mV). In acidic media, the optimal catalyst was C-MoFeNiP-1000 (η_{10} = 228 mV), highlighting that the ideal pyrolysis temperature depends on the electrolyte, in agreement with previous studies. Kinetic analysis revealed that the most active catalysts also exhibited favorable reaction parameters, including the lowest Tafel slopes, highest charge transfer coefficients, and smallest charge transfer resistances, indicating efficient electron transfer at the catalyst–electrolyte interface. Tafel slopes decreased with increasing pyrolysis temperature from ~120 mV dec^{-1} to 93 mV dec^{-1} for C-MoFeNiP-1200 in alkaline media, and to 98 mV dec^{-1} for C-MoFeNiP-1000 in acidic media, suggesting enhanced Volmer step kinetics and improved overall HER activity. Electrochemical impedance spectroscopy (EIS) provided further insight into charge-transfer behavior. Nyquist plots, fitted with an equivalent circuit consisting of solution resistance (R_s), charge transfer resistance

(R_{ct}), and a constant phase element (CPE), showed similar R_s values (4–5 Ω) for all catalysts in both alkaline and acidic media. All measurements and parameters are summarized in Figs. 27, 28 and Tabs. 5 and 6.



(a) (b)

(c) (d)

Fig. 27. (a) LSV curves of C-MoFeNiP catalysts treated at different temperatures, measured in 1 M KOH (scan rate of 1 mV s^{-1} and rotation speed of 500 rpm); (b) corresponding Tafel plots; (c) Nyquist plots from EIS recorded in 1 M KOH at

–485 mV with the inset showing the equivalent circuit; (d) capacitance current density vs. scan rate with C_{dl} values.

In alkaline media, the reaction mechanism likely involves OH^- generation and the formation of oxide/hydroxide intermediates. Detailed steps of the mechanism are outlined below for clarity.

HER in alkaline electrolyte.

$MoFeNiP + H_2O + e^- \rightarrow MoFeNiPH^* + OH^-$ discharge Volmer reaction

$MoFeNiP + OH^- \rightarrow MoFeNi–O(OH)/OH + P$ {surface or dissolution}

Either

$MoFeNiPH^* + H_2O + e^- \rightarrow MoFeNiP + H_2 + OH^-$ desorption Heyrovsky reaction

or

$MoFeNiPH^* + MoFeNiPH^* \rightarrow 2MoFeNiP + H_2$ recombination Tafel reaction

HE R in acidic:

$MoFeNiP + H^+ + e^- \rightarrow MoFeNiPH^*$ discharge Volmer reaction

either

$MoFeNiPH^* + H^+ + e^- \rightarrow MoFeNiP + H_2$ desorption Heyrovsky reaction

or.

$MoFeNiPH^* + MoFeNiPH^* \rightarrow 2MoFeNiP + H_2$ recombination Tafel reaction

During the Volmer step, the generation of OH^- ions near the electrode surface locally increases the pH, which promotes surface hydroxylation or oxidation. This can lead to the formation of a thin (oxy)hydroxide layer, such as $Ni(OH)_2$, FeOOH, or MoO, while part of the phosphide phase may dissolve into the electrolyte. Such surface reconstruction can contribute to minor activation effects or stabilization during continuous operation. These processes help explain the distinct stability

behavior observed in 1 M KOH compared with acidic media, where hydroxide formation does not occur and the catalyst generally requires more time to reach a steady state during HER.

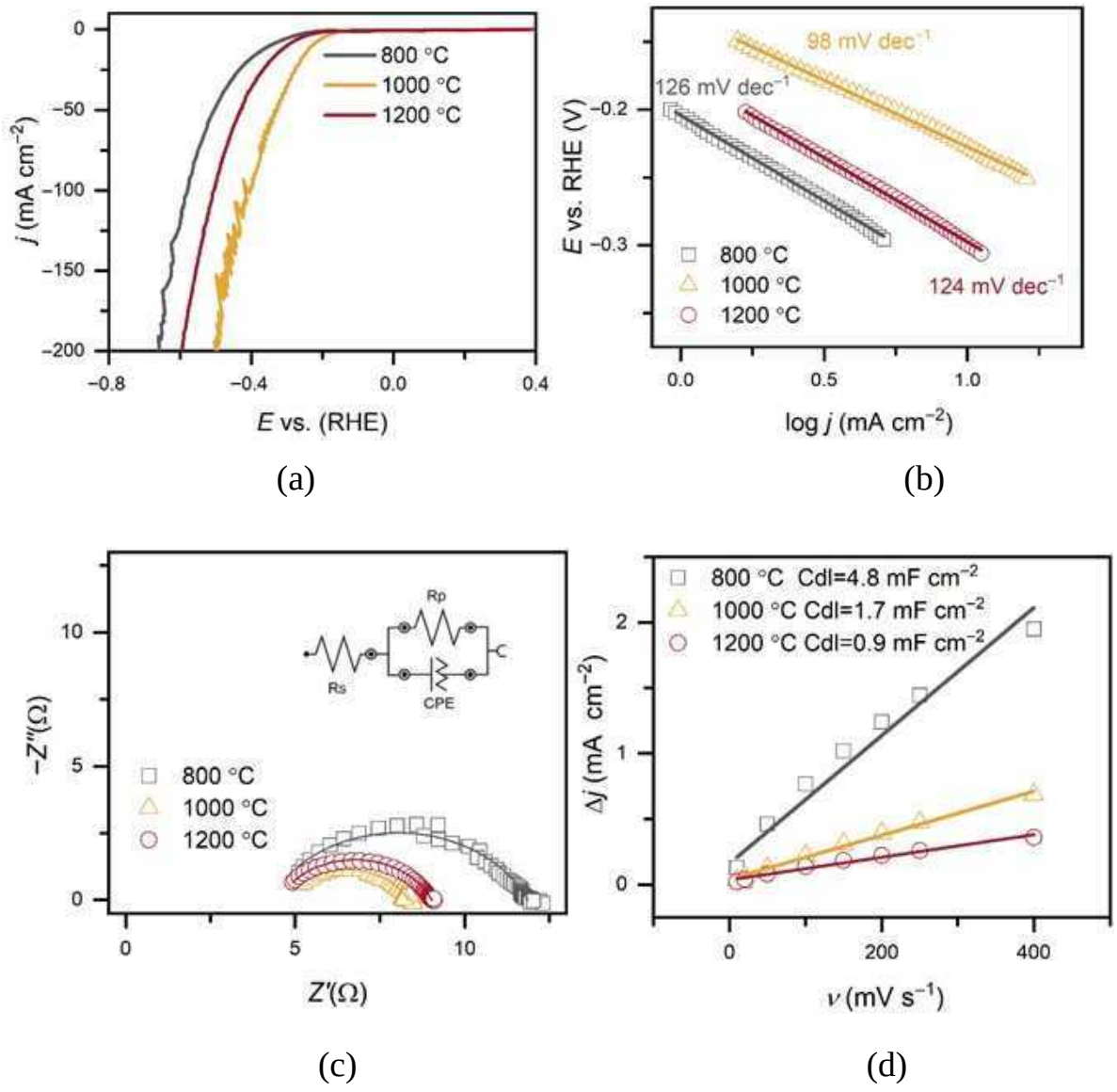


Fig. 28. (a) LSV curves of C-MoFeNiP catalysts treated at different temperatures, measured in 0.5 M H_2SO_4 (scan rate of 1 mV s^{-1} and rotation speed of at 1000 rpm); (b) Corresponding Tafel plots; (c) Nyquist plots from EIS recorded in 0.5 M H_2SO_4 at −589 mV; (d) Capacitance current density vs. scan rate with C_{dl} values.

Table 5. Summary of electrochemical parameters measurements in 1 M KOH for C-MoFeNiP cat-alysts treated at different temperatures.

	C-MoFeNiP-800	C-MoFeNiP-1000	C-MoFeNiP-1200
LSV analysis			
η10 (mV)	522	349	321
Tafel slop (mV dec^{-1})		138	93
j_0 (mA cm^{-2})	$2.2 \cdot 10^{-4}$	$2.8 \cdot 10^{-2}$	$3.4 \cdot 10^{-3}$
α	0.53	0.43	0.64
EIS analysis			
Y_0-CPE ($mS \cdot s^N$)	0.19	0.54	2.2
Rct (Ω)	13.7	9.6	5.3
Rs (Ω)	4.8	4.7	4.7
N-CPE	0.742	0.670	0.562
Ceff (F)	$2.3 \cdot 10^{-5}$	$3.5 \cdot 10^{-5}$	$6.7 \cdot 10^{-5}$
χ^2	0.03	0.03	0.003
CV analysis			
Cdl (mF cm^{-2})	4.9	3.6	5.5

* η10 (mV)—Overpotential at 10 mA cm^{-2}, j_0—Exchange current density, α—Charge transfer coefficient, CPE—constant phase element, Y_0-CPE admittance, N—CPE exponent change, Rct—charge transfer resistance, Rs—Solution resistance, Ceff—Effective capacitance, χ^2—Chi-squared fitting, Cdl—Double-layer capacitance.

Table 6. Summary of electrochemical parameters measurements in 0.5 M H_2SO_4 for C-MoFeNiP catalysts treated at different temperatures.

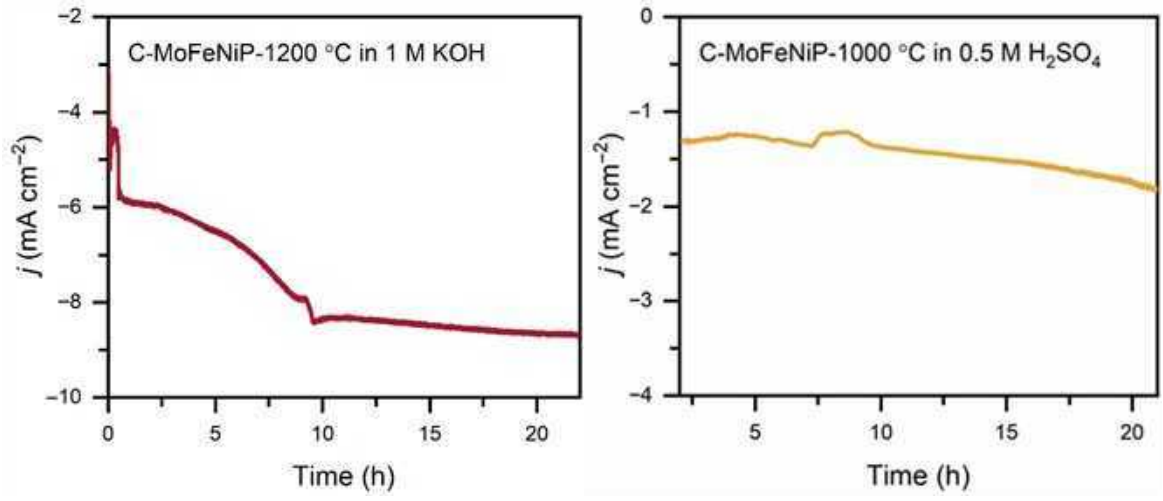
Parameters	C-MoFeNiP-800	C-MoFeNiP-1000	C-MoFeNiP-1200
LSV analysis			
η10 (mV)	349	228	300
Tafel slop (mV dec^{-1})	126	98	124
j_0 (mA cm^{-2})	$2.4 \cdot 10^{-2}$	$4.8 \cdot 10^{-2}$	$4.0 \cdot 10^{-2}$
α	0.47	0.60	0.48
EIS analysis			
Y_0-CPE ($mS \cdot s^N$)	0.030	0.080	0.054
Rct (Ω)	7.6	3.6	4.5
Rs (Ω)	4.2	4.8	4.5
N-CPE	0.741	0.715	0.746
Ceff (F)	$1.5 \cdot 10^{-6}$	$3.1 \cdot 10^{-6}$	$3.1 \cdot 10^{-6}$
χ^2	0.03	0.008	0.001
CV analysis			
Cdl (mF cm^{-2})	4.8	1.7	0.9

In alkaline media, Rct decreased with increasing pyrolysis temperature (13.7 Ω → 5.3 Ω for C-MoFeNiP-800 → -1200), indicating more efficient charge transfer for higher-temperature samples. In acidic media, R_{ct} showed a different trend, with the lowest value for C-MoFeNiP-1000 (3.6 Ω), consistent with its superior HER activity. The CPE exponent (N-CPE) was nearly constant in acidic media but decreased in KOH with higher synthesis temperatures, likely due to surface reconstruction and oxy(hydroxide) formation, as commonly observed for TMP catalysts. Capacitance analysis showed that while C_{dl} from non-faradaic CV measurements did not correlate with HER activity, the effective capacitance (C_{eff}) from EIS under faradaic conditions did, reflecting the true active sites. This suggests that the carbon matrix mainly provides conductivity and stability, whereas HER activity originates from the metallic phosphide phases. Differences in HER performance are attributed to structural and compositional changes. XRD and EDX revealed that higher pyrolysis temperatures enhance crystallinity, interdiffusion, and

mixing of metal species, while Raman spectra indicated minimal changes in carbon disorder. Morphology analysis showed notable alterations at 1200 °C, highlighting that catalytic activity is primarily governed by the crystalline phase and composition of the phosphides.

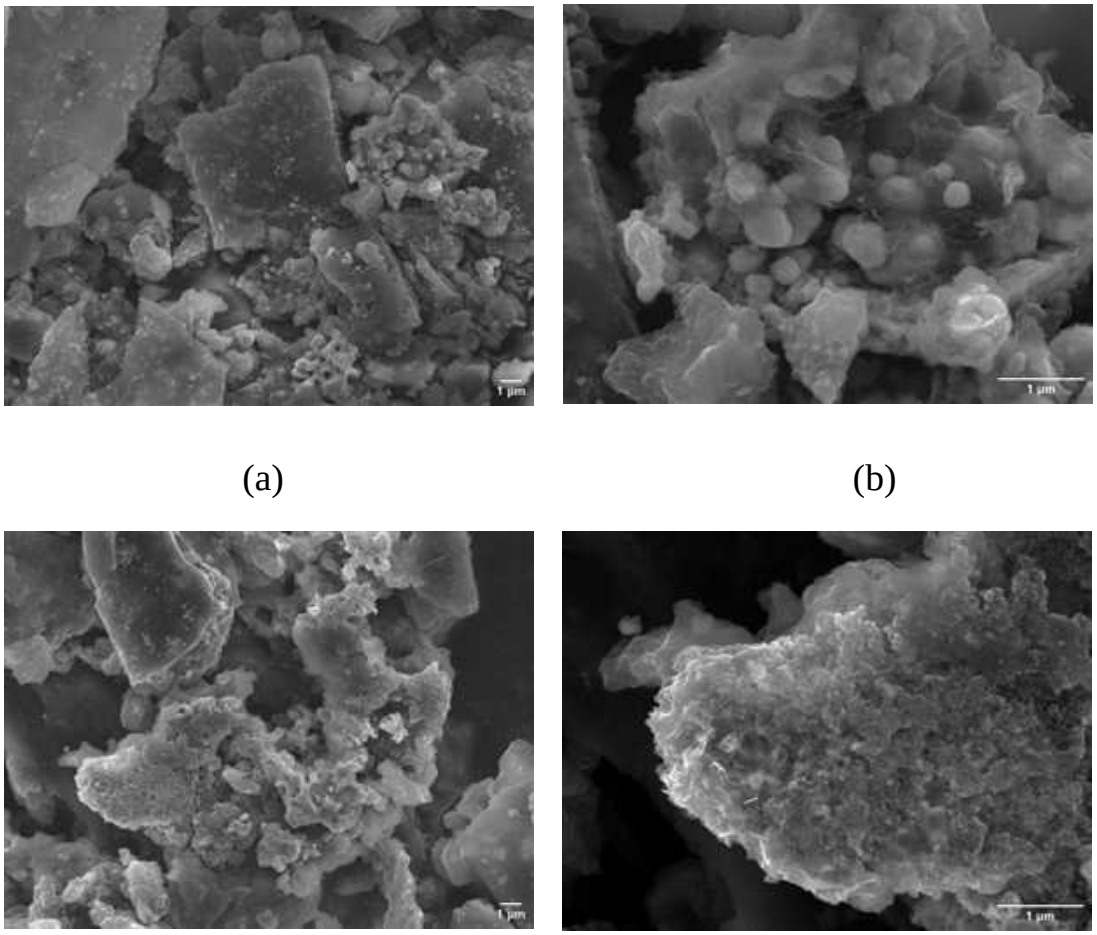
Stability tests of the best catalysts in each medium showed that C-MoFeNiP-1200 in alkaline media exhibited an initial current increase over 10 h, then stabilized, while C-MoFeNiP-1000 in acid maintained a stable current throughout (Fig. 29). Post-stability EDX analysis revealed a decrease in the M/P ratio and increased oxygen content in alkaline media, indicating partial P dissolution and surface oxidation, whereas the M/P ratio remained almost unchanged in acidic media .

Lower current densities in acid may result from hydrogen bubble accumulation on the electrode, which can block active sites; this can be mitigated under pressurized electrolyzer conditions. SEM imaging showed overall structural integrity, though high-resolution images revealed surface disruption: carbon matrix leaching in acid exposed phosphide particles, while alkaline conditions caused increased porosity (Fig. 30).



(a) (b)

Fig. 29. Chronopotentiometric stability measurement for C-MoFeNiP for 22 h (a) at −285 mV vs. RHE in an alkaline environment, and (b) at −229 mV vs. RHE in an acidic environment.



(a) (b)

(c) (d)

Fig. 30. SEM images of C-MoFeNiP after a 22 h22-h chronoamperometry stability test: (a,b) post-test morphology in an acidic environment; (c,d) post-test morphology in an alkaline environment.

Overall overview, the electrochemical analyses show that the HER performance of C-MoFeNiP catalysts is strongly influenced by pyrolysis temperature, which affects the crystalline phase and composition of the metal phosphides, Volmer step kinetics, and charge-transfer properties at the catalyst–electrolyte interface. As a multimetallic phosphide system, C-MoFeNiP exhibits distinct behavior in acidic and

alkaline media due to differences in HER mechanisms, adsorption characteristics, and pH-dependent active site functionality.

For TMP-based catalysts, different behaviors in alkaline and acidic environments have been reported. In alkaline media, where HER is generally limited by water dissociation, phosphorus can dissolve, leaving the metal to form hydroxides or oxides. Mo oxides formed on MoFeNiP have been shown to enhance HER activity, although some reports suggest that the apparent activity increase arises from an enlarged ECSA, and per-ECSA activity may actually decrease. Detailed characterization before and after stability tests is needed to clarify these activation processes and optimize performance in alkaline media.

In acidic media, where the Volmer step is fast, both metal and phosphorus dissolve proportionally, maintaining catalytic activity. However, hydrogen bubble accumulation can form a resistive barrier that reduces performance. Optimizing the hydrophilic/hydrophobic balance of C-MoFeNiP could facilitate bubble release and improve activity.

4. Identification of issues and risks

During the implementation of the DEMADES project, several potential issues and risks were identified that could affect the project timeline and achievement of objectives.

Key risks include:

- **Financial and administrative delays**: Initial funding delays could impact the schedule for experimental work and procurement of laboratory materials.
- **Technical risks**: Possible malfunction or unavailability of specific instruments and materials required for catalyst synthesis and electrochemical measurements.

- **Personnel risks**: Limited availability of qualified researchers or staff could affect the pace of planned experiments.

Risks were continuously monitored and mitigated through:

- ✓ regular consortium meetings and coordination,
- ✓ targeted training and workshops for laboratory personnel,
- ✓ flexible planning and adaptation of experimental schedules.

5. Description of planned activities in the next monitoring period (Months 11–20)

In the next monitoring period (Months 11–20), the DEMADES project will continue the implementation of planned activities across all work packages, focusing on completing experimental tasks, evaluating results, and preparing final project outputs. Key planned activities include:

WP 1 – Catalysts Preparation (Months 11–18):

- Completion of experimental syntheses and optimization of electrochemical and chemical deposition processes.
- Finalization of noble metal decoration of catalysts and determination of optimal parameters.
- Processing and analysis of all collected data and updating theoretical models.
- Preparation and submission of additional conference papers and research articles.
- Preparation and submission of the final WP 1 report.

WP 2 – Catalysts Characterization (Months 11–18):

- Continuation of detailed characterization of catalysts using SEM, AFM, EDX, XPS, XRD, FTIR, and Raman spectroscopy.
- Integration of WP 1 and WP 3 results to evaluate the influence of synthesis on catalytic activity.

- Organization of internal meetings and discussions for knowledge sharing.
- Preparation of the final WP 2 report.

WP 3 – Electrochemical Performance Evaluation (Months 11–18):

- Completion of the assessment of catalytic activity of new catalysts for HER in alkaline media.
- Analysis of parameters such as overpotential, Tafel slope, TOF, and Faradaic efficiency.
- Conducting webinars and advanced training courses for project team members.
- Evaluation of the feasibility of a pilot electrolyser for "green" hydrogen production.
- Preparation and submission of the final WP 3 report.

WP 4 – Sustainability Assessment (Months 11–19):

- Continuation of testing catalysts' corrosion resistance and operational longevity.
- Assessment of environmental and economic impacts of the catalysts.
- Formulation of recommendations and specific performance metrics for long-term catalyst stability.
- Preparation and submission of the final WP 4 report.

WP 5 – Theories Formation and Scaling-up Potential (Months 15–20):

- Development of theoretical frameworks describing kinetics and mechanisms of catalyst synthesis.
- Analysis of the relationships between catalyst structure and performance.
- Preparation of strategies for scaling-up production and industrial implementation.
- Preparation of the final WP 5 report and comprehensive final project report.

- Organization of a meeting with all partners to discuss results from all previous work packages (M5.1).

These planned activities will ensure that the project achieves its objectives, produces relevant scientific outputs, and lays the foundation for the practical application of the developed catalysts.

6. Summary of the interim report (WP1–3)

During the first ten months of the DEMADES project, substantial progress was achieved across Work Packages WP1–WP3, ensuring smooth implementation of project goals and establishing a solid basis for the upcoming phases.

Within **WP1 (Project Management and Coordination)**, the consortium maintained effective collaboration through regular strategic meetings, internal consultations, and continuous communication among all partner institutions. These activities supported proper planning, timely reporting, risk monitoring, and alignment of work across scientific and administrative tasks.

WP2 (Material Development and Characterization) focused on advancing the preparation and analysis of novel catalytic materials. The research teams successfully initiated and carried out key tasks related to material synthesis, structural evaluation, and performance assessment. Achieved results demonstrate clear progress toward the development of materials required for improved hydrogen production technologies.

In **WP3 (Electrochemical Evaluation and Performance Testing)**, systematic studies of material behaviour, stability, and efficiency under different operational conditions were initiated. These activities enabled the project to verify the potential of developed materials and to prepare for more advanced testing in the following project stages.

The project team actively disseminated results through participation in international conferences, scientific workshops, professional training programs, and public outreach events. Several scientific publications have already been produced, including conference proceedings, peer-reviewed articles, and submitted manuscripts. Additionally, DEMADES team members received notable awards and external recognition, contributing to the project's visibility and impact.

The progress achieved in months 1–10 confirms that the DEMADES project is developing in accordance with the work plan. The consortium has successfully launched essential research tasks, strengthened scientific cooperation, and ensured effective dissemination and promotion of project outcomes.